

Copyright is owned by the Author of the thesis. Permission is given for a copy to be downloaded by an individual for the purpose of research and private study only. The thesis may not be reproduced elsewhere without the permission of the Author.

# **Salicylaldoxime Derivatives for New Magnetic Materials**

A thesis presented in partial fulfilment of the requirements for the  
degree of

**Master of Science**

**in Chemistry**

at Massey University, Manawatu, New Zealand.

Sidney Woodhouse

2019



## Abstract

Salicylaldoxime ( $H_2Sao$ ) is an appealing unit for metal ion coordination, specifically that of transition metal ( $3d$ ) ions. During this research, four ligands were synthesised, of which two were previously unknown (**L2** and **L3**). These ligands differed by the secondary amine added to the simple  $H_2Sao$  molecule. These  $H_2Sao$  derived ligands were complexed with a variety of  $3d$  ions, resulting in three distinct topologies: mononuclear, triangular, and defective dicubane. The nine new complexes (**C1-C9**) synthesised were all structurally characterised, with Mössbauer spectroscopy performed on the iron complexes, and magnetic characterisation performed on complexes **C1-C6**, **C8-C9**. Analysis of the synthesised complexes has led to new insights into magnetostructural correlations and new pathways to unique ligand designs.



## Acknowledgements

I would like to acknowledge and thank my supervisor Assoc. Prof. Paul Plieger for his support, guidance and enthusiasm throughout my research project. I would like to thank my co-supervisor Assoc. Prof. Gareth Rowlands for his support and help with synthetic procedures.

I am grateful to the Plieger/Rowlands research groups for their friendship, constant support and encouragement throughout my Masters' research and all areas of life. I would especially like to thank Tyson Dais, for his advice and help with the screening and collection of crystal structures.

I would like to acknowledge Prof. Euan Brechin and his research group for performing and the analysis of the magnetic measurements of complexes, **C4-C6**, **C8-C9**, Assoc. Prof. Guy Jameson for the Mössbauer measurements of complexes **C5** and **C7**, and the research staff at the Haijima Rigaku laboratory in Tokyo, Japan for the collection of the X-ray data of **C3**.

Finally, to my family, I would like to thank them for their continual support and encouragement throughout this research project.



# Table of Contents

<b>Abstract .....</b>	<b>iii</b>
<b>Acknowledgements .....</b>	<b>v</b>
<b>Table of Contents.....</b>	<b>vii</b>
<b>List of Figures .....</b>	<b>ix</b>
<b>List of Tables .....</b>	<b>xv</b>
<b>Abbreviations .....</b>	<b>xvii</b>
<b>1.0 Introduction.....</b>	<b>1</b>
<b>1.1 Magnetism.....</b>	<b>1</b>
1.1.1 Exchange Interactions .....	2
1.1.2 Single Molecule Magnetism .....	3
<b>1.2 Characterisation Techniques.....</b>	<b>6</b>
1.2.1 X-ray Diffraction.....	6
1.2.2 Magnetic Measurements.....	8
1.2.3 Mössbauer Spectroscopy.....	9
<b>1.3 Coordination Chemistry of Salicylaldoxime .....</b>	<b>11</b>
<b>1.4 Aims of Research .....</b>	<b>21</b>
<b>2.0 Ligand Design and Synthesis.....</b>	<b>22</b>
<b>2.1 General Ligand Design.....</b>	<b>22</b>
<b>2.2 General Synthesis.....</b>	<b>24</b>
<b>2.3 General Ligand Characterisation.....</b>	<b>26</b>
2.3.1 NMR Interpretation of the Ligands and their Precursors .....	26
2.3.2 IR Interpretation of the Ligands and their Precursors.....	29
<b>3.0 Transition Metal Complexes .....</b>	<b>30</b>
<b>3.1 General Complexation Synthesis and Characterisation.....</b>	<b>30</b>
3.1.1 General Synthetic Methods.....	30



3.1.2 IR Characterisation of Complexes <b>C1-C9</b> .....	31
<b>3.2 Mononuclear Complexes</b> .....	<b>33</b>
3.2.1 [Cu( <b>L1</b> ) <sub>2</sub> (BF <sub>4</sub> ) <sub>2</sub> ] ( <b>C1</b> ), [Ni( <b>L1-H</b> ) <sub>2</sub> ] ( <b>C2</b> ), and [Mn( <b>L4a</b> ) <sub>2</sub> (NO <sub>3</sub> ) <sub>2</sub> ](NO <sub>3</sub> ) ( <b>C3</b> ) .....	33
<b>3.3 Dinuclear Complexes</b> .....	<b>46</b>
3.3.1 [Cu <sub>2</sub> ( <b>L3'</b> ) <sub>2</sub> Cl <sub>2</sub> ] ( <b>C4</b> ) .....	46
<b>3.4 Trinuclear Complexes</b> .....	<b>52</b>
3.4.1 [Fe <sub>3</sub> O( <b>L4-H</b> ) <sub>3</sub> (OAc) <sub>3</sub> ] ( <b>C5</b> ) and [Mn <sub>3</sub> O( <b>L4-H</b> ) <sub>2</sub> ( <b>L4-2H</b> )(OAc) <sub>3</sub> ] ( <b>C6</b> ) .....	52
<b>3.5 Tetranuclear Complexes</b> .....	<b>65</b>
3.5.1 [Fe <sub>4</sub> ( <b>L3</b> ) <sub>2</sub> (OMe) <sub>6</sub> (OH) <sub>6</sub> ] ( <b>C7</b> ).....	65
3.5.2 [Ni <sub>4</sub> ( <b>L2-H</b> ) <sub>2</sub> (OAc) <sub>2</sub> (OMe) <sub>2</sub> Cl <sub>2</sub> ](Et <sub>2</sub> O) <sub>3</sub> ( <b>C8</b> ) and [Ni <sub>4</sub> ( <b>L3-H</b> ) <sub>2</sub> (OAc) <sub>2</sub> (OMe) <sub>2</sub> Cl <sub>2</sub> ](MeOH) <sub>2</sub> ( <b>C9</b> ) .....	71
<b>4.0 Experimental Methods</b> .....	<b>81</b>
<b>4.1 General Procedures</b> .....	<b>81</b>
<b>4.2 Ligand Synthesis</b> .....	<b>84</b>
4.2.1 Synthesis of Precursors <b>1</b> and <b>2</b> .....	84
4.2.2 Synthesis of <b>L1</b> .....	86
4.2.3 Synthesis of <b>L2</b> .....	88
4.2.4 Synthesis of <b>L3</b> .....	90
4.2.5 Synthesis of <b>L4</b> .....	93
<b>4.3 Complexation Synthesis</b> .....	<b>95</b>
4.3.1 [Cu( <b>L1</b> ) <sub>2</sub> (BF <sub>4</sub> ) <sub>2</sub> ] ( <b>C1</b> ) .....	95
4.3.2 [Ni( <b>L1-H</b> ) <sub>2</sub> ] ( <b>C2</b> ) .....	95
4.3.3 [Mn( <b>L4a</b> ) <sub>2</sub> (NO <sub>3</sub> ) <sub>2</sub> ](NO <sub>3</sub> ) ( <b>C3</b> ) .....	96
4.3.4 [Cu <sub>2</sub> ( <b>L3'</b> )Cl <sub>2</sub> ] ( <b>C4</b> ) .....	96
4.3.5 [Fe <sub>3</sub> O( <b>L4-H</b> ) <sub>3</sub> (OAc) <sub>3</sub> ] ( <b>C5</b> ).....	97
4.3.6 [Mn <sub>3</sub> O( <b>L4-H</b> ) <sub>2</sub> ( <b>L4-2H</b> )(OAc) <sub>3</sub> ] ( <b>C6</b> ) .....	98
4.3.7 [Fe <sub>4</sub> ( <b>L3</b> ) <sub>2</sub> (OMe) <sub>6</sub> (OH) <sub>6</sub> ] ( <b>C7</b> ).....	98
4.3.8 [Ni <sub>4</sub> ( <b>L2-H</b> ) <sub>2</sub> (OAc) <sub>2</sub> (OMe) <sub>2</sub> Cl <sub>2</sub> ](Et <sub>2</sub> O) <sub>3</sub> ( <b>C8</b> ) .....	99
4.3.9 [Ni <sub>4</sub> ( <b>L3-H</b> ) <sub>2</sub> (OAc) <sub>2</sub> (OMe) <sub>2</sub> Cl <sub>2</sub> ](MeOH) <sub>2</sub> ( <b>C9</b> ).....	99
<b>5.0 Conclusions and Future Work</b> .....	<b>101</b>
<b>References</b> .....	<b>103</b>
<b>Appendices</b> .....	<b>114</b>

## List of Figures

<b>Figure 1.1:</b> Schematic representations of antiferromagnetic exchange (left) and ferromagnetic exchange (right). .....	2
<b>Figure 1.2:</b> X-ray structure of the SMM with the record-breaking blocking temperature (80K). The ligands utilised, Cp <sup>iPr5</sup> and Cp*, are on the right. H atoms are omitted for clarity; Dy <sup>III</sup> = aqua, C = grey.....	4
<b>Figure 1.3:</b> Schematic representation of the Bragg equation. ....	7
<b>Figure 1.4:</b> Example diffraction pattern .....	8
<b>Figure 1.5:</b> Illustration of an example Mössbauer spectrum.....	10
<b>Figure 1.6:</b> Schematic illustration of a generalised H <sub>2</sub> Sai ligand.....	11
<b>Figure 1.7:</b> Schematic representation of generalised single-headed (left) and double-headed (right) H <sub>2</sub> Sao derivatives.....	11
<b>Figure 1.8:</b> Schematic representation of a selection of the various coordination modes of H <sub>2</sub> Sao derivatives. ....	12
<b>Figure 1.9:</b> Schematic representation of generalised H <sub>2</sub> Sao based mononuclear and triangular complexes. ....	13
<b>Figure 1.10:</b> Crystal structure of a single-headed H <sub>2</sub> Sao based mononuclear Cu <sup>II</sup> complex, which coordinates the Cu <sup>II</sup> ion in a trans configuration. H atoms, apart from ones involved in hydrogen bonding, omitted for clarity. Cu <sup>II</sup> = orange, N = blue, O = red, C = grey, H = white. Hydrogen bonding represented as red dotted lines. ....	13
<b>Figure 1.11:</b> Crystal structure of a double-headed H <sub>2</sub> Sao based mononuclear Cu <sup>II</sup> complex, which coordinates the Cu <sup>II</sup> ion in a cis configuration. H atoms, apart from ones involved in hydrogen bonding, omitted for clarity. Cu <sup>II</sup> = orange, N = blue, O = red, S = yellow, C = grey, H = white. Hydrogen bonding represented as red dotted lines. ....	14
<b>Figure 1.12:</b> Crystal structure of the Mn <sup>III</sup> triangle produced by Brechin and coworkers (left) and corresponding ligands and co-ligands (right). H atoms omitted for clarity; Mn <sup>III</sup> = purple, N = blue, O = red.....	15
<b>Figure 1.13:</b> Crystal structure of the Mn <sup>III</sup> triangular SMM produced by Yang et al. (left) and the corresponding ligand (right). H atoms omitted for clarity; Mn <sup>III</sup> = purple, N = blue, O = red, Cl = green.....	16
<b>Figure 1.14:</b> Schematic representation of the defective dicubane topology; B = body metal ions, W = wingtip metal ions.....	17

<b>Figure 1.15:</b> Crystal structures of the two Ni <sup>II</sup> defective dicubane complexes produced by Jiang et al. (top) and corresponding ligand utilised for both complexes (bottom). H atoms omitted for clarity; Ni <sup>II</sup> = green, N = blue, O = red. ....	18
<b>Figure 1.16:</b> Crystal structure of the Zn <sup>II</sup> /Dy <sup>III</sup> defective dicubane complex produced by Peng et al. H atoms omitted for clarity; Zn <sup>II</sup> = purple, Dy <sup>III</sup> = aqua, N = blue, O = red. ....	19
<b>Figure 1.17:</b> Generalised synthetic route for the in situ condensation reaction between oximic ligands and a boron source (typically either boronic acids, boron trifluoride etherates, and BF <sub>4</sub> <sup>-</sup> anions).....	20
<b>Figure 1.18:</b> Crystal structure of the Cu <sup>II</sup> BF <sub>2</sub> <sup>+</sup> bridged clathrochelate complex (left) and ligand produced in situ (right). H atoms omitted for clarity; Cu <sup>II</sup> = orange, N = blue, O = red, B = light pink, F = yellow. ....	20
<b>Figure 2.1:</b> Schematic representation of the four different ligands utilised in this research .....	22
<b>Figure 2.2:</b> Generalised reaction scheme for the synthesis of ligands <b>L1-L4</b> .....	24
<b>Figure 2.3:</b> The numbering system used for <sup>1</sup> H NMR spectra .....	26
<b>Figure 2.4:</b> The numbering system used for <sup>13</sup> C NMR spectra .....	26
<b>Figure 2.5:</b> Example <sup>1</sup> H NMR of the ligand precursor, <b>L2a</b> . Residual solvent (CDCl <sub>3</sub> ) at 7.26 ppm .....	27
<b>Figure 2.6:</b> Example <sup>1</sup> H NMR of the ligand, <b>L2</b> . Residual solvent (CDCl <sub>3</sub> ) at 7.26 ppm .....	27
<b>Figure 2.7:</b> Example <sup>13</sup> C NMR of the ligand precursor, <b>L2a</b> . Residual solvent (CDCl <sub>3</sub> ) at 77 ppm.....	28
<b>Figure 2.8:</b> Example <sup>13</sup> C NMR of the ligand, <b>L2</b> . Residual solvent (CDCl <sub>3</sub> ) at 77 ppm .....	28
<b>Figure 3.1:</b> Crystal structure of the complex [Cu( <b>L1</b> ) <sub>2</sub> (BF <sub>4</sub> ) <sub>2</sub> ], ( <b>C1</b> ). H atoms, apart from those involved in hydrogen bonding, have been omitted for clarity; Cu <sup>II</sup> = orange, N = blue, O = red, B = light pink, F = yellow, C = grey, H = white. Hydrogen bonding is represented by red dotted lines. ORTEP view at 30% probability level.....	33
<b>Figure 3.2:</b> Crystal structure of the complex [Ni( <b>L1-H</b> ) <sub>2</sub> ], ( <b>C2</b> ). H atoms, apart from those involved in hydrogen bonding, have been omitted for clarity; Ni <sup>II</sup> = green, N = blue, O = red, C = grey, H = white. Hydrogen bonding is represented by red dotted lines. ORTEP view at 30% probability level.....	34
<b>Figure 3.3:</b> Crystal structure of the complex [Mn( <b>L4a</b> ) <sub>2</sub> (NO <sub>3</sub> )](NO <sub>3</sub> ), ( <b>C3</b> ). H atoms, apart from those involved in hydrogen bonding, have been omitted for clarity; Mn <sup>III</sup> = purple, N =	

blue, O = red, C = grey, H = white. Hydrogen bonding is represented by red dotted lines. ORTEP view at 30% probability level .....	34
<b>Figure 3.4:</b> Crystal structure of <b>C3</b> , illustrating the chain-like network produced by hydrogen bonding (red dotted lines).....	35
<b>Figure 3.5:</b> Crystal structure of <b>C1</b> , illustrating the planarity of the structure. ORTEP view at 30% probability level.....	38
<b>Figure 3.6:</b> Crystal structure of <b>C2</b> , illustrating the planarity of the structure. ORTEP view at 50% probability level.....	38
<b>Figure 3.7:</b> Crystal structure of <b>C3</b> , illustrating the non-planarity of the structure. ORTEP view at 50% probability level.....	39
<b>Figure 3.8:</b> Crystal structure of the mononuclear Cu <sup>II</sup> complex, with weakly coordinated BF <sub>4</sub> <sup>-</sup> anions produced by Forgan <i>et al.</i> H atoms, apart from those involved in hydrogen bonding, have been omitted for clarity; Cu <sup>II</sup> = orange, N = blue, O = red, B = light pink, F = yellow, C = grey, H = white. Hydrogen bonding represented as red dotted lines .....	41
<b>Figure 3.9:</b> Crystal structure of the mononuclear Cu <sup>II</sup> complex with coordinated NO <sub>3</sub> <sup>-</sup> anions produced by Forgan <i>et al.</i> H atoms, apart from those involved in hydrogen bonding have been omitted for clarity; Cu <sup>II</sup> = orange, N = blue, O = red, C = grey, H = white. Hydrogen bonds represented as red dotted lines.....	42
<b>Figure 3.10:</b> Crystal structure of the mononuclear Ni <sup>II</sup> = green, N = blue, O = red, C = grey, H = white. Hydrogen bonding represented as red dotted lines.....	43
<b>Figure 3.11:</b> Crystal structure of the mononuclear Mn <sup>II</sup> structure produced by Li <i>et al.</i> , which utilises a HSal based ligand. H atoms omitted for clarity; Mn <sup>II</sup> = purple, N = blue, O = red, Cl = green, C = grey.....	44
<b>Figure 3.12:</b> Crystal structure of the mononuclear Cu <sup>II</sup> structure produced by Hindo <i>et al.</i> H atoms omitted for clarity; Cu <sup>II</sup> = orange, O = red, C = grey.....	45
<b>Figure 3.13:</b> Crystal structure of the complex [Cu <sub>2</sub> ( <b>L3'</b> ) <sub>2</sub> Cl <sub>2</sub> ], ( <b>C4</b> ) (left) and the ligand ( <b>L3'</b> ) formed <i>in situ</i> (right). H atoms, apart from those involved in hydrogen bonding, have been omitted for clarity; Cu <sup>II</sup> = orange, N = blue, O = red, B = light pink, F = yellow, Cl = green, C = grey, H = white. Hydrogen bonding is represented by red dotted lines. ORTEP view at 30% probability level.....	46
<b>Figure 3.14:</b> The metallic core of the complex, <b>C4</b> ; Cu <sup>II</sup> = orange, N = blue, O = red, B = light pink, F = yellow, Cl = green, C = grey. ORTEP view at 30% probability level.....	48
<b>Figure 3.15:</b> Plot of $\chi_M T$ vs. $T$ for the complex <b>C4</b> in the $T = 300-2$ K temperature range measured in an applied field of $B = 0.1$ T. The inset shows the VTVB data for <b>C4</b> in	

the  $T = 2-6$  K and  $B = 0-7$  T temperature and field ranges. The solid red lines are a fit of the experimental data to spin-Hamiltonian (**eqn. 4.**) .....49

**Figure 3.16:** Crystal structure of the mononuclear Ni<sup>II</sup> BF<sub>2</sub><sup>+</sup> bridged macrocycle by Prushan *et al.* (top), and the ligand utilised (bottom). H atoms omitted for clarity; Ni<sup>II</sup> = green, N = blue, O = red, S = dark yellow, B = light pink, F = light yellow .....50

**Figure 3.17:** Crystal structure of the dinuclear Fe<sup>III</sup> complex produced by Powell and co-workers (left) and the ligand utilised (right). H atoms omitted for clarity; Fe<sup>III</sup> = orange, N = blue, O = red, Cl = green.....51

**Figure 3.18:** Crystal structure of the complex [Fe<sub>3</sub>O(L4-H)<sub>3</sub>(OAc)<sub>3</sub>], (**C5**). H atoms, apart from those involved in hydrogen bonding, have been omitted for clarity; Fe<sup>III</sup> = orange, N = blue, O = red, H = white. Hydrogen bonding represented as red dotted lines. ORTEP view at 30% probability .....52

**Figure 3.19:** Crystal structure of the complex [Mn<sub>3</sub>O(L4-H)<sub>2</sub>(L4-2H)(OAc)<sub>3</sub>], (**C6**). H atoms, apart from those involved in hydrogen bonding have been omitted for clarity; Mn<sup>III</sup> = purple, N = blue, O = red, H = white. Hydrogen bonding represented as red dotted lines. ORTEP view at 30% probability level. .... 53

**Figure 3.20:** <sup>57</sup>Fe Mössbauer spectrum of the complex, **C5**, at RT (294 K), LNT (77 K), and low T (6.3 K)..... 57

**Figure 3.21:** Crystal structure of **C5**, illustrating the fac coordination of the OAc<sup>-</sup> groups. H atoms omitted for clarity; Fe<sup>III</sup> = orange, O = red, C = grey. ORTEP view at 30% probability level..... 58

**Figure 3.22:** Crystal structure of **C6** illustrating the mer-mer-fac coordination of the OAc<sup>-</sup> anions. H atoms omitted for clarity; Mn<sup>III</sup> = purple, O = red, C = grey. ORTEP view at 30% probability level..... 59

**Figure 3.23:** Plot of the  $\chi_M T$  product versus T for **C5** and **C6** in the T = 290 – 1.8 K temperature range, in an applied field, B = 0.1 T. The solid red lines are a fit of the experimental data ..... 60

**Figure 3.24:** Exchange interaction models for **C5** (left) and **C6** (right) illustrating the exchange interactions found within the complexes. .... 61

**Figure 3.25:** Plot of lowest lying spin states (S) versus energy (E) as obtained from the isotropic fit of the susceptibility data for **C5** (left) and **C6** (right)..... 62

<b>Figure 3.26:</b> Crystal structures of the first known triangular SMM produced Stamatatos et al., looking down at the metallic core (left) and illustrating the fac coordination geometry of the OAc <sup>-</sup> anions (right). Mn <sup>III</sup> = purple, N = blue, O = red.....	63
<b>Figure 3.27:</b> Crystal structure of the Mn <sup>III</sup> triangular SMM produced by Yang et al. (left) and the corresponding ligand used (right). H atoms are omitted for clarity; Mn <sup>III</sup> = purple, N = blue, O = red, Cl = green, C = grey. ....	64
<b>Figure 3.28:</b> The metallic core of the complex, <b>C7</b> , illustrating the defective dicubane topology. The dotted box indicates the 'body' Fe <sup>III</sup> ions (Fe2). Fe <sup>III</sup> = orange, N = blue, O = red, C = grey. ORTEP view at 30% probability level.....	65
<b>Figure 3.29:</b> Crystal structure of the complex [Fe <sub>4</sub> (L3) <sub>2</sub> (OMe) <sub>6</sub> (OH) <sub>6</sub> ], ( <b>C7</b> ). H atoms, apart from those involved in hydrogen bonding, have been omitted for clarity; Fe <sup>III</sup> = orange, N = blue, O = red, C = grey, H = white. ORTEP view at 30% probability level. ....	66
<b>Figure 3.30:</b> <sup>57</sup> Fe Mössbauer spectrum of the complex, <b>C7</b> , at RT (294 K), LNT (77 K), and low T (6.3 K).....	69
<b>Figure 3.31:</b> Crystal structure of the Fe <sup>III</sup> defective dicubane produced by the research group of Gray. H atoms have been omitted for clarity; Fe <sup>III</sup> = orange, O = red, Cl = green, C = grey.....	70
<b>Figure 3.32:</b> The metallic cores of the Ni <sup>II</sup> defective dicubane complexes, <b>C8</b> (left) and <b>C9</b> (right). H atoms omitted for clarity; Ni <sup>II</sup> = light green, N = blue, O = red, Cl = dark green, C = grey. The dotted boxes indicate the Ni <sup>II</sup> 'body' ions (Ni1). ORTEP view at 30% probability level.....	71
<b>Figure 3.33:</b> Crystal structure of the complex [Ni <sub>4</sub> (L2-H) <sub>2</sub> (OAc) <sub>2</sub> (OMe) <sub>2</sub> Cl <sub>2</sub> ](Et <sub>2</sub> O) <sub>3</sub> , ( <b>C8</b> ). H atoms, apart from those involved in hydrogen bonding, have been omitted for clarity; Ni <sup>II</sup> = light green, N = blue, O = red, Cl = dark green, C = grey, H = white. Hydrogen bonding represented as red dotted lines. ORTEP view at 30% probability level.....	72
<b>Figure 3.34:</b> Crystal structure of the complex [Ni <sub>4</sub> (L3-H) <sub>2</sub> (OAc) <sub>2</sub> (OMe) <sub>2</sub> Cl <sub>2</sub> ](MeOH) <sub>2</sub> , ( <b>C9</b> ). H atoms, apart from those involved in hydrogen bonding, have been omitted for clarity; Ni <sup>II</sup> = light green, N = blue, O = red, Cl = dark green, C = grey, H = white. Hydrogen bonding is represented by red dotted lines. ORTEP view at 50% probability level.....	73
<b>Figure 3.35:</b> The metallic cores of the complexes, <b>C8</b> and <b>C9</b> , illustrating the different coordination modes of the R groups. Ni <sup>II</sup> = light green, N = blue, O = red, Cl = dark green, C = grey. ORTEP view at 30% probability level.....	75

<b>Figure 3.36:</b> Plot of the $\chi_M T$ product versus T for <b>C8</b> and <b>C9</b> in the T = 300 – 1.8 K temperature range, in an applied field, B = 0.1 T. The solid red lines are a fit of the experimental data .....	77
<b>Figure 3.37:</b> Plot of lowest lying spin states (S) versus energy (E) as obtained from the isotropic fit of the susceptibility data for <b>C8</b> (left) and <b>C9</b> (right).....	78
<b>Figure 3.38:</b> Crystal structure of the tetranuclear Ni <sup>II</sup> defective dicubane produced by Perlepes et al. (left) and the corresponding ligand utilised (right). Ni <sup>II</sup> = green, N = blue, O = red.....	78
<b>Figure 3.39:</b> Crystal structure of the tetranuclear Ni <sup>II</sup> defective dicubane produced by Slater-Parry et al. (left) and the corresponding ligand (right). Ni <sup>II</sup> = green, N = blue, O = red, Br = dark yellow.....	79
<b>Figure 3.40:</b> Crystal structure of the Ni <sup>II</sup> /Dy <sup>III</sup> complex produced by Zhao et al., which contains a double defective dicubane topology (left). The ligand utilised can be found on the right. Ni <sup>II</sup> = light green, Dy <sup>III</sup> = aqua, N = blue, O = red, Cl = dark green.....	80
<b>Figure A1:</b> Crystal Structure of 5-tert-Butyl-3-(ethoxymethyl)-2-hydroxybenzaldehyde oxime (left). Hydrogen bonded dimers found within the cell (right). H atoms, apart from attached to heteroatoms, have been omitted for clarity; N = blue, O = red, C = grey, H = white. Hydrogen bonding represented as red dotted lines. ORTEP view at 30% probability level. ....	116
<b>Figure A2:</b> <sup>1</sup> H NMR of L2a. Reference solvent peak (CDCl <sub>3</sub> ) at 7.26 ppm. ....	117
<b>Figure A3:</b> <sup>13</sup> C NMR of L2a. Reference solvent peak (CDCl <sub>3</sub> ) at 77 ppm.....	118
<b>Figure A4:</b> <sup>1</sup> H NMR of L3a. Reference solvent peak (CDCl <sub>3</sub> ) at 7.26 ppm. ....	119
<b>Figure A5:</b> <sup>13</sup> C NMR of L3a. Reference solvent peak (CDCl <sub>3</sub> ) at 77 ppm.....	120
<b>Figure A6:</b> <sup>1</sup> H NMR of L2. Reference solvent peak (CDCl <sub>3</sub> ) at 7.26 ppm. ....	121
<b>Figure A7:</b> <sup>13</sup> C NMR of L2. Reference solvent peak (CDCl <sub>3</sub> ) at 77 ppm. ....	122
<b>Figure A8:</b> <sup>1</sup> H NMR of L3. Reference solvent peak (CDCl <sub>3</sub> ) at 7.26 ppm. ....	123
<b>Figure A9:</b> <sup>13</sup> C NMR of L3. Reference solvent peak (CDCl <sub>3</sub> ) at 77 ppm.....	124

## List of Tables

<b>Table 3.1:</b> The metal salts utilised in this research.....	30
<b>Table 3.2:</b> Selected bond lengths of the complexes <b>C1</b> , <b>C2</b> , and <b>C3</b> .....	36
<b>Table 3.3:</b> Selected bond angles of the complexes <b>C1</b> , <b>C2</b> , and <b>C3</b> . ....	36
<b>Table 3.4:</b> Hydrogen bonding distances of the complexes <b>C1</b> , <b>C2</b> , and <b>C3</b> .....	37
<b>Table 3.5:</b> Magnetic susceptibility and magnetic moment results for the complexes <b>C1</b> , <b>C2</b> , and <b>C3</b> . ....	40
<b>Table 3.6:</b> Selected bond lengths of <b>C4</b> . ....	47
<b>Table 3.7:</b> Selected bond angles of <b>C4</b> . ....	47
<b>Table 3.8:</b> Selected bond lengths of the complexes, <b>C5</b> and <b>C6</b> . ....	54
<b>Table 3.9:</b> Selected bond angles of the complexes, <b>C5</b> and <b>C6</b> . ....	55
<b>Table 3.10:</b> Hydrogen bond distances found in the complexes, <b>C5</b> and <b>C6</b> .....	56
<b>Table 3.11:</b> <sup>57</sup> Fe Mössbauer parameters of the complex, <b>C5</b> . $\delta$ , isomer shift; $\Delta E_Q$ , quadrupole splitting; $\Gamma_L$ , line width of the left peak; $\Gamma_R$ , line width of the right peak. ....	56
<b>Table 3.12:</b> Selected bond lengths of the complex, <b>C7</b> . ....	67
<b>Table 3.13:</b> Selected bond angles of the complex, <b>C7</b> . ....	67
<b>Table 3.14:</b> <sup>57</sup> Fe Mössbauer parameters of the complex, <b>C7</b> . $\delta$ , isomer shift; $\Delta E_Q$ , quadrupole splitting; $\Gamma_L$ , line width of the left peak; $\Gamma_R$ , line width of the right peak. ....	68
<b>Table 3.15:</b> Selected bond lengths of the complexes, <b>C8</b> and <b>C9</b> . ....	73
<b>Table 3.16:</b> Selected bond angles of the complexes, <b>C8</b> and <b>C9</b> . ....	74





## Abbreviations

$\chi$	Magnetic susceptibility
$\chi_M$	Molar Magnetic Susceptibility
$D$	Zero field splitting
$\delta$	Isomer shift
$\Delta E_Q$	Quadrupole splitting
$\Gamma_L$	Line width of the left peak
$\Gamma_R$	Line width of the right peak
$E$	Energy
$T_B$	Blocking temperature
$\mu_B$	Bohr magneton
$\mu_{\text{eff}}$	Effective barrier for reversal of magnetisation
$3d$	First row transition metal
$4f$	Lanthanide
$\text{Acac}^-$	Acetylacetonate anion
$\text{Ar}$	Aryl group
$B$	Applied magnetic field
$\text{BF}_4^-$	Tetrafluoroborate anion
$\text{Bn}$	Benzyl group
CCDC	Cambridge Crystallographic Database Centre
$\text{CDCl}_3$	Deuterated chloroform
$(\text{CHO})_n$	Paraformaldehyde
$\text{ClO}_4^-$	Perchlorate anion
DC	Direct current
ESI-MS	Electrospray ionisation mass spectrometry
$fac$	Facial coordination geometry
FT	Fourier transformation
ATR-FTIR	Attenuated total reflection - Fourier transform infrared spectroscopy
HPLC	High performance liquid chromatography
HSal	Salicylaldehyde

H <sub>2</sub> Sao	Salicylaldoxime
H <sub>2</sub> Sai	Salicylaldimine
IPA	Isopropyl alcohol
IS	Isomer Shift
K	Kelvin
LNT	Liquid nitrogen temperature
M	Magnetisation
Me	Methyl group
<i>mer</i>	Meridional coordination geometry
NH <sub>2</sub> OH·HCl	Hydroxylamine hydrochloride
NO <sub>3</sub> <sup>-</sup>	Nitrate anion
OAc <sup>-</sup>	Acetate anion
OH <sup>-</sup>	Hydroxide anion
OMe <sup>-</sup>	Methoxide anion
QS	Quadrupole splitting
QTM	Quantum tunnelling of magnetisation
R <sub>F</sub>	Retention factor
S	Total spin angular momentum
SMMs	Single molecule magnets
SO <sub>4</sub> <sup>2-</sup>	Sulfate anion
SQUID	Superconducting quantum interference device
<sup>t</sup> Bu	<i>Tert</i> -butyl group
XRD	X-ray diffraction
ZFS	Zero field splitting



# 1.0 Introduction

## 1.1 Magnetism

The magnetism found in metallic compounds arises from the magnetic moments generated by the electron spins of the compound. In simple terms, magnetism is the repulsion and/or attraction of two objects, originating from how these objects interact not only with one another but with a magnetic field.<sup>1</sup>

When a metallic object interacts with a magnetic field, the spins of the object's ground state electrons are reorientated such that they become ordered and aligned with the magnetic field, resulting in a measurable magnetisation of the object. Once the object leaves the magnetic field the spins become disordered, rapidly relaxing the magnetisation.<sup>2</sup>

The magnetism found in metallic objects is generally split into two different classes, diamagnetism and paramagnetism. Each class is dependent on the electron configuration of the objects metal ions and produce a different response when interacting with a magnetic field.

Diamagnetic metals are characterised as having no unpaired electrons, this causes an overall magnetic moment of zero and weakly negative magnetic susceptibility, resulting in the repulsion of a magnetic field and subsequently no observable magnetisation. Paramagnetic metals are characterised as having unpaired electrons, resulting in positive magnetic moments and magnetic susceptibility. These properties allow the electron spins to interact and align in the direction of the magnetic field, resulting in magnetisation.<sup>1,3</sup>

For bulk solids, there are additional classes of magnetism: ferromagnetism, antiferromagnetism and ferrimagnetism. These classes of magnetism are temperature dependent and contain properties of both paramagnetism and diamagnetism, however, they are directly related to the alignment of the magnetic dipoles of interacting metal centres. Ferromagnetism is the alignment of magnetic dipoles in the same direction,

whereas antiferromagnetism is the antiparallel alignment of magnetic dipoles. The directionality of the dipoles is generally influenced by bridging groups and/or ligands, which can induce spin polarization on one or more of the metal centres. Ferrimagnetism and antiferromagnetism are closely related in that they have antiparallel spins, however, in ferrimagnetism the magnetic dipoles are not proportional resulting in spontaneous magnetisation.<sup>1,4</sup>

### 1.1.1 Exchange Interactions

An exchange interaction in a metallic complex is defined as the electronic interaction between two metal centres, originating from the mutual overlap of two partially occupied atomic orbitals. A superexchange pathway, while similar, is the result of an overlap between a partially occupied atomic orbital of a metal centre and molecular orbitals of an intermediary or bridging ligand, which can then facilitate further coupling on adjacent metal centres. In polynuclear clusters there exists an angular dependence for which superexchange occurs; antiferromagnetic exchange arises when the angle between two metal centres and a bridging ligand is  $180^\circ$ , as illustrated in Figure 1.1 (left). Ferromagnetic exchange arises when this angle is reduced to  $90^\circ$  by the involvement of a secondary  $p$ -orbital of the ligand (Figure 1.1, right).<sup>5</sup>

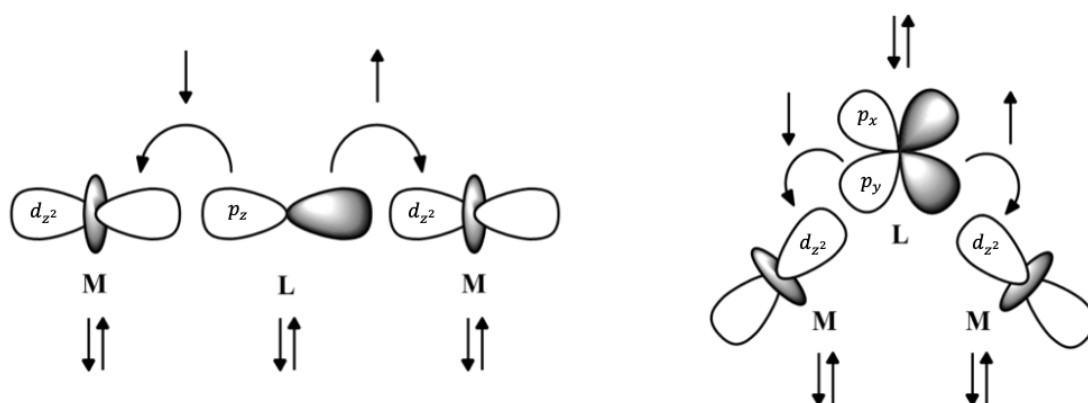


**Figure 1.1:** Schematic representations of antiferromagnetic exchange (left) and ferromagnetic exchange (right).

A prediction on the nature of the superexchange can be made by following the Pauli exclusion principle. The principle dictates that the superexchange between a pair of coupled ions will exhibit antiferromagnetic behaviour if both ions have half-filled orbitals, whereas ferromagnetic behaviour is observed if one orbital is filled and the other half-filled. This generalisation breaks down however if there are multiple exchange pathways present within the complex, as antiferromagnetic exchange will dominate.<sup>5-6</sup>

### 1.1.2 Single Molecule Magnetism

Single molecule magnets (SMMs) are a class of compounds within the field of magnetism, where discrete molecules display molecular based hysteresis and slow relaxation of magnetisation. The magnetism found within a SMM differs from a traditional magnet in that each magnetic domain consists solely of one molecule. Unlike bulk magnetic materials, the magnetic domains in SMMs are well isolated and thus do not interact with each other. The molecular based hysteresis (the magnetic memory required to store data) results directly from metal-ligand interactions and ground spin states, which also result in the slow relaxation and/or retention of magnetisation.<sup>7</sup> The combination of these properties together allow for the potential application of SMMs in quantum computing, spintronic devices, and the most promising, high-density information storage.<sup>3, 8</sup>

In the field of SMMs, three characteristic properties are commonly used for comparison: the blocking temperature ( $T_B$ ), the effective barrier for reversal of magnetisation ( $U_{eff}$ ), and magnetic susceptibility ( $\chi_M T$ ); a temperature dependent indication about the degree to which the metallic complex will become magnetised when interacting with a magnetic field.<sup>1, 9</sup>

The blocking temperature is the maximum temperature at which hysteresis can be observed and hence magnetism is retained, this however, is dependent on the rate at which the magnetisation is measured. This characteristic property in recent years has been the largest obstacle in producing functional SMMs. Until recently, all known SMMs required at least liquid-helium cooling (4 K) for hysteresis to be observed.<sup>3, 10</sup> A large breakthrough was made in 2018 by Guo *et al.* with the record breaking SMM  $[(Cp^{iPr5})Dy(Cp^*)]^+$  ( $Cp^{iPr5}$  = pentaisopropylcyclopentadienyl,  $Cp^*$  = pentamethylcyclopentadienyl) that has a blocking

temperature of 80 K, surpassing the idealised 77 K temperature (the temperature at which nitrogen boils) (Figure 1.2).<sup>7d</sup> The effective barrier,  $U_{eff}$  is the energy barrier that the electron spins must overcome to reorient themselves as either spin up or spin down in order to quench the magnetisation. The barrier correlates to the difference in energy between the lowest and highest ground spin states of the metal centre/s. It has been concluded that in order to achieve a large blocking temperature the effective barrier must also be large.<sup>9a, 10b</sup> This was observed by Guo *et al.* who when producing their record breaking blocking temperature (80 K) also produced a record breaking  $\mu_{eff}$  of 2217 K (1541  $\text{cm}^{-1}$ ). In order to achieve a large barrier, it has been realised that the vital properties are a large ground spin state, and a large negative magnetic anisotropy resulting from zero-field splitting (ZFS) of the ground spin state.<sup>7d</sup>

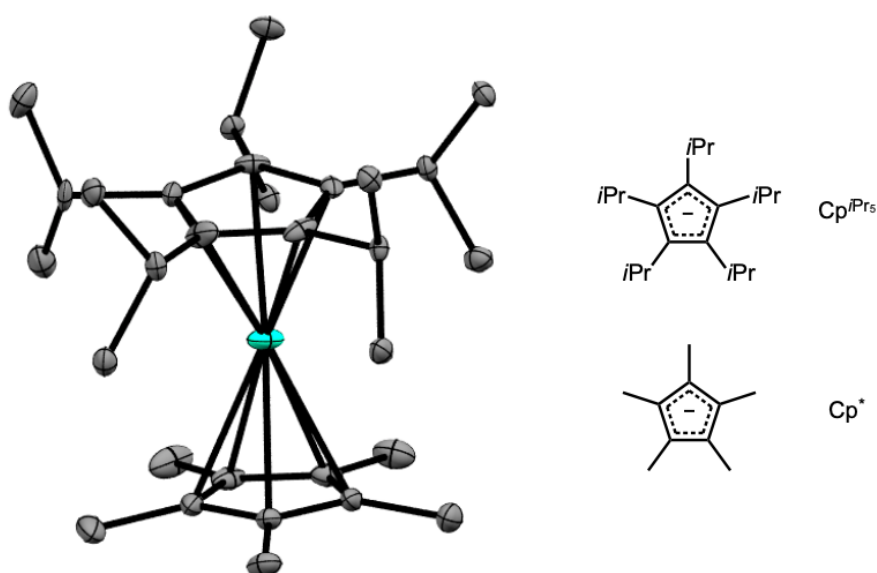


**Figure 1.2:** X-ray structure of the SMM with the record-breaking blocking temperature (80 K). The ligands utilised, Cp<sup>iPr5</sup> and Cp<sup>+</sup>, are on the right. H atoms are omitted for clarity; Dy<sup>III</sup> = aqua, C = grey.

Throughout literature, there is a large range of reported SMMs, varying from single-ion centres of either transition metals (3d) or lanthanides (4f) ions, to mixed metal 3d/3d, 3d/4f, and various other combinations using 4d, 5d, and 5f metal ions. The most common metal ions found in SMMs are Mn<sup>II/III/IV</sup>, Fe<sup>II/III</sup>, Co<sup>II</sup>, Ni<sup>II</sup>, Dy<sup>III</sup>, Tb<sup>III/IV</sup>, Eu<sup>III</sup> and Gd<sup>III</sup>, with SMMs containing Mn ions the most popular due to this metals large uniaxial anisotropy rising from



Jahn-Teller distortions.<sup>11</sup> The Jahn-Teller effect occurs when the electron configuration of a metal ion has doubly degenerate states; this is most commonly seen in  $d^9$  metal ions, but can also be seen in low spin  $d^7$  and high spin  $d^4$  ions. As degenerate states are not energetically favoured, the metal ion will attempt to lower the overall energy of the states by geometric distortion along a given axis.<sup>11e</sup>

## 1.2 Characterisation Techniques

Every complex synthesized in this report (**C1-C9**) has undergone basic characterisation, including techniques such as, ATR-FTIR, ESI-MS, UV/Vis, conductivity, and CHN elemental analysis. In addition to these basic characterisation techniques, more advanced characterisation has been performed; X-ray diffraction was performed on all complexes to elucidate the structure of the complex, Mössbauer spectroscopy was performed on iron complexes **C5** and **C7** to determine the oxidation state, and coordination environment of the iron atoms, and magnetic measurements were performed on complexes **C1-C6**, **C8-C9** to investigate their magnetic properties (magnetic measurements were not performed on **C7** due to reproducibility issues and time constraints).

### 1.2.1 X-ray Diffraction

X-ray diffraction (XRD) is a characterisation technique that irradiates a crystalline material, whether it be powder (PXRD) or a single crystal (SCXRD), with X-rays ( $\lambda$ , order of  $10^{-10}$  m) to obtain a diffraction pattern. The analysis of which provides a 3-D atomic-resolution spatial arrangement of the atoms contained within the crystal.

The diffraction pattern arises from the scattering of X-rays by the atoms electrons (Figure 1.4). The scattering of the X-rays occurs at a specific angle,  $2\theta$ , which is related to an inter-atom distance by the Bragg equation (**eqn. 1**). From the scattering of the X-rays, and the resulting diffraction signals, correlated data can be determined as the X-rays are approximately the same order of magnitude as the distances found between atoms. Additionally, the intensity of the signal can be related to the electron density surrounding an atom through a Fourier transformation (FT).

$$2d \sin \theta = n\lambda \quad (\text{eqn. 1})$$

The Bragg equation (**eqn. 1**) is employed to determine parameters of the diffraction pattern, such as: the distance between lattice planes in the material ( $d$ ) and the scattering angle ( $\theta$ ), using the wavelength of the X-rays ( $\lambda$ ) (Figure 1.3). A diffraction pattern, known as a diffractogram, is a representation of the diffraction intensities ( $I$ ) vs.  $2\theta$ , the Bragg angle. In order to resolve the structure of the crystalline material, a series of diffractograms over a range of scattering angles are measured to produce a file of reflections ( $hkl$ ) with corresponding structural factors ( $F$ ). This file of reflections in conjunction with software can determine cell parameters, the space group of the crystalline material, and ultimately can be used to produce a model structure of the crystalline material.<sup>1</sup> Several assumptions, including the composition of the crystal, are made when calculating a structural model, as the diffraction pattern results from measurements of  $F^2$ , therefore, a Fourier transformation cannot reproduce the real space lattice of the structure. This is known as the 'phase problem' and is a common problem encountered in X-ray crystallography.<sup>12</sup>

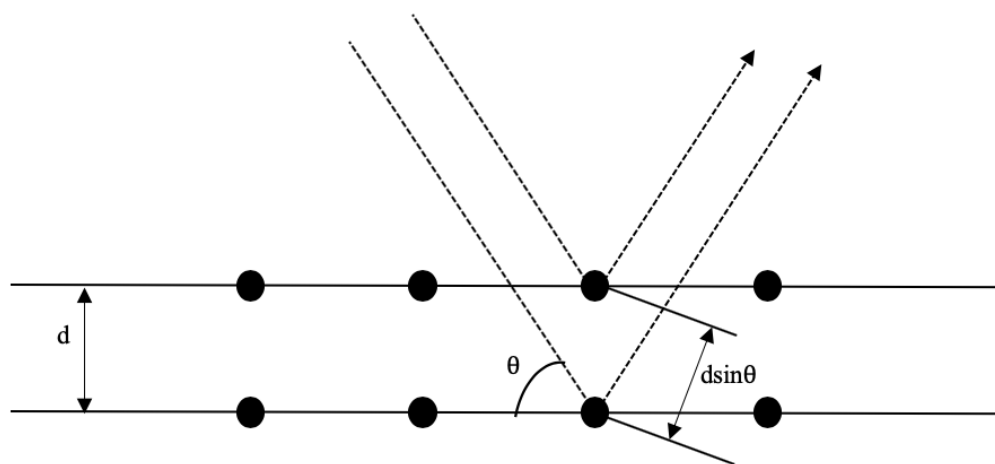


**Figure 1.3:** Schematic representation of the Bragg equation.

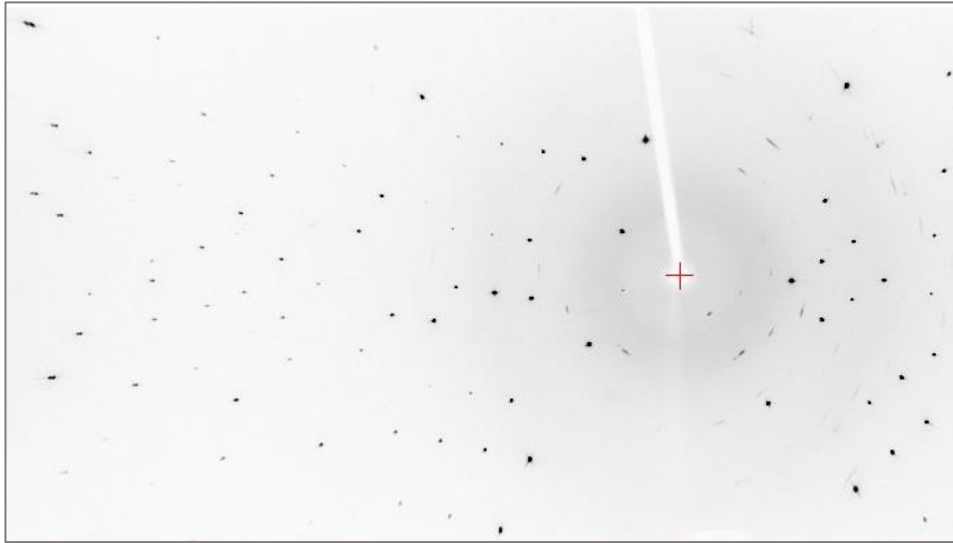


**Figure 1.4:** Example diffraction pattern

### 1.2.2 Magnetic Measurements

Since the 1960s, the most commonly used instrumentation for measuring the magnetic properties of a sample, such as magnetic susceptibility and magnetic moment, is a superconducting quantum interference device (SQUID) magnetometer. Other instruments include Gouy and Faraday balances, however, these instruments are less sensitive and cannot measure samples at low temperatures, which are required to observe magnetic hysteresis.<sup>1, 9e, 13</sup>

A SQUID measures the subtle changes in the magnetic flux ( $\Delta\Phi$ ) of a sample, which is used to determine the magnetic moment of the sample. The changes in a samples magnetic flux, are directly related to the change or reversal of the samples magnetic moment (**eqn. 2**), where  $\alpha$  is the flux coupling factor, a value related to and determined by the positioning and geometry of the instrument and sample.

$$\Delta\Phi = \alpha\Delta M \quad (\text{eqn. 2})$$

The general set up of a SQUID consists of a superconducting loop, interrupted by two parallel Josephson junctions. These Josephson junctions consist of narrow, insulating material where any change in magnetic flux over the material can be observed as a change in voltage. The SQUID is connected to a superconducting coil, where the sample is passed down, generating a current corresponding to the magnetic flux of the sample. This current is passed to the SQUID where any subtle changes in the current are measured. The change in voltage from the SQUID can be manipulated into an output, and the magnetic moment of the sample can be determined.<sup>1, 13a, 14</sup>

### *1.2.3 Mössbauer Spectroscopy*

The Mössbauer effect centres on atomic nuclei found in rigid crystal lattices and their recoilless emission and resonant absorption of nuclear gamma rays.<sup>1</sup> The Mössbauer effect is a characterisation technique that investigates structural properties, electronic, magnetic, and oxidation states of a crystalline solid containing Mössbauer active nuclei.<sup>1, 15</sup> The most commonly measured Mössbauer nuclei is <sup>57</sup>Fe, as it has a sufficient combination of natural abundance, and recoil free fraction ( $f$ ).<sup>15c</sup> The gamma ray source generally utilised is a radioisotope, for <sup>57</sup>Fe the radioisotope is <sup>57</sup>Co (generally in the form of doped stainless steel).

Instrumentation for Mössbauer spectroscopy includes a gamma radiation source, <sup>57</sup>Co, an absorber, where the Fe sample is placed, and a gamma ray detector. Upon the capture of an electron, the <sup>57</sup>Co source decays to an excited state of <sup>57</sup>Fe, which in turn releases gamma radiation as it relaxes back to the ground state. This gamma radiation interacts with the absorber and the sample, if the Fe in the sample matches that of the <sup>57</sup>Fe source, it absorbs the radiation (resonant absorption) and no radiation reaches the detector.<sup>1</sup>

The detector outputs a spectrum (Figure 1.5) of relative velocity vs. %transmittance. The parameters that are then determined, such as isomer shift (IS), quadrupole splitting (QS), and magnetic hyperfine splitting provide information on the electronic structure, oxidation state and magnetic properties.<sup>1, 15b, 15c</sup> The IS ( $\delta$ ) of a sample is directly related to the s-electron density found at the nucleus. This is measured by the difference in gamma-radiation between an absorbing iron source and the emitting source, which have different

s-electron densities.<sup>15c, 16</sup> A limitation of this property is that it is sensitive to shielding from other electrons found in the sample, such as *d*, *p*, and *f*-electrons.<sup>9e, 15c, 16</sup>

QS ( $\Delta E_Q$ ) relates to a nucleus that has a spin quantum number greater than  $\frac{1}{2}$  or has non-degenerate excited states. This causes the electronic charge distribution of the nucleus to be non-spherical, and when an external electric field is applied, the asymmetric charge distribution causes a nuclear energy state to split, producing a doublet. QS can determine various parameters of the nucleus such as oxidation state, spin state, and ligand symmetry.<sup>15b, 15c, 17</sup>

Magnetic hyperfine splitting resembles QS, however instead of an applied electric field splitting an energy state, an applied magnetic field will interact with the magnetic moment of the nucleus and split an energy state. The degree to which the energy state is split is related to the strength of the internal magnetic field at the nucleus. The resulting magnetic hyperfine splitting parameters can be used to determine magnetic properties of the nucleus.<sup>15c, 17</sup>

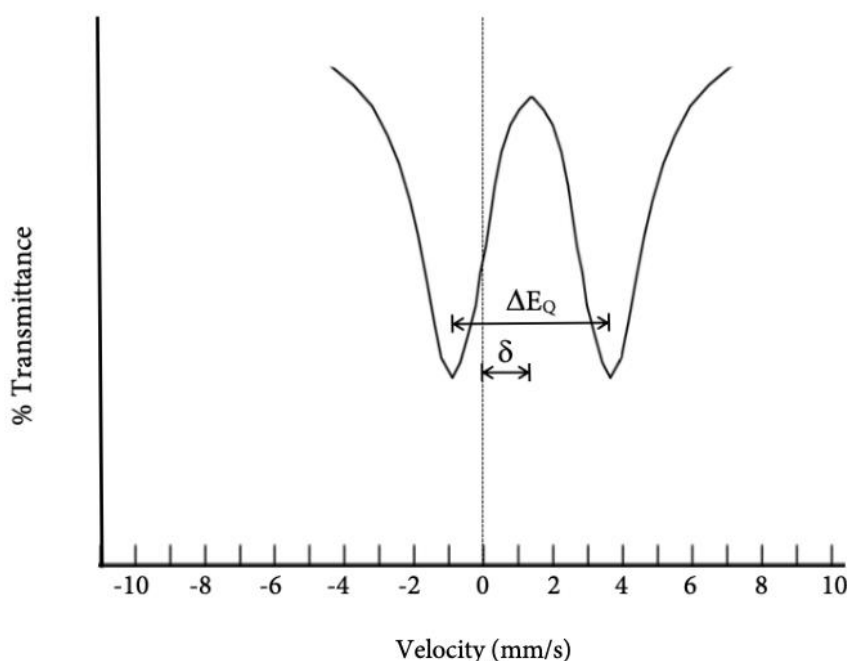


**Figure 1.5:** Illustration of an example Mössbauer spectrum.

### 1.3 Coordination Chemistry of Salicylaldoxime

The use of salicylaldehyde (HSal), salicylaldoxime ( $H_2Sao$ ), and salicylaldimine ( $H_2Sai$ ) derivatives as chelating ligands in metal clusters has grown significantly in recent years, with the first known use of  $H_2Sao$  in a metal complex in 1930.<sup>18</sup> Since then, many HSal,  $H_2Sao$  and  $H_2Sai$  based metal clusters have been synthesised with their properties investigated for application in biological processes, magnetic devices, and hydrometallurgy.<sup>19</sup>

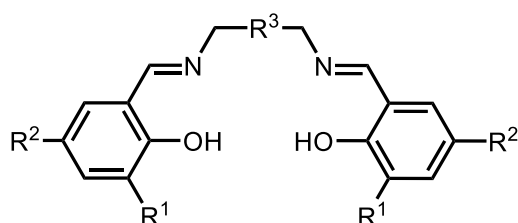


**Figure 1.6:** Schematic illustration of a generalised  $H_2Sai$  ligand.

Throughout the literature, the most common chelating ligands found are  $H_2Sai$  derivatives (Figure 1.6), due to the preorganised binding site. A search on the Cambridge Crystallographic Database Centre (CCDC)(v. 1.20) revealed 12171 entries containing  $H_2Sai$  derivatives. This number greatly outnumbers the 1157 entries found containing  $H_2Sao$  derivatives. As metallic complexes containing  $H_2Sao$  derivatives are less commonly found in literature, they will be the focus of this research.

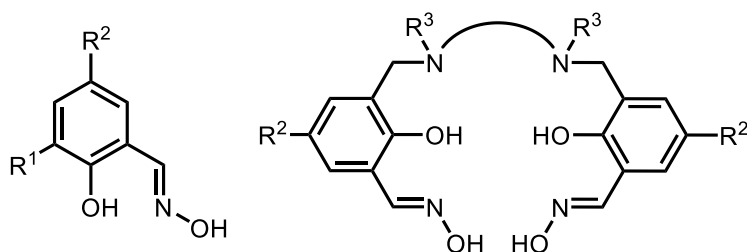


**Figure 1.7:** Schematic representation of generalised single-headed (left) and double-headed (right)  $H_2Sao$  derivatives.

There are two main types of H<sub>2</sub>Sao based molecules, single headed (one basic H<sub>2</sub>Sao unit) or double headed (two basic H<sub>2</sub>Sao units generally joined by a diamine bridge) as shown in Figure 1.7. H<sub>2</sub>Sao derivatives are widely utilised as chelating ligands as they have multiple binding sites for metal ion coordination, this includes a phenolic oxygen atom, oximic nitrogen and oxygen atoms. The different binding sites illustrated in Figure 1.8 are just a few examples of a large variety. The oximic OH has two possible conformations, it can either be deprotonated and coordinate to a metal ion in either a  $\mu_1$  or  $\mu_2$  fashion, or as most commonly found, it can remain protonated and form a hydrogen bond with a phenolic oxygen of an adjacent ligand, providing stability. The phenol readily deprotonates to form either a  $\mu_1$  or  $\mu_2$  bridge between metal ions.

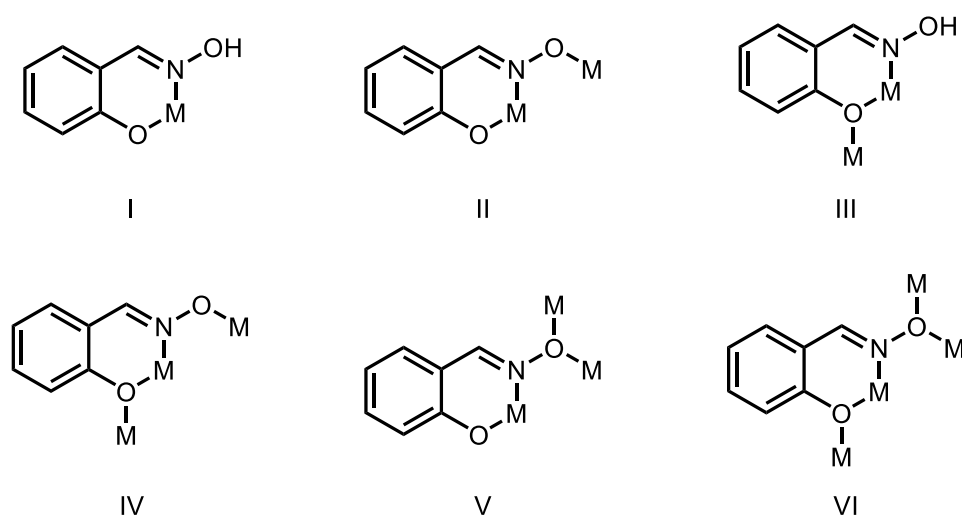


**Figure 1.8:** Schematic representation of a selection of the various coordination modes of H<sub>2</sub>Sao derivatives.

Among the various H<sub>2</sub>Sao based structures found on the CCDC (v. 1.20), many different topologies can be found, with mononuclear and triangular topologies being the most common (Figure 1.9). Mononuclear complexes with H<sub>2</sub>Sao based ligands generally adopt a coordination mode resembling Type I in Figure 1.8, with the ligands arranged in either a *cis* or *trans* conformation. A common application for these Type I structures is extractive hydrometallurgy.<sup>19a, 19b, 20</sup>



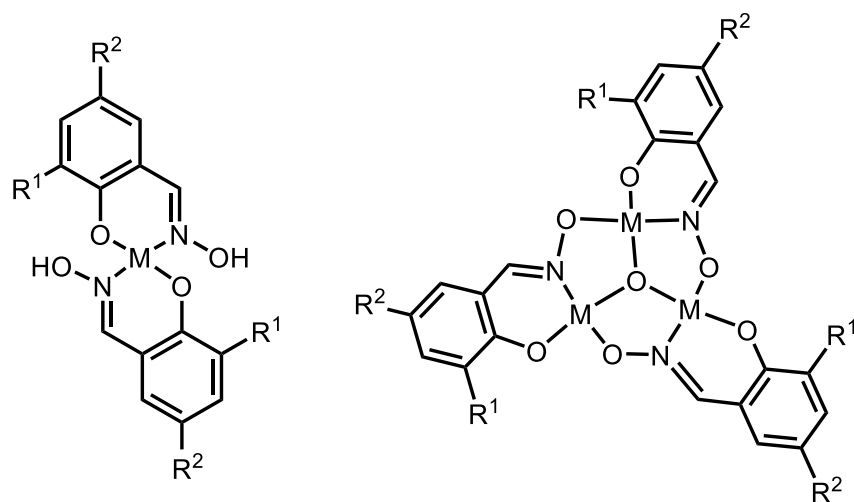


**Figure 1.9:** Schematic representation of generalised H<sub>2</sub>Sao based mononuclear and triangular complexes.

Tasker and coworkers have extensively researched the use of H<sub>2</sub>Sao based ligands for Cu(II) and Ni(II) extraction. The metal cation and anion extractants produced by Tasker and coworkers generally take the form of a single headed H<sub>2</sub>Sao with alkylamino functionality added at the 3-position (R<sup>1</sup> in Figure 1.7, left). Double headed structures are also utilised, however, generally take the form of a H<sub>2</sub>Sai derivative rather than a H<sub>2</sub>Sao derivative.

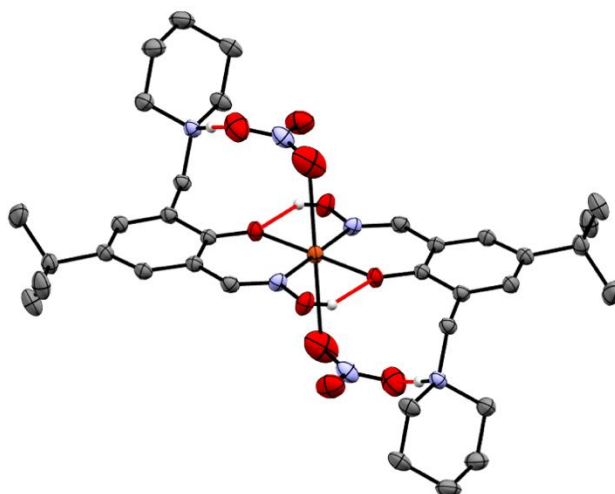


**Figure 1.10:** Crystal structure of a single-headed H<sub>2</sub>Sao based mononuclear Cu<sup>II</sup> complex, which coordinates the Cu<sup>II</sup> ion in a *trans* configuration. H atoms, apart from ones involved in hydrogen bonding, omitted for clarity. Cu<sup>II</sup> = orange, N = blue, O = red, C = grey, H = white. Hydrogen bonding represented as red dotted lines.

The inclusion of an alkylamino group provides a site for anion coordination, in addition to the metal cation extraction. It was found that for the single headed ligands, they typically coordinate a metal cation in the *trans* conformation (Figure 1.10), whereas for the double headed ligands they coordinate the metal cation in a *cis* conformation (Figure 1.11). This is an important factor concerning anion extraction as it has been found that the *cis* arrangement has greater efficiency for extraction of dianions, such as  $\text{SO}_4^{2-}$ , and the *trans* arrangement has greater efficiency for monoanionic extraction ( $\text{BF}_4^-$  and  $\text{NO}_3^-$ ).<sup>19a, 19b, 20-21</sup>

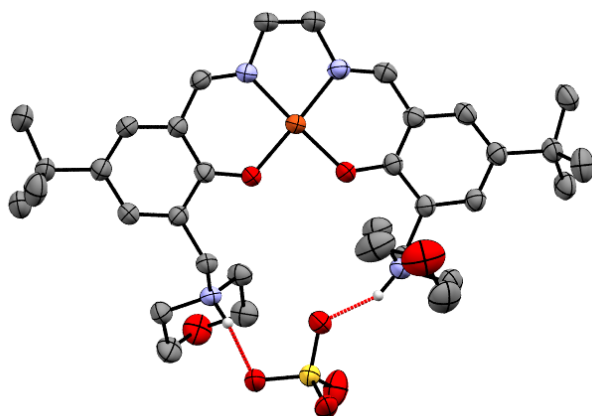


**Figure 1.11:** Crystal structure of a double-headed  $\text{H}_2\text{Sao}$  based mononuclear  $\text{Cu}^{\text{II}}$  complex, which coordinates the  $\text{Cu}^{\text{II}}$  ion in a *cis* configuration. H atoms, apart from ones involved in hydrogen bonding, omitted for clarity.  $\text{Cu}^{\text{II}}$  = orange, N = blue, O = red, S = yellow, C = grey, H = white. Hydrogen bonding represented as red dotted lines.

The triangular topology (Figure 1.9, right) regularly appears in  $\text{H}_2\text{Sao}$  based metallic clusters, as single triangular units or a network of bridged triangles. The basic triangular structure consists of three ligands (coordination resembling Type II in Figure 1.8), three metal cations (Mn being the most common), and a central  $\mu_3$ -oxo group (generally resulting from residual  $\text{H}_2\text{O}$  in the solvent and/or metal salt).<sup>22</sup> The remaining coordination sites are filled by anions and/or solvent molecules to produce a single triangular structure, or for larger networks, the sites are occupied by bridging atoms/groups such as hydrolysed solvent and/or water molecules, deprotonated phenols, and halides. The  $\text{H}_2\text{Sao}$  based ligands utilised for triangular structures are typically single headed, often derivatised in the 3-position (Figure 1.7, left). Double-headed  $\text{H}_2\text{Sao}$  based triangular structures exist, however they are less commonly found in literature.<sup>23</sup>

One potential application for triangular complexes is in magnetic materials, namely SMMs. In 2007, Brechin and coworkers produced a record breaking SMM that consisted of two  $\text{Mn}^{\text{III}}$  triangles bridged through  $\mu_2$ -oximic oxygen atoms (Figure 1.12, left). The ligand that was utilised to produce this structure was 2-hydroxyphenylpropanone oxime (Figure 1.12, top right). Each  $\text{Mn}^{\text{III}}$  ion is coordinated by a phenolic oxygen, oximic nitrogen and oximic oxygen from an adjacent ligand. The remaining coordination sites are completed by carboxylate groups (3,5-dimethylbenzoic acid) and solvent molecules (EtOH). Brechin and coworkers found that by inducing structural distortion in the Mn-N-O-Mn angle of the triangles, the magnetic exchange could be switched from antiferromagnetic to ferromagnetic, even with the triangles antiferromagnetically coupled and the dominant magnetic exchange interaction being antiferromagnetic. The result was a SMM with a ground state of  $S = 12$  and  $D = -0.43 \text{ cm}^{-1}$ , a barrier to magnetisation reversal of 86.4 K ( $124.33 \text{ cm}^{-1}$ ), and a blocking temperature of 4 K.<sup>24</sup>

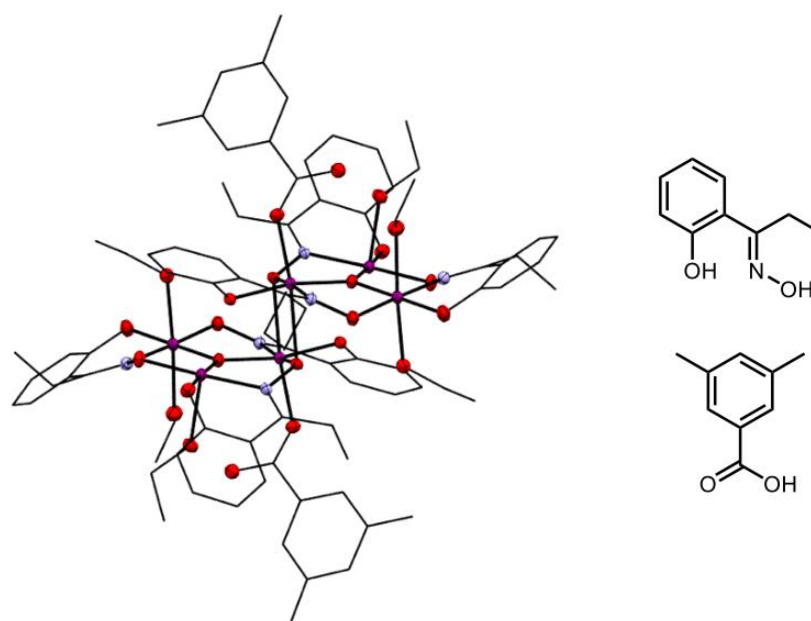


**Figure 1.12:** Crystal structure of the  $\text{Mn}^{\text{III}}$  triangle produced by Brechin and coworkers (left) and corresponding ligands and co-ligands (right). H atoms omitted for clarity;  $\text{Mn}^{\text{III}}$  = purple, N = blue, O = red.

The triangular SMM produced by Yang *et al.* (Figure 1.13, left) utilises the large single ion anisotropy of  $\text{Mn}^{\text{III}}$  ions to produce an anisotropy barrier of 58 K ( $83.46 \text{ cm}^{-1}$ ).<sup>25</sup> Yang *et al.*

used a similar ligand (a methyl ketoxime instead of an ethyl ketoxime) as used by Brechin and coworkers above, however, they produced a Mn<sup>III</sup> complex with a single triangular topology. The metallic core of the triangular structure resembles that of a typical triangle; the Mn<sup>III</sup> ions are coordinated to phenolic oxygen and oximic nitrogen atoms and an oximic oxygen atom from an adjacent ligand. The remainder of the coordination sites are completed by solvent molecules (MeOH), and a capping ClO<sub>4</sub><sup>-</sup> anion. The ClO<sub>4</sub><sup>-</sup> anion elongates the axial coordination of each metal ion, inducing the Jahn-teller elongation effect on the Mn<sup>III</sup> ions. The addition of a methyl group at the oxime creates a structural distortion on the oximato bridge between the Mn<sup>III</sup> ions. The combination of the structural distortion and Jahn-Teller elongation produces a large single ion anisotropy for the Mn ions resulting in the large anisotropy barrier.<sup>25</sup>

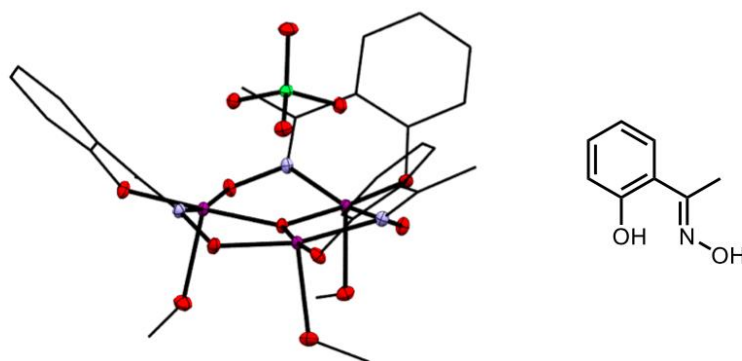


**Figure 1.13:** Crystal structure of the Mn<sup>III</sup> triangular SMM produced by Yang *et al.* (left) and the corresponding ligand (right). H atoms omitted for clarity; Mn<sup>III</sup> = purple, N = blue, O = red, Cl = green.

A third topology commonly found utilising HSal/H<sub>2</sub>Sao/H<sub>2</sub>Sai based ligands is a defective dicubane, more commonly known as a 'butterfly' structure. These tetranuclear structures are composed of two face-sharing cubanes, each with an opposite corner missing; the two central metal ions are nicknamed the body and two outer metal ions are the wingtips, as illustrated in Figure 1.14.<sup>26</sup> The nomenclature is used as it is common to obtain complexes where the body ions differ from the wings, whether it be different oxidation states or different metals.<sup>8f, 27</sup> There are many different applications for H<sub>2</sub>Sao based defective dicubanes, with a few being magnetic materials (SMMs), photoluminescent devices, and catalysis.<sup>27c, 28</sup>

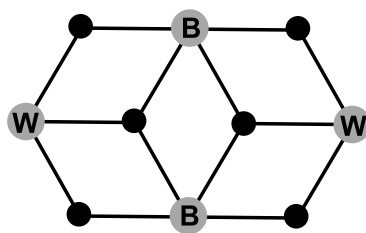


**Figure 1.14:** Schematic representation of the defective dicubane topology; B = body metal ions, W = wingtip metal ions.

The complexes with defective dicubane topologies are most commonly seen in SMMs, as a key feature of the dicubane is the various exchange pathways present (discussed in Section 1.1.1). It has been found that the exchange interactions are a crucial factor in enhancing the magnetic properties of a complex, as large exchange couplings have the ability to decrease quantum tunnelling of magnetisation (QTM) within the complex, in turn, increasing energy barriers and blocking temperatures.<sup>7a, 7g, 27c, 29</sup> One method for enhancing specific exchange interactions is to change the group bridging the metal ions.<sup>29</sup>

The effect of bridging groups between the body ions on the direct exchange interaction and surrounding interactions was investigated by Jiang *et al.*<sup>28b</sup> The ligand utilised in the two tetranuclear Ni(II) complexes was a H<sub>2</sub>Sai derivative that occupied all coordination sites of the metal ions, apart from the  $\mu_3$ -bridges (Figure 1.15). A comparison was made between azide bridging and methoxide bridging; it was found that the azide bridges increase the exchange interaction of the direct body-body coupling, with the exchange interaction between the body and wing ions weaker. This was expected as azide end on bridging ( $\mu_3$ -1,1,1) is known to induce ferromagnetic coupling between metal centres.<sup>30</sup> The opposite was found for methoxide bridges, as the body-body coupling was weaker but the body-wing coupling was greater than the azide bridging.<sup>28b</sup>

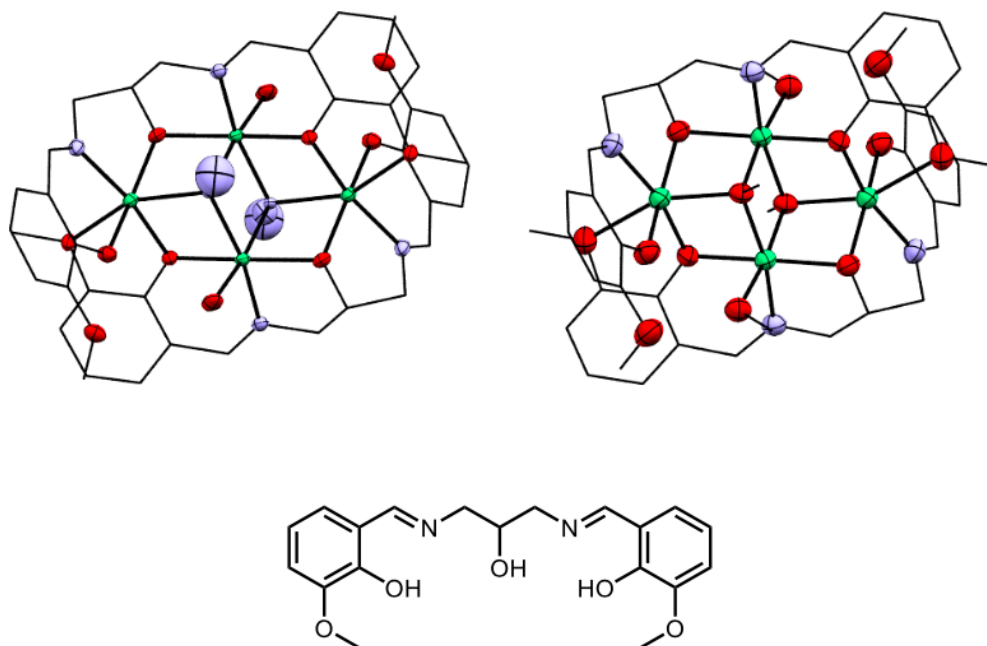


**Figure 1.15:** Crystal structures of the two Ni<sup>II</sup> defective dicubane complexes produced by Jiang *et al.* (top) and corresponding ligand utilised for both complexes (bottom). H atoms omitted for clarity; Ni<sup>II</sup> = green, N = blue, O = red.

When synthesising  $3d/4f$  complexes with defective dicubane topologies, not only does the bridging groups and their properties need to be considered, but also the metal ions used themselves. Peng *et al.* compared the magnetic properties of two isostructural  $3d/\text{Dy}^{\text{III}}$  defective dicubanes, and the effect of paramagnetic Co(II) ions vs. diamagnetic Zn(II) ions.<sup>27c</sup> It was found that the magnetic susceptibility for the Co<sup>II</sup>/Dy<sup>III</sup> complex was  $30.21 \text{ cm}^3 \text{ K mol}^{-1}$  and  $28.79 \text{ cm}^3 \text{ K mol}^{-1}$  for the Zn<sup>II</sup>/Dy<sup>III</sup> complex (Figure 1.16). These values indicated that the majority of the complexes magnetic susceptibility was a result of the large single ion anisotropy of the Dy<sup>III</sup> ions. As the magnetic susceptibility of the Co<sup>II</sup>/Dy<sup>III</sup> complex was greater, it could be thought that the complex would have the greater effective barrier,  $\mu_{\text{eff}}$ . However, Peng *et al.* found that the Zn<sup>II</sup>/Dy<sup>III</sup> complex had the greater  $\mu_{\text{eff}}$  of  $140.4 \text{ K}$  ( $202.04 \text{ cm}^{-1}$ ), with the  $\mu_{\text{eff}}$  of the Co<sup>II</sup>/Dy<sup>III</sup> complex,  $104.8 \text{ K}$  ( $150.81 \text{ cm}^{-1}$ ). The reason for these unexpected results was found to be the result of strong exchange interactions between the Co<sup>II</sup> and Dy<sup>III</sup> ions, a feature of  $3d/4f$  complexes that can enhance the magnetic properties, but can also decrease the magnetic properties when the interaction becomes too large.<sup>27c</sup>

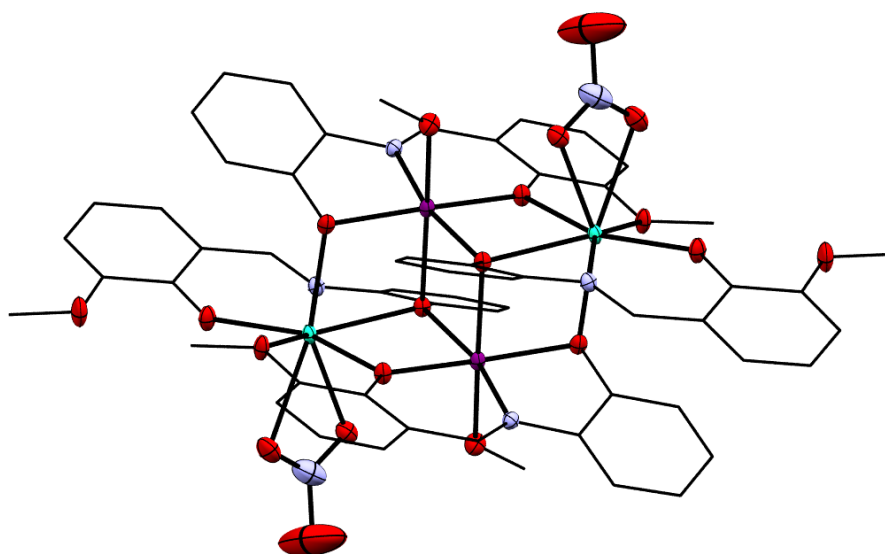


**Figure 1.16:** Crystal structure of the Zn<sup>II</sup>/Dy<sup>III</sup> defective dicubane complex produced by Peng *et al.* H atoms omitted for clarity; Zn<sup>II</sup> = purple, Dy<sup>III</sup> = aqua, N = blue, O = red.

Since 2016, the use of H<sub>2</sub>Sao based ligands in the synthesis of clathrochelate complexes (a complex where the coordination sites of a metal ion are completely filled by a single macrocyclic ligand) has dramatically risen.<sup>31</sup> These clathrochelate complexes are either boron-capped or boron bridged di- and tri-oximate species (larger oximate species are possible but not as commonly found in literature), which have arisen from a condensation reaction between an oxime and a boron source, generally either boronic acids, boron trifluoride etherates, or BF<sub>4</sub><sup>-</sup> anions (Figure 1.17).<sup>31-32</sup> During the complexation of these structures, the capping and/or bridging by borate groups results in the formation of new ligands *in situ*, generally in the form of macrocyclic ligands. These macrocyclic ligands are regularly used as building blocks for supramolecular structures, such as metal-organic frameworks (MOFs), with other applications including molecular magnetism and catalysis.

Research has shown that the complexations which use boronic acids or boron trifluoride etherates commonly result in capped structures, with the structures generally retaining the functionality of the boron source.<sup>31-32</sup> In contrast to this, the hydrolysis of BF<sub>4</sub><sup>-</sup> anions has been shown to form borate or fluoroborate bridges. The hydrolysis of the anions is thought to be assisted by a preformed metal complex in mildly basic conditions.<sup>32b</sup>

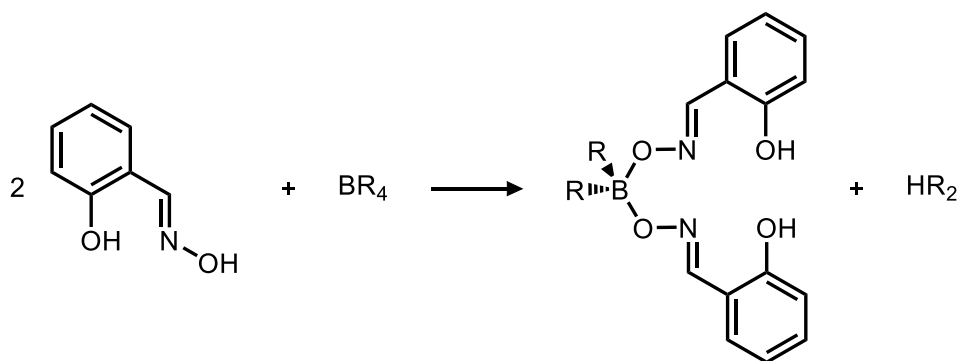


**Figure 1.17:** Generalised synthetic route for the *in situ* condensation reaction between oximic ligands and a boron source (typically either boronic acids, boron trifluoride etherates, and  $BF_4^-$  anions).

In 2017, Martinez *et al.* synthesised a mononuclear Cu(II) boron-bridged clathrochelate complex (Figure 1.18, left).<sup>33</sup> The complex was synthesised by an aqueous condensation reaction between the ligand, methyl-(2-pyridyl)-ketone oxime (mpkoH) and the metal salt  $Cu(BF_4)_2 \cdot 6H_2O$ ; the result of this reaction was a new ligand formed *in situ* (Figure 1.18, right). This complex is one of a very limited number of  $BF_2^+$  bridged complexes formed by the hydrolysis of  $BF_4^-$  anions.<sup>34</sup> The magnetic properties of this complex were investigated, and it was found that the square pyramidal Cu(II) ion was antiferromagnetic.

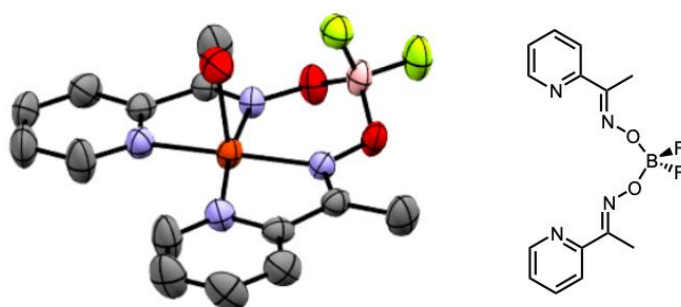


**Figure 1.18:** Crystal structure of the  $Cu^{II} BF_2^+$  bridged clathrochelate complex (left) and ligand produced *in situ* (right). H atoms omitted for clarity;  $Cu^{II}$  = orange, N = blue, O = red, B = light pink, F = yellow.



## 1.4 Aims of Research

The aim of this research was to synthesis and characterise a series of H<sub>2</sub>Sao based ligands capable of coordination to 3*d* ions. The H<sub>2</sub>Sao based ligands will all have the bulky *tert*-butyl group added in the 5-position, and will differ by the alkylamino functionality added at the 3-position (Figure 1.17, left). Following synthesis and purification, all new ligands will be characterised by a series of techniques such as: NMR, ATR-FTIR, ESI-MS, UV/Vis, and CHN elemental analysis.

A series of complexations and recrystallisations utilising a combination of 3*d* and 4*f* ions will be performed. The metal ions used, were chosen for a number of different reasons, including, their potential magnetic properties, their varied affinities for H<sub>2</sub>Sao derivatives, and inspiration from the literature. Any complexes synthesised will be fully characterised using the same techniques used for the ligands, but also characterised by X-ray crystallography, Mössbauer spectroscopy, and magnetic susceptibility measurements to determine the magnetic properties of the complexes.

## 2.0 Ligand Design and Synthesis

The Plieger group in the past has had success in producing double-headed  $H_2Sao$  metal clusters, with the focus on application as anion-binding capsules.<sup>23c, 35</sup> As single-headed  $H_2Sao$  derivatives have not been the sole focus of the Plieger group before, the ligand design will focus on single-headed  $H_2Sao$  derivatives.

### 2.1 General Ligand Design

Four  $H_2Sao$  based ligands were proposed (Figure 2.1) with each ligand differing by the incorporated secondary amine functionality (R in Figure 2.1). The initial goal of this research was to produce heterometallic  $3d/4f$  complexes, as  $H_2Sao$  based ligands are known to strongly coordinate  $3d$  ions, and the addition of oxygen rich secondary amines was proposed to coordinate the  $4f$  ions. The choice to modify the 3-position with a secondary amine was due to a simpler and more straightforward synthesis.

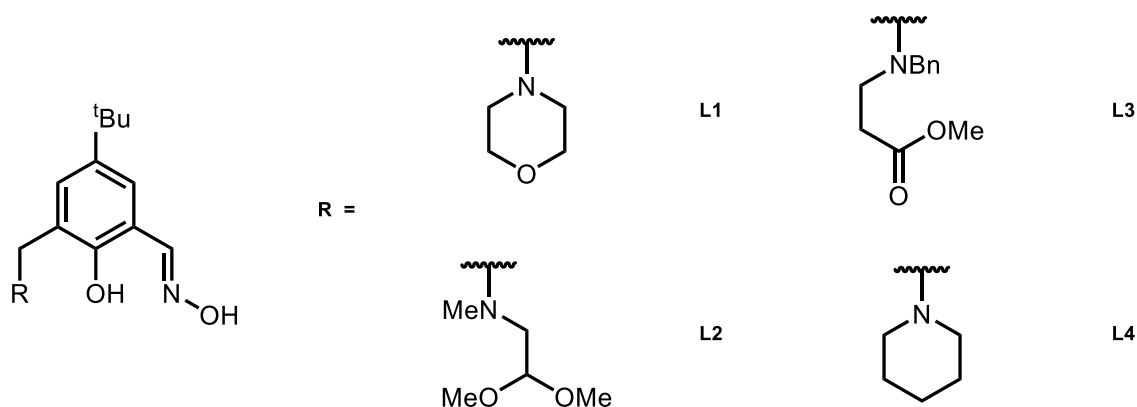


**Figure 2.1:** Schematic representation of the four different ligands utilised in this research.

In the past, the Plieger group has had success in forming Fe(III) hexanuclear and heptanuclear cluster complexes using the ligands 5-methyl-3-(morpholinomethyl)-2-hydroxybenzaldehyde oxime and 5-methyl-3-(piperidinylmethyl)-2-hydroxybenzaldehyde oxime, derivatives of **L1**, and **L4** respectively.<sup>36</sup> The initial reasons for synthesising both **L1** and **L4** was to reproduce these cluster complexes, but at the same time, incorporate central 4*f* ions into the hexa- and hepta-cluster complexes. As 4*f* ions are highly oxophilic, the incorporation of an oxygen atom in the secondary amine for **L1** was to provide additional donor atoms for a 4*f* ion.

As the two proposed binding sites for **L1** and **L4** are in close proximity, the oxophilic binding sites on **L2** and **L3** were designed to have greater flexibility and increase the possibility for 4*f* ion coordination. The oxygen donor atoms chosen for **L2** and **L3** were ether and ester functional groups respectively. The ether and ester functionalities were chosen as there exists a large number of reported HSal/H<sub>2</sub>Sao/H<sub>2</sub>Sai derivatives with ether and ester donor atoms used in metal ion coordination.<sup>37</sup>

All ligand syntheses started from the formylation reaction of 4-*tert*-butylphenol following an adapted version of Aldred *et al.*, with the resulting aldehyde (5-*tert*-butyl-2-hydroxybenzaldehyde (**1**)) purified by column chromatography to give an average yield of 50%.<sup>38</sup> A methylbromination reaction was performed on the purified aldehyde as per the method of Meier *et al.*, with the resulting product 5-*tert*-butyl-3-bromomethyl-2-hydroxybenzaldehyde (**2**) purified by hot recrystallisation from pentane with an average yield of 66%.<sup>39</sup> The secondary amine used for **L3**, *N*-benzyl-β-alanine methyl ester, was prepared as per the method of Cruz-Huerta *et al.* achieving an average yield of 95%.<sup>40</sup> The coupling reactions of **2** with the chosen secondary amines followed an adapted method of Stevens and Plieger.<sup>41</sup> The final step in the syntheses, an oximation reaction, followed an adapted method of De Silva *et al.*<sup>35e</sup>

## 2.2 General Synthesis

The syntheses of the ligands **L1-L4** all involved a coupling reaction between **2** and the chosen secondary amine, followed by an oximation reaction as illustrated in the general reaction scheme below (Figure 2.2).

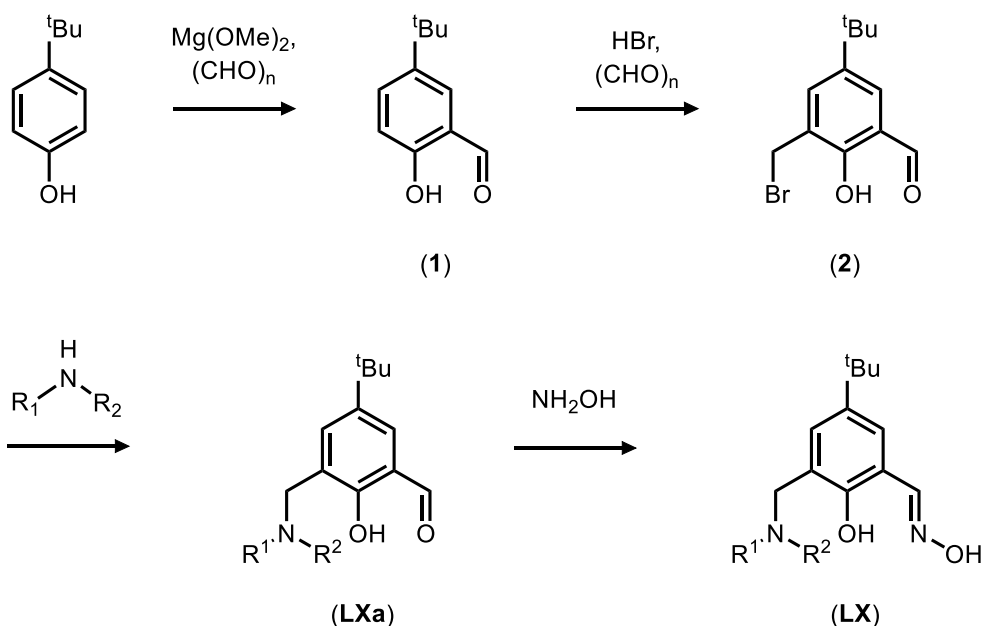


**Figure 2.2:** Generalised reaction scheme for the synthesis of ligands **L1-L4**.

The ligand precursors **L1a** and **L4a** are known compounds, with many preparations found in literature, however, the most common syntheses found are between **1**, the secondary amines (morpholine or piperidine) and paraformaldehyde.<sup>42</sup> Due to past success in the Plieger group, and recent literature methods for using **2** in coupling reactions, the other literature methods were not used. By starting with **2** for the coupling reaction, an amine alkylation reaction can be employed, for which many different procedures can be found throughout the literature.<sup>35a, 43</sup> Generally, these alkylation reactions are performed at RT in basic solutions with common solvents being DCM, THF, or  $\text{Et}_2\text{O}$ . The procedure that was chosen to synthesise **L1a-L4a** was the method of Stevens and Plieger, which used  $\text{Et}_3\text{N}$  as the base, DCM as the solvent and reported a yield of 97%.<sup>41</sup>

For the amine alkylation reactions, solutions of **2** and the corresponding secondary amine, both in DCM, were added dropwise to an Et<sub>3</sub>N/DCM solution and stirred at RT for 24 hours. After purification, yields of 48% - 97% were obtained. The large range of yields was suspected to be a result of the washing step; in an attempt to improve this, the solvent was changed to CHCl<sub>3</sub>. Following this revised method, higher average yields of 85% - 98% were obtained. Ligand precursors **L1a**, **L2a**, and **L4a** did not require further purification, as determined by <sup>1</sup>H NMR.

**L3a**, on the other hand required column chromatography for purification. Initially, the synthesis of **L3a** proceeded using crude amine (*N*-benzyl-β-alanine methyl ester), and purified **2**; the <sup>1</sup>H NMR indicated a successful reaction, with an impurity present (22%), carried through from the crude amine. Column chromatography was performed using the conditions (4:1, *n*Hex : EtOAc) from the literature purification of *N*-benzyl-β-alanine methyl ester. The results found that the same impurity (thought to be the double addition of methyl acrylate to benzyl amine) still remained, although in a reduced amount (approximately 8% instead of the previous 22%). The column conditions were optimised, and it was found that an eluent of *n*Hex/Et<sub>2</sub>O (1:1) gave pure **L3a** with a yield of 87%.

The final step to form the ligands involved an oximation reaction. For H<sub>2</sub>Sao based derivatives, many procedures can be found throughout literature.<sup>19e, 44</sup> These procedures generally include NH<sub>2</sub>OH·HCl, base, such as KOH, NaHCO<sub>3</sub>, or NH<sub>4</sub>OAc, and are performed at RT in solvents such as H<sub>2</sub>O, EtOH or DCM.<sup>35e, 45</sup> The chosen procedure for the oximation of all ligands (**L1-L4**) was an adaption of the procedure by De Silva *et al.*<sup>35e</sup> A solution of NH<sub>2</sub>OH·HCl was neutralised with a solution of KOH, both in EtOH; the filtrate was added dropwise to **L1a** in EtOH and stirred at RT for 24 hours. The procedure for all of the ligands was identical to the literature method up until the H<sub>2</sub>O wash step. As EtOH and H<sub>2</sub>O are miscible, the crude EtOH solution was concentrated *in vacuo*, redissolved in CHCl<sub>3</sub>, then washed with water and concentrated again *in vacuo* to obtain the ligands, **L1-L4** in good yield (65% - 97%). The syntheses were straightforward and they could be scaled up to approximately five grams of **2** per reaction.

## 2.3 General Ligand Characterisation

### 2.3.1 NMR Interpretation of the Ligands and their Precursors

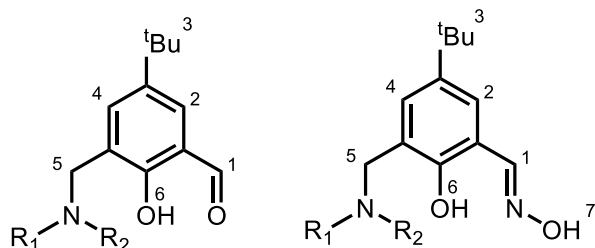


**Figure 2.3:** The numbering system used for  $^1\text{H}$  NMR spectra.

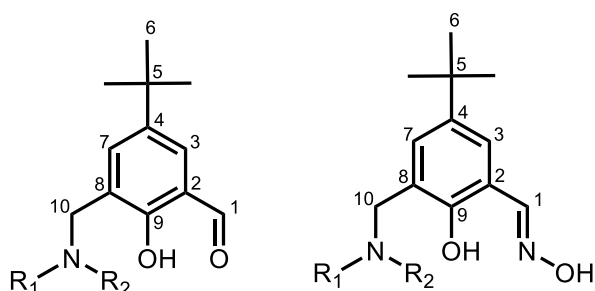


**Figure 2.4:** The numbering system used for  $^{13}\text{C}$  NMR spectra.

For both the  $^1\text{H}$  NMR and  $^{13}\text{C}$  NMR spectra of the final ligands, and their aldehyde precursors, the peaks corresponding to the general aromatic region do not shift significantly, allowing for the numbering of the corresponding peaks to be kept consistent (Figures 2.3 and 2.4).

A successful coupling reaction between **2** and the secondary amines utilised was confirmed by the appearance of the following peaks: singlets at  $\delta$  1.29-1.34 ppm, 3.71-3.79 ppm, and 10.22-10.41 ppm corresponding to the  $^t\text{Bu}$  group, methylene bridge, and carbonyl proton respectively; as well as doublets at  $\delta$  7.35-7.54 ppm, and 7.58-7.65 ppm corresponding to the two aromatic protons (Figure 2.5).

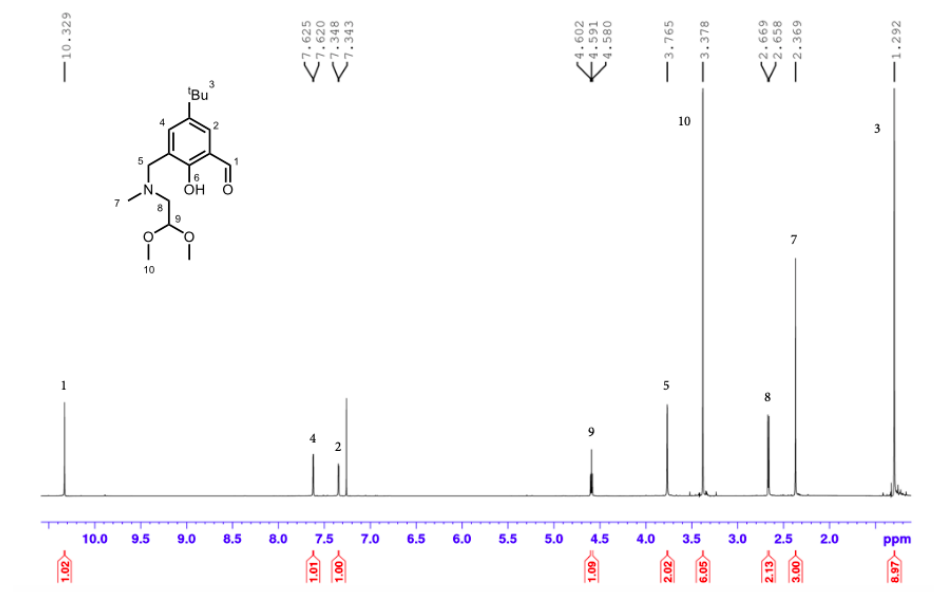


**Figure 2.5:** Example  $^1\text{H}$  NMR of the ligand precursor, **L2a**. Residual solvent ( $\text{CDCl}_3$ ) at 7.26 ppm.

Confirmation of a successful oximation reaction was identified in the  $^1\text{H}$  NMR by the shifting, disappearance and/or appearance of peaks. The aromatic doublets shift to 7.05-7.17 ppm, and 7.43-7.48 ppm; the peak corresponding to the aldehyde proton disappears, and a new peak appears at 8.42-8.45 ppm corresponding to the new oximic proton (Figure 2.6).

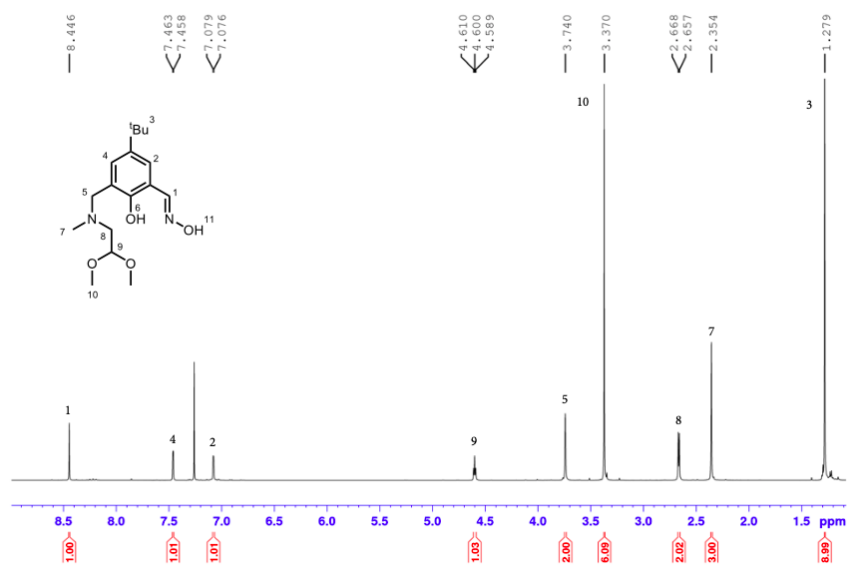


**Figure 2.6:** Example  $^1\text{H}$  NMR of the ligand, **L2**. Residual solvent ( $\text{CDCl}_3$ ) at 7.26 ppm.

As **L1a**, **L1**, **L4a**, and **L4** are known molecules, only the ligands **L2** and **L3**, and their precursors **L2a**, and **L3a** were characterised by  $^{13}\text{C}$  NMR (Figures 2.7 and 2.8), and various 2D NMR techniques such as COSY, NOESY, Dept, HMQC, and HMBC.

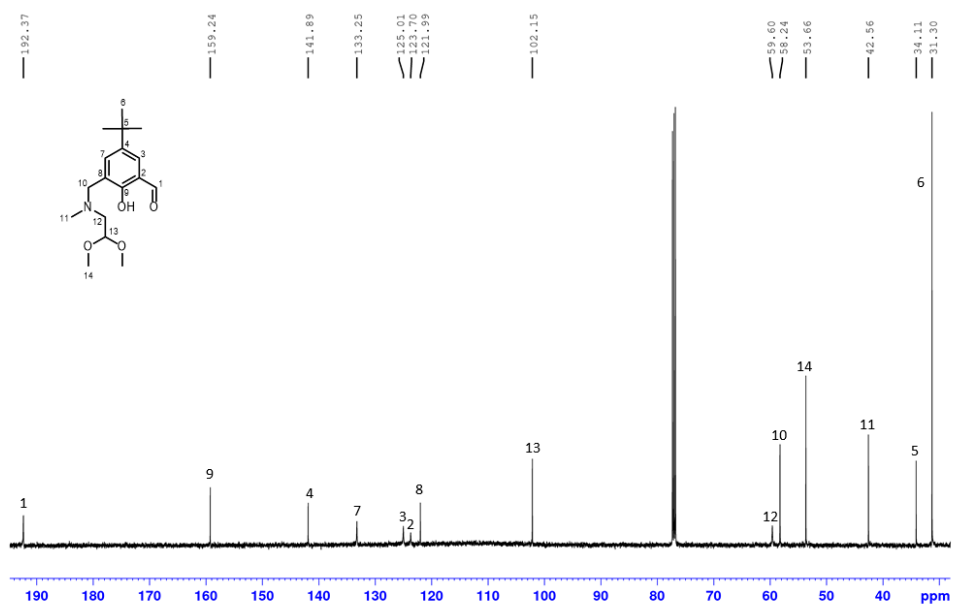


**Figure 2.7:** Example  $^{13}\text{C}$  NMR of the ligand precursor, **L2a**. Residual solvent ( $\text{CDCl}_3$ ) at 77 ppm.

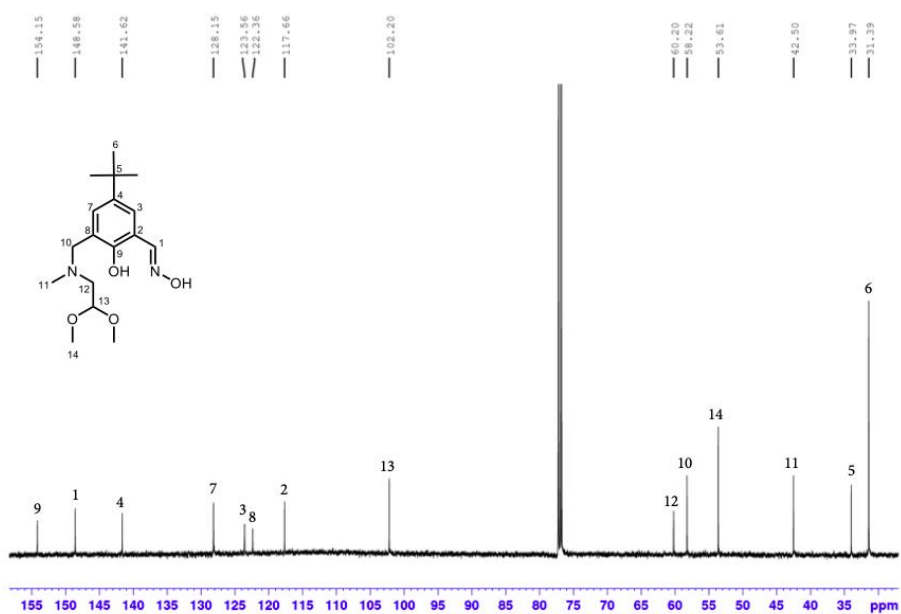


**Figure 2.8:** Example  $^{13}\text{C}$  NMR of the ligand, **L2**. Residual solvent ( $\text{CDCl}_3$ ) at 77 ppm.



### *2.3.2 IR Interpretation of the Ligands and their Precursors*

Attenuated total reflectance - Fourier transform infrared (ATR-FTIR) spectroscopy in the range 700 – 4000  $\text{cm}^{-1}$  was performed on all ligands and their precursors to confirm that the functional group transformations had been successful.

ATR-FTIR was used to determine and confirm that aldehyde precursors (**L1a-L4a**) had successfully been synthesised. The main identifier to this was the appearance of a peak at approximately 1670-1680  $\text{cm}^{-1}$  corresponding to the C=O stretch of the aldehyde.

This form of characterisation was also used to determine the outcome of the oximation reactions and whether the ligands, **L1-L4** had successfully been synthesised. A successful reaction was observed by the appearance of a strong peak between 1610-1630  $\text{cm}^{-1}$  confirming the presence of a C=N stretching mode in the ligand, and the disappearance of a strong peak at approximately 1678  $\text{cm}^{-1}$  confirming the aldehyde C=O stretch no longer remained.

Additional confirmation of a successful reaction for both the precursors and final ligands, was the presence of the following peaks: O-H (3400-3050  $\text{cm}^{-1}$ ), C-H (2960-2950  $\text{cm}^{-1}$ ),  $\text{CH}_2$  (1450-1470  $\text{cm}^{-1}$ ),  $^t\text{Bu}$  (1390-1400  $\text{cm}^{-1}$ ), O-H (1360-1365  $\text{cm}^{-1}$ ), C-N (1110-1130  $\text{cm}^{-1}$ ), and N-O (940-965  $\text{cm}^{-1}$ , **L1-L4** only).

## 3.0 Transition Metal Complexes

### 3.1 General Complexation Synthesis and Characterisation

#### 3.1.1 General Synthetic Methods

The aim of the project was to synthesise heterometallic *3d/4f* complexes, utilising a mixture of different *3d* and *4f* metal salts (Table 3.1). The metal salts that were utilised were chosen according to their potential magnetic properties, and affinities for H<sub>2</sub>Sao based ligands. As the project proceeded, however, it became clear that the major crystalline products (essential for magnetic characterisation) were all *3d* based, albeit with the incorporation of the *4f* associated counterions.

**Table 3.1:** The metal salts utilised in this research.

<b>3d Metal Salts</b>	<b>4f Metal Salts</b>
CoCl <sub>2</sub> ·6H <sub>2</sub> O	Dy(NO <sub>3</sub> ) <sub>3</sub> ·6H <sub>2</sub> O
Cu(BF <sub>4</sub> ) <sub>2</sub> ·6H <sub>2</sub> O	Gd(NO <sub>3</sub> ) <sub>3</sub> ·6H <sub>2</sub> O
Fe(BF <sub>4</sub> ) <sub>2</sub> ·6H <sub>2</sub> O	HoCl <sub>3</sub> ·6H <sub>2</sub> O
Mn(OAc) <sub>3</sub> ·2H <sub>2</sub> O	La(OAc) <sub>3</sub> ·1.5H <sub>2</sub> O
Mn(NO <sub>3</sub> ) <sub>2</sub> ·4H <sub>2</sub> O	TbCl <sub>3</sub> ·6H <sub>2</sub> O
Ni(OAc) <sub>2</sub> ·4H <sub>2</sub> O	Yb(OAc) <sub>3</sub> ·4H <sub>2</sub> O

The basic H<sub>2</sub>Sao unit has been observed to have several different coordination modes, as illustrated in Section 1.3, Figure 1.8. The modes utilise the deprotonated phenol and oximic oxygens as well as the oximic nitrogen. The addition of the alkylamino chains provides additional coordination sites to ultimately result in structures of high nuclearity.

It has been found in previous work with H<sub>2</sub>Sao based structures that the phenolic proton readily deprotonates when in contact with *3d* metal salts, therefore base was solely used for the deprotonation of the oxime.<sup>46</sup> The bases that were used include pyridine,

2,6-lutidine, Et<sub>3</sub>N, and NaOH. The complexation reactions were performed in MeOH with different solvents and ratios used for crystallisation attempts, including MeOH, MeCN, EtOH, DMF, 1:1 and 3:2 MeOH/MeCN.

Complexations were performed either at RT or at reflux (65 °C for MeOH), with all complexations stirred for at least 30 minutes. Confirmation that coordination had occurred was observed by a colour change from yellow, the colour of the ligands. The methods attempted for recrystallisation included vapour diffusion of Et<sub>2</sub>O and slow evaporation of the reaction solution. Attempts of complexation via solvothermal synthesis were made, with crystallisation achieved by cooling of the reaction solution (DMF was used as the solvent).

Hundreds of complexations were attempted, with varying metal combinations, ligand to metal ratios, solvents, bases and recrystallisation techniques. For the complexations/recrystallisations that did not produce X-ray quality crystals and/or precipitate it was difficult to identify the nuclearity or metal ions present in the metallic core, therefore characterisation techniques were solely performed on the complexations for which crystal structures were obtained (results can be found in Chapter 4.0).

For bulk recrystallisation of the complexes that resulted in crystal structures, methods and starting materials were altered to ensure there was no metallic contamination. For example, the structures that had coordinated anions resulting from the 4*f* metal salts were replaced with an ammonium salt of the anion to ensure no 4*f* ions were trapped in the crystal lattices, and the magnetic properties were solely related to the structures produced.

### *3.1.2 IR Characterisation of Complexes C1-C9*

ATR-FTIR spectroscopy is a quick and easy characterisation technique that was initially performed on the metallic complexes, in the range 700 – 4000 cm<sup>-1</sup> to compare the various stretching and bending modes of both the complexes and their corresponding ligand. The peaks corresponding to the coordinated atoms showed a shift in wavelength as expected.

The coordination modes of all the ligands resemble each other, apart from small variations in additional coordination and the ligands utilised. All complexes have coordination through

the phenolic oxygen atom and the oximic nitrogen atom, these coordination modes are shown by the decrease in intensity of the O-H stretch at approximately 3000 – 3300  $\text{cm}^{-1}$  and shift of C=N peak from 1610 – 1630  $\text{cm}^{-1}$  to 1550 – 1570  $\text{cm}^{-1}$ . For the complexes with coordinated carbonyl groups, a shift in the C=O stretch from 1740  $\text{cm}^{-1}$  to 1650 – 1700  $\text{cm}^{-1}$  is seen. The disappearance and appearance of peaks in the region  $>3000 \text{ cm}^{-1}$  can indicate deprotonation/protonation of certain groups. When the oximic oxygen atom is involved in coordination, the peak at 3000 – 3300  $\text{cm}^{-1}$ , corresponding to the O-H stretch disappears. Amine protonation can be confirmed by the appearance of a N-H stretching peak at 3400 – 3500  $\text{cm}^{-1}$ .

## 3.2 Mononuclear Complexes

### 3.2.1 $[Cu(\mathbf{L1})_2(\text{BF}_4)_2]$ (**C1**), $[\text{Ni}(\mathbf{L1-H})_2]$ (**C2**), and $[\text{Mn}(\mathbf{L4a})_2(\text{NO}_3)_2](\text{NO}_3)$ (**C3**)

The syntheses of the mononuclear complexes **C1**, **C2**, and **C3** all followed the same general procedure; the reaction between the ligand and the corresponding metal salt ( $\text{Cu}(\text{BF}_4)_2 \cdot 6\text{H}_2\text{O}$ ,  $\text{Ni}(\text{OAc})_2 \cdot 6\text{H}_2\text{O}$ , and  $\text{Mn}(\text{NO}_3)_2 \cdot 4\text{H}_2\text{O}$  respectively) in both a 2:1 ratio (**C1** and **C2**) and 1:1 ratio (**C3**) resulted in the formation of green solutions. Isolation was achieved by vapour diffusion of  $\text{Et}_2\text{O}$  into the methanolic reaction solutions over a period of three weeks, resulting in the formation of green platelet crystals of the complex **C1**  $[\text{Cu}(\mathbf{L1})_2(\text{BF}_4)_2]$ , green prism shaped crystals of the complex **C2**  $[\text{Ni}(\mathbf{L1-H})_2]$ , and green/brown platelet crystals of the complex **C3**  $[\text{Mn}(\mathbf{L4a})_2(\text{NO}_3)_2](\text{NO}_3)$ . The formulations were established by elemental analysis, IR, and ESI-MS, and confirmed by X-ray crystallography. **C1** and **C2** are triclinic and crystallise in the  $P\bar{1}$  space group, whereas **C3** is monoclinic and crystallises in the  $P2/c$  space group. For all of the structures, the asymmetric unit contains half of the structure, with the remainder generated by inversion symmetry through the central metal ion (Figures 3.1, 3.2, and 3.3).

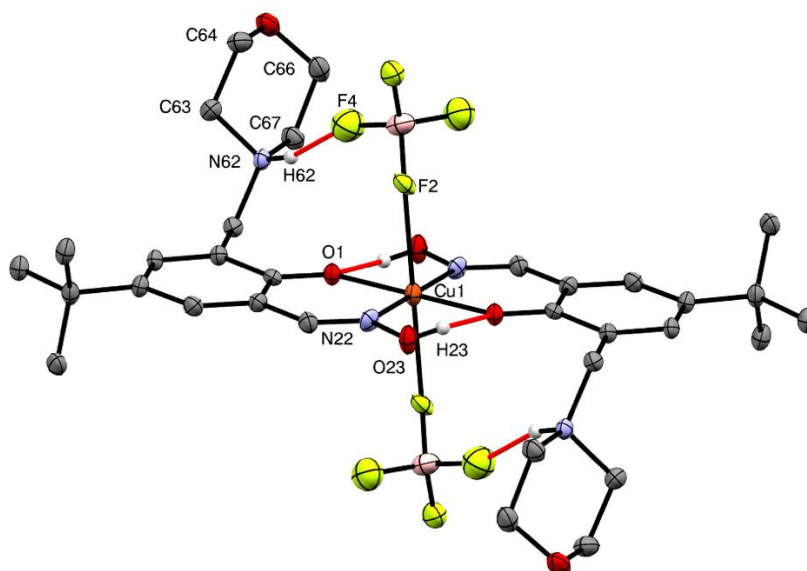


**Figure 3.1:** Crystal structure of the complex  $[\text{Cu}(\mathbf{L1})_2(\text{BF}_4)_2]$ , (**C1**). H atoms, apart from those involved in hydrogen bonding, have been omitted for clarity;  $\text{Cu}^{\text{II}}$  = orange, N = blue, O = red, B = light pink, F = yellow, C = grey, H = white. Hydrogen bonding is represented by red dotted lines. ORTEP view at 30% probability level.

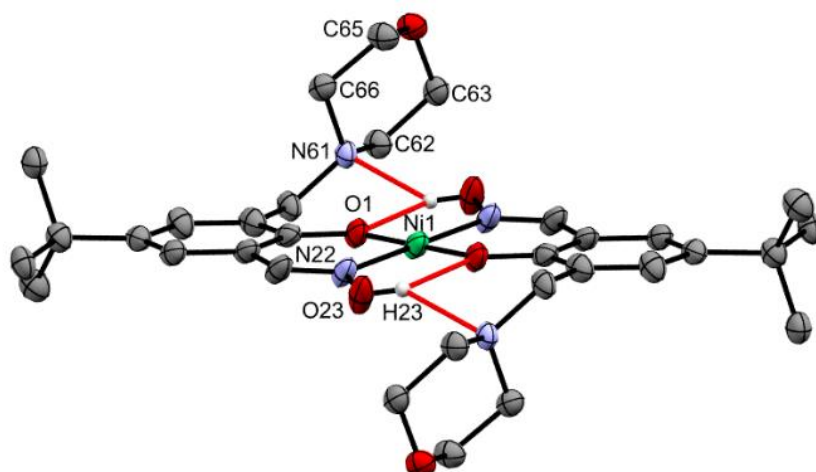


**Figure 3.2:** Crystal structure of the complex  $[\text{Ni}(\text{L1-H})_2]$ , (**C2**). H atoms, apart from those involved in hydrogen bonding, have been omitted for clarity;  $\text{Ni}^{\text{II}}$  = green, N = blue, O = red, C = grey, H = white. Hydrogen bonding is represented by red dotted lines. ORTEP view at 30% probability level.

The complexes all consist of two molecules of either **L1** or **L4a** (**L1** for both **C1** and **C2**, and **L4a** for **C3**), where each of the phenolic oxygen atoms are deprotonated and for **C1** and **C3**, the amino nitrogens are protonated, hence these ligands are in zwitterionic forms. For both **C1** and **C3**, the  $\text{Cu}(\text{II})$  and  $\text{Mn}(\text{III})$  ions lie in distorted octahedral geometries, whereas for **C2**, the  $\text{Ni}(\text{II})$  ion lies in a distorted square planar geometry.

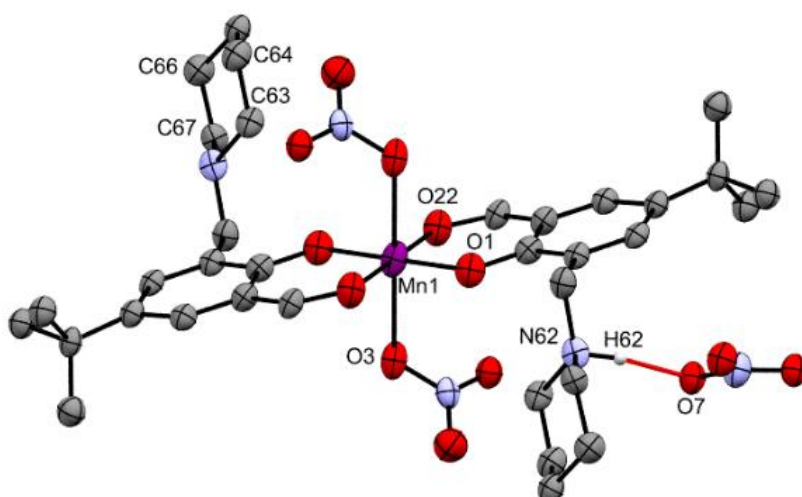


**Figure 3.3:** Crystal structure of the complex  $[\text{Mn}(\text{L4a})_2(\text{NO}_3)_2](\text{NO}_3)$ , (**C3**). H atoms, apart from those involved in hydrogen bonding have been omitted for clarity;  $\text{Mn}^{\text{III}}$  = purple, N = blue, O = red, C = grey, H = white. Hydrogen bonding is represented as red dotted lines. ORTEP view at 30% probability level.

Each metal ion is coordinated equatorially to a phenolic oxygen and either an oximic nitrogen or carbonyl oxygen from each ligand. For **C1** and **C3**, the remainder of the coordination sphere is completed by two anions ( $\text{BF}_4^-$  and  $\text{NO}_3^-$ ) occupying the axial positions. For all three complexes, the ligands coordinate the metal ion in a *trans* arrangement, consistent with similar structures found in the literature (discussed further in Section 1.3). For **C3**, an additional  $\text{NO}_3^-$  anion is found in the crystal lattice to balance the +1 charge of the complex cation; this  $\text{NO}_3^-$  anion forms a hydrogen bond to the protonated amino nitrogen of one ligand ( $\text{N62}\cdots\text{O7}$ , 2.92(3) Å) and a second amino nitrogen of an adjacent structure ( $\text{N62}^1\cdots\text{O5}$ , 2.92(3) Å), producing a chain-like network (Figure 3.4). The SQUEEZE procedure was implemented using the crystallographic software, Olex2, to remove disordered solvent in the crystal lattice.<sup>47</sup> The result of this was the removal of 73.2 electrons ( $e^-$ ), this equates to two MeOH molecules (36  $e^-$ ) and one Et<sub>2</sub>O molecule (42  $e^-$ ). Selected bond lengths and angles of **C1**, **C2** and **C3** can be found in Tables 3.2 and 3.3. For **C3**, a Mn(II) salt was initially used, however it appears oxidation has occurred, resulting in a Mn(III) complex. Despite very weak crystal data, evidence for Mn(III) over Mn(II) was given by charge balance considerations of the complex (with three  $\text{NO}_3^-$  anions per unit formula), and was further confirmed by bond length analysis through comparison with literature examples. The magnetic moment data was performed on the X-ray sample, with the value suggesting a Mn(II) oxidation state. Clearly this discrepancy requires further investigation.

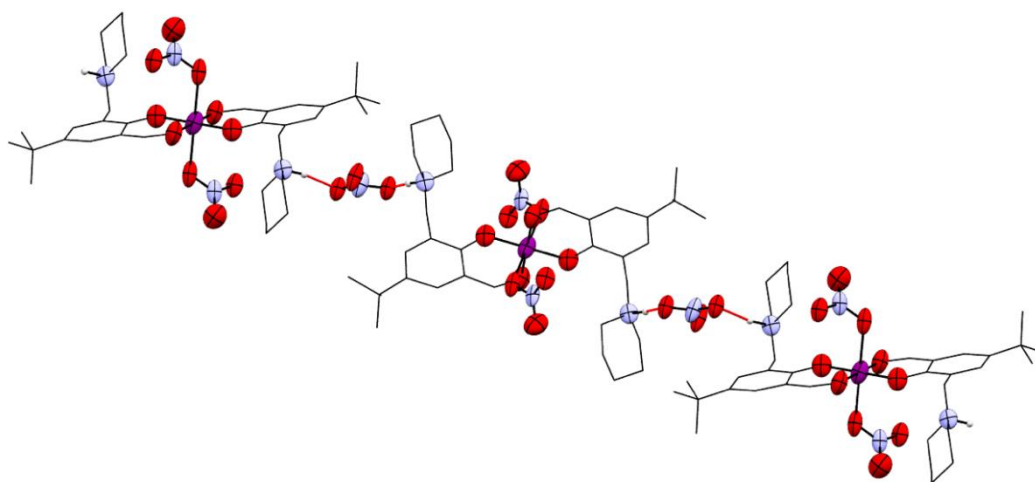


**Figure 3.4:** Crystal structure of **C3**, illustrating the chain-like network produced by hydrogen bonding (red dotted lines).

**Table 3.2:** Selected bond lengths of the complexes **C1**, **C2**, and **C3**.

Bond	Length (Å)	Bond	Length (Å)	Bond	Length (Å)
<b>C1</b>					
Cu1-O1	1.919(15)	Cu1-N22	1.957(13)	Cu1-F2	2.470(19)
<b>C2</b>					
Ni1-O1	1.821(2)	Ni1-N22	1.888(2)		
<b>C3</b>					
Mn1-O1	1.889(4)	Mn1-O22	1.984(10)	Mn1-O3	2.304(3)

**Table 3.3:** Selected bond angles of the complexes **C1**, **C2**, and **C3**.

Atoms	Angle (°)	Atoms	Angle (°)	Atoms	Angle (°)
<b>C1</b>					
O1-Cu1-N22	92.9(6)	O1-Cu1-N22 <sup>1</sup>	87.8(6)	N22-Cu1-N22 <sup>1</sup>	180(0)
O1-Cu1-F2	93.9(5)	O1-Cu1-F2 <sup>1</sup>	86.1(5)	N22-Cu1-F2 <sup>1</sup>	96.7(6)
O1-Cu1-O1 <sup>1</sup>	180(0)	N22-Cu1-F2	83.3(6)	F2-Cu1-F2 <sup>1</sup>	180(0)
<b>C2</b>					
O1-Ni1-N22	94.3(9)	O1-Ni1-N22 <sup>1</sup>	85.7(9)	N22-Ni1-N22 <sup>1</sup>	180(0)
O1-Ni1-O1 <sup>1</sup>	180(0)				
<b>C3</b>					
O1-Mn1-O22	92.0(7)	O1-Mn1-O22 <sup>1</sup>	88.1(7)	O22-Mn1-O22 <sup>1</sup>	180(0)
O1-Mn1-O3	87.1(12)	O1-Mn1-O3 <sup>1</sup>	92.9(12)	O22-Mn1-O3 <sup>1</sup>	91.8(7)
O1-Mn1-O1 <sup>1</sup>	180(0)	O22-Mn1-O3	88.2(7)	O3-Mn1-O3 <sup>1</sup>	180(14)

<sup>1</sup> = 1-x, 1-y, 1-z

The synthesis of **C3** did not proceed as expected; it appears that a hydrolysis reaction occurred during the complexation of **C3**, as the ligand, **L4** was the starting material, however, the X-ray crystal structure clearly shows that the coordinated ligand is actually the aldehyde precursor, **L4a**. IR confirmed the presence of a C=O stretch at 1671 cm<sup>-1</sup> indicating coordination of the aldehyde by the C=O stretch shifting from 1738 cm<sup>-1</sup> as found in the spectrum of **L4a**. An alternative X-ray structural model, where **L4a** was replaced with **L4** was also investigated, however, a suitable peak corresponding to the oximic oxygen could not be located using the difference map, indicating that **L4a** was indeed the correct coordinating species in **C3**.



The complexation reaction was also repeated under identical conditions, but using **L4a** instead of **L4**. Upon addition of the metal to the ligand (both in MeOH), no colour change was observed, instead the yellow colour of the ligand persisted, indicating no immediate coordination to the metal ion. Crystals were not able to be produced from this reaction, so it appears that for the formation of **C3**, the presence of **L4** is a prerequisite. Repeating the complexation with **L4** produced the desired colour change of yellow to dark green, indicating coordination. The complexation reaction and recrystallisation utilising **L4**, was found to only be successful in the presence of NH<sub>4</sub>OAc, indicating that the presence of NH<sub>4</sub>OAc is required to either aid in recrystallisation or mediate the hydrolysis reaction.

For complexes **C1** and **C2**, moderate intramolecular hydrogen bonding is present within the complexes between the oximic OH groups and phenolic oxygen atoms of the opposite molecule of **L1**.<sup>48</sup> For the complex, **C1**, there is additional moderate hydrogen bonding found between the protonated amino nitrogens and a fluoride atom of each coordinated BF<sub>4</sub><sup>-</sup> anion, further stabilising the structure (Table 3.4). For all three complexes, the metallic core lies within the one plane; for **C1** and **C2**, the aromatic rings of each ligand also lie within this same plane, with the morpholine rings and *tert*-butyl groups sticking out of the plane (Figures 3.5 and 3.6). For **C3**, the aromatic rings of each ligand sit in the same plane, however this plane is not parallel with the metallic core. The non-planarity of the structure is due to the crystal packing; each piperidine ring hydrogen bonds to a NO<sub>3</sub><sup>-</sup> anion found in the lattice, as illustrated by Figure 3.7, the anions are found on opposite sides of the plane causing the aromatic rings to distort away from either side of the metallic core.

**Table 3.4:** Hydrogen bonding distances of the complexes **C1**, **C2**, and **C3**.

Atoms (X...A)	Distance (Å)	Atoms (X...A)	Distance (Å)
<b>C1</b>			
O1...O22	2.61(19)	N62...F4	2.85(17)
<b>C2</b>			
O23...O1	2.55(5)	O23...N62	2.79(2)
<b>C3</b>			
O7...N62	2.94(17)	O5...N62 <sup>1</sup>	2.94(17)

<sup>1</sup> = 1-x, 1-y, 1-z

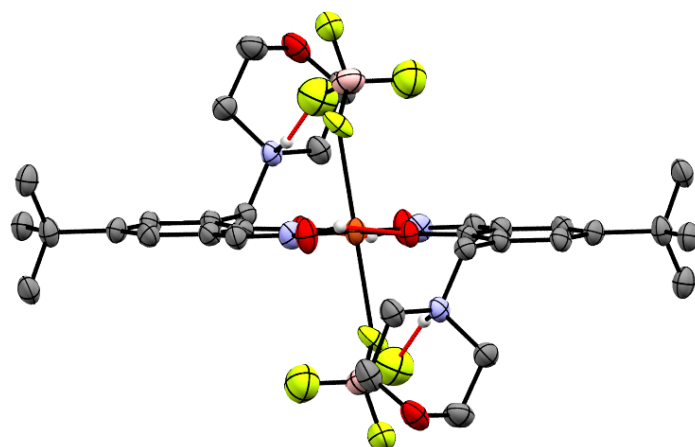


**Figure 3.5:** Crystal structure of **C1**, illustrating the planarity of the structure. ORTEP view at 30% probability level.

The hydrogen bonding within the complexes is responsible for the degree at which the morpholine/piperidine rings are displaced away from the central plane (N22, O1, N22<sup>1</sup>, O1<sup>1</sup>). On analysis of the plane (C63, C64, C66, and C67) angles for **C1** and **C3**, hydrogen bonding between anions, either coordinated or found in the lattice cause the amino rings to be positioned almost perpendicular (89.60° and 89.71° respectively) to the central plane. For **C2**, only intramolecular hydrogen bonding is present between the oximic OH and both the amino nitrogen atoms and phenolic oxygen atoms. This reduces the angle at which these rings are displaced to 69.02°.

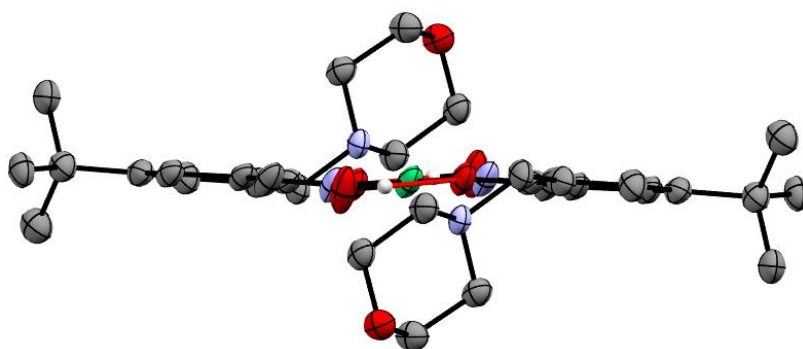


**Figure 3.6:** Crystal structure of **C2**, illustrating the planarity of the structure. ORTEP view at 50% probability level.

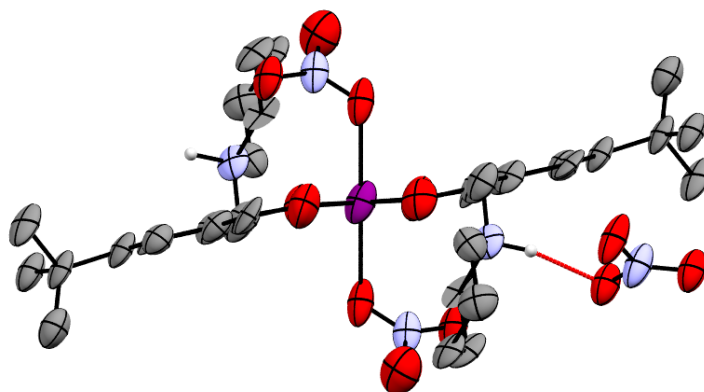


**Figure 3.7:** Crystal structure of **C3**, illustrating the non-planarity of the structure. ORTEP view at 50% probability level.

Conductivity measurements were performed on all three complexes to determine how the complexes behave in solution. The results for the neutral complex **C2** indicated that no anions were present in solution, which agrees with the structural analysis. Measurements on **C1** indicated that the complex was a 1:1 electrolyte in MeOH, i.e. one  $\text{BF}_4^-$  anion dissociates. This result is not unexpected as the  $\text{BF}_4^-$  anions are very weakly coordinated to the Cu(II) ion and could easily dissociate. Measurements performed on **C3** indicated that the complex was a 1:1 electrolyte in MeOH, which was expected, as a  $\text{NO}_3^-$  anion is found in the crystal lattice. Although the structures of **C1** and **C3** are similar that is, they both have two coordinated anions, the conductivity results indicate that the coordination strength differs between the two; as one  $\text{BF}_4^-$  anion dissociates in solution for **C1**, but the  $\text{NO}_3^-$  anions remain coordinated in **C3**.

Magnetic susceptibility ( $\chi_M$ ) measurements were run at RT (296.15 K) on polycrystalline samples of **C1**, **C2**, and **C3** to determine the effective magnetic moment ( $\mu_{eff}$ ) of the complexes, employing the equation:

$$\mu_{eff} = \sqrt{\frac{3\kappa_B}{N_A\beta^2}(\chi_M T)} \quad (\text{eqn. 3})$$

Where,  $\kappa_B$  is the Boltzmann constant,  $N_A$  is Avogadro's number,  $\beta$  is the Bohr magneton,  $\chi_M$  is the molar magnetic susceptibility, and  $T$  is the temperature (K).<sup>49</sup> The magnetic susceptibility results, found in Table 3.5, reveal that the complexes **C1**, and **C3** are paramagnetic in nature, with  $\chi_M$  values of  $1.18 \times 10^{-3}$  and  $1.33 \times 10^{-2}$   $\text{cm}^3 \text{mol}^{-1}$  respectively. **C2** was found to be diamagnetic, with a  $\chi_M$  value of  $-1.98 \times 10^{-4}$   $\text{cm}^3 \text{mol}^{-1}$ . Employing eqn. 3, the  $\chi_M T$  and  $\mu_{eff}$  values found for **C1** ( $0.349 \text{ cm}^3 \text{ K mol}^{-1}$  and  $1.67 \mu_B$  respectively) and **C2** ( $-0.0586 \text{ cm}^3 \text{ K mol}^{-1}$  and  $0.242 \mu_B$  respectively) were found to be as expected; for **C1**, simple H<sub>2</sub>Sao-based Cu(II) complexes have shown to have magnetic moments in the range  $1.79$ - $1.83 \mu_B$ , and for **C2**, the result was as expected for a square planar, d<sup>8</sup> Ni(II) ion.<sup>50</sup> The  $\chi_M T$  and  $\mu_{eff}$  values found for **C3** were found to be  $3.95 \text{ cm}^3 \text{ K mol}^{-1}$  and  $5.59 \mu_B$  respectively. These results were unexpected, as the literature has shown that for one non-interacting, high spin Mn(III) ion, the spin-only  $\chi_M T$  value is  $3.0 \text{ cm}^3 \text{ K mol}^{-1}$ , and the effective magnetic moment is  $4.0 \mu_B$ .<sup>51</sup>

**Table 3.5:** Magnetic susceptibility and magnetic moment results for the complexes **C1**, **C2**, and **C3**.

Complex	$\chi_M$ ( $\text{cm}^3 \text{mol}^{-1}$ )	$\chi_M T$ ( $\text{cm}^3 \text{K mol}^{-1}$ )	$\mu_{eff}$ ( $\mu_B$ )
<b>C1</b>	$1.18 \times 10^{-3}$	0.349	1.67
<b>C2</b>	$-1.98 \times 10^{-4}$	-0.0586	0.242
<b>C3</b>	$1.33 \times 10^{-2}$	3.95	5.59

Over the five year period between 2007 till 2012, several mononuclear H<sub>2</sub>Sal/H<sub>2</sub>Sao based Cu(II), Ni(II), and Mn(II) complexes resembling **C1-C3** were synthesised.<sup>19a, 19b, 20, 52</sup> Forgan *et al.* synthesised two Cu(II) complexes isostructural to **C1**, utilising the ligand, 5-*tert*-Butyl-3-(piperidinylmethyl)-2-hydroxybenzaldehyde oxime (**L4**), and BF<sub>4</sub><sup>-</sup> (Figure 3.8) and NO<sub>3</sub><sup>-</sup> anions (Figure 3.9).<sup>19b, 20</sup> The three complexes were synthesised in the same manner; a RT reaction between the ligand and Cu(II) metal salt (Cu(NO<sub>3</sub>)<sub>2</sub>.3H<sub>2</sub>O or Cu(BF<sub>4</sub>)<sub>2</sub>.6H<sub>2</sub>O). Isolation of the complexes was achieved by vapour diffusion of Et<sub>2</sub>O in the methanolic solution. All three structures have a similar metallic core, with all of the Cu(II) ions lying in an octahedral geometry. All are coordinated equatorially to an oximic nitrogen and phenolic oxygen from each ligand, and weakly coordinated axially to two anions (NO<sub>3</sub> and BF<sub>4</sub>).

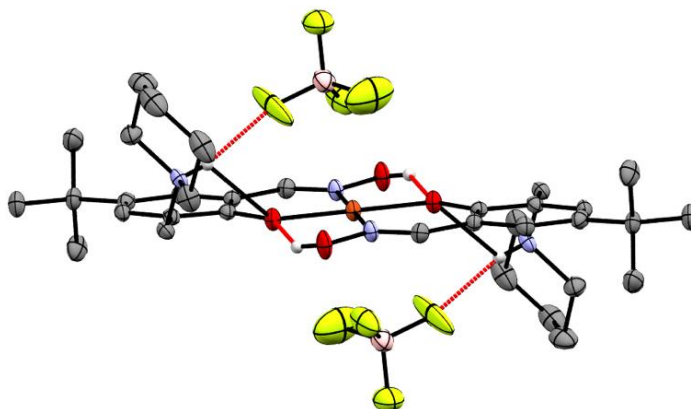


**Figure 3.8:** Crystal structure of the mononuclear Cu<sup>II</sup> complex, with weakly coordinated BF<sub>4</sub><sup>-</sup> anions produced by Forgan *et al.* H atoms, apart from those involved in hydrogen bonding, have been omitted for clarity; Cu<sup>II</sup> = orange, N = blue, O = red, B = light pink, F = yellow, C = grey, H = white. Hydrogen bonding represented as red dotted lines.

A structural difference identified between the different anions, is the angle at which the alkylamino rings are displaced out of the central plane. The angles for the complexes with coordinated BF<sub>4</sub><sup>-</sup> molecules are 89.60° and 88.60°, indicating that the hydrogen bonding between the amino nitrogen and BF<sub>4</sub><sup>-</sup> molecule displaces the rings out of the plane at an angle close to 90°. The complex with the coordinated NO<sub>3</sub><sup>-</sup> anion differs slightly to the others, with the rings at an angle of 80.76° to the central plane. The cause for this difference between the anions, is thought to be due to the strength of the hydrogen bond, with the N...F distance of the BF<sub>4</sub><sup>-</sup> coordinated complex (2.78 Å) shorter and stronger than the O...N distance (2.84 Å) of the NO<sub>3</sub><sup>-</sup> complex by Forgan *et al.* The complex by Forgan *et al.* with weakly coordinated NO<sub>3</sub><sup>-</sup> anions also resembles the complex **C3**, however, the ligand utilised in **C3** has aldehyde functionality rather than oximic functionality. The angle at which the alkylamino rings of **C3** intersect the central plane is 89.71°, greater than found for the NO<sub>3</sub><sup>-</sup> complex of Forgan *et al.* The cause for this is likely due to the fact that no hydrogen bonding occurs between the protonated amino nitrogen and NO<sub>3</sub><sup>-</sup> anion, instead the protonated amine hydrogen bonds to a NO<sub>3</sub><sup>-</sup> anion found in the crystal lattice.

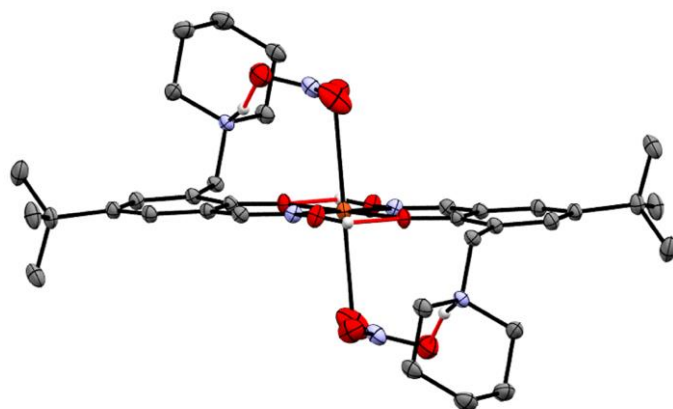


**Figure 3.9:** Crystal structure of the mononuclear Cu<sup>II</sup> complex with coordinated NO<sub>3</sub><sup>-</sup> anions produced by Forgan *et al.* H atoms, apart from those involved in hydrogen bonding have been omitted for clarity; Cu<sup>II</sup> = orange, N = blue, O = red, C = grey, H = white. Hydrogen bonds represented as red dotted lines.

The complex produced by Bates *et al.* is a square planar Ni(II) complex (Figure 3.10) utilising the same ligand as Forgan *et al.*, **L4**.<sup>19a, 19b, 20</sup> This complex is isostructural to the complex, **C2**, with a very similar synthetic procedure and structural properties. The structure of Bates *et al.* was produced by reacting **L4** and Ni(OAc)<sub>2</sub>·4H<sub>2</sub>O in MeOH similarly to the synthesis of **C2**, however, the crystals were grown by slow evaporation from *n*Hex.<sup>19a</sup> The alkylamino rings for both **C2** and the complex produced by Bates *et al.* are displaced out of the central plane at very reduced angles (69.02° and 71.14° respectively) compared to **C1**, **C3**, and the complexes by Forgan *et al.* This again is a result of hydrogen bonding, this time hydrogen bonding between the amino nitrogen and both the phenolic and oximic oxygens.

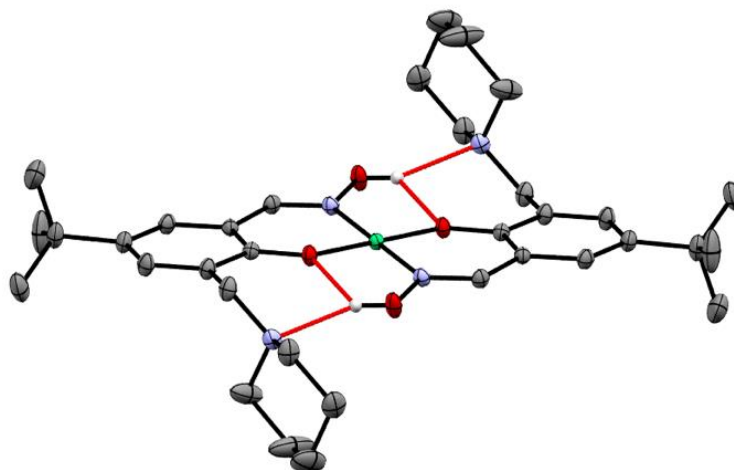


**Figure 3.10:** Crystal structure of the mononuclear Ni<sup>II</sup> complex produced by Bates *et al.* H atoms, apart from those involved in hydrogen bonding, have been omitted for clarity; Ni<sup>II</sup> = green, N = blue, O = red, C = grey, H = white. Hydrogen bonding represented as red dotted lines.

As the structural properties of **C1-C3** resemble those of the mononuclear Cu(II) and Ni(II) complexes by Forgan *et al.* and Bates *et al.*, it could be inferred that the complexes could be utilised as metal cationic and monoanionic extractants in the extractive hydrometallurgy industry. Out of the three complexes (**C1-C3**), **C1** is the most promising for this application, as it was the only complex to coordinate both a metal cation and corresponding anions, whilst retaining the ligand itself (it did not undergo a hydrolytic reaction like **C3**).

A HSal based Mn complex, similar to **C3** was synthesised by Li *et al.* (Figure 3.11).<sup>52</sup> Their complex has an octahedral Mn(II) ion coordinated to phenolic and carbonyl oxygen atoms from each ligand, a DMF molecule, and a H<sub>2</sub>O molecule. A key difference between the two structures is the method used for synthesis. Li *et al.* started with the aldehyde, instead of the aldehyde formed *in situ*. The axial coordinates of the complex by Li *et al.* originate from the complexation solvent (DMF) and H<sub>2</sub>O obtained during synthesis. In a similar fashion to **C3**, the aromatic rings of the ligands do not lie within the same plane as the metallic core. As this structural property has only arisen in the complexes discussed with coordination through an aldehyde, it is implied that the additional hydrogen bonding provided by the oximic OH and phenolic oxygen atom is crucial to the planarity of the structure.

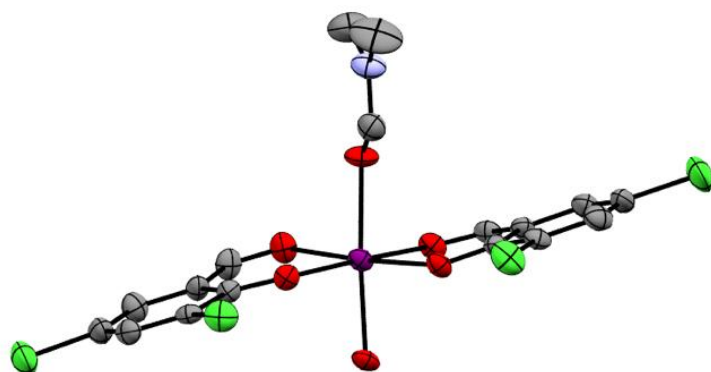


**Figure 3.11:** Crystal structure of the mononuclear Mn<sup>II</sup> structure produced by Li *et al.*, which utilises a HSal based ligand. H atoms omitted for clarity; Mn<sup>II</sup> = purple, N = blue, O = red, Cl = green, C = grey.

In 2008, Hindo *et al.* synthesised a series of H<sub>2</sub>Sai based Cu(II) complexes (Figure 3.12).<sup>53</sup> After initial complexation attempts they discovered that hydrolytic reactions occurred during the complexation, reducing the ligand back to a HSal derivative, similarly to the hydrolytic reaction that occurs in the synthesis of **C3**. Hindo *et al.* deduced that the hydrolysis reaction was the result of free Cu(II) ions in solution, as they had previously shown to catalyse hydrolytic reactions. Previous work in the Plieger group has shown similar results when utilising both oximic ligands and the metal salt, Mn(NO<sub>3</sub>)<sub>2</sub>·4H<sub>2</sub>O, however, reactions utilising Mn<sup>III</sup> salts, such as Mn(OAc)<sub>3</sub>·2H<sub>2</sub>O have not resulted in the hydrolysis of the oximic ligand. In a similar manner to the hydrolytic reaction found for the complex by Hindo *et al.*, it is thought that free Mn<sup>II</sup> ions from the Mn(NO<sub>3</sub>)<sub>2</sub>·4H<sub>2</sub>O salt are responsible for mediating the hydrolysis of **L4** to **L4a**.



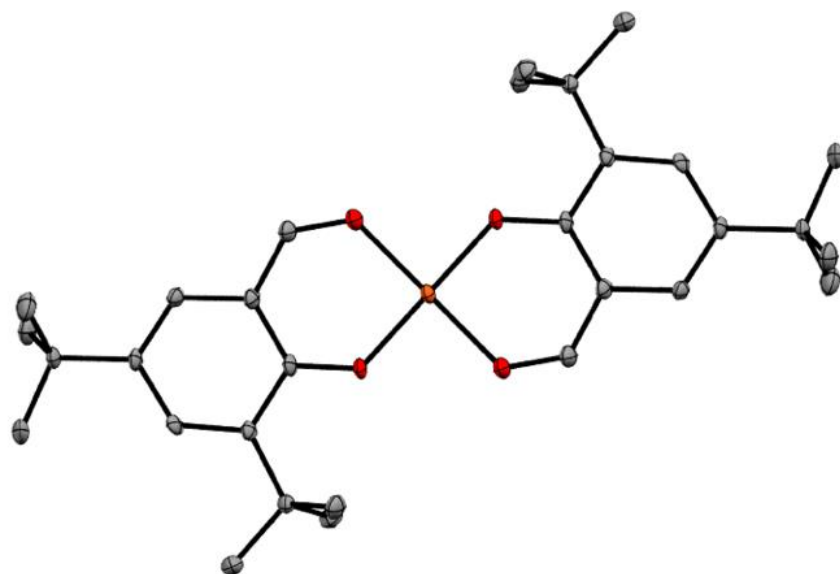


**Figure 3.12:** Crystal structure of the mononuclear Cu<sup>II</sup> structure produced by Hindo *et al.* H atoms omitted for clarity; Cu<sup>II</sup> = orange, O = red, C = grey.

## 3.3 Dinuclear Complexes

### 3.3.1 $[\text{Cu}_2(\text{L3}')_2\text{Cl}_2]$ (**C4**)

The reaction between **L3**,  $\text{Cu}(\text{BF}_4)_2 \cdot 6\text{H}_2\text{O}$  and  $\text{NH}_4\text{Cl}$  in a 1:1:1 ratio resulted in the formation of a green solution. Isolation was achieved by vapour diffusion of  $\text{Et}_2\text{O}$  into the methanolic solution over two weeks, which resulted in the formation of green platelet crystals of the complex **C4**  $[\text{Cu}_2(\text{L3}')_2\text{Cl}_2]$ . The successful complexation was established by IR, and  $^{19}\text{F}$  NMR, and confirmed by X-ray crystallography. **C4** is triclinic and crystallises in the  $P\bar{1}$  space group. The asymmetric unit contains half of the structure, with the remainder generated by inversion through the centroid of Cu1-O4-Cu1-O4 (Figure 3.13, left).

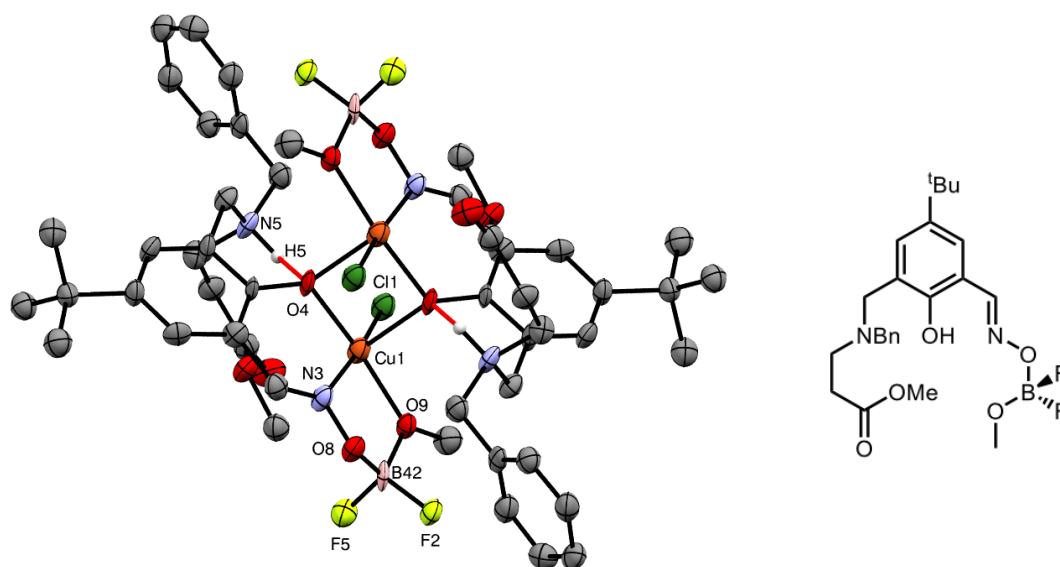


**Figure 3.13:** Crystal structure of the complex  $[\text{Cu}_2(\text{L3}')_2\text{Cl}_2]$ , (**C4**) (left) and the ligand (**L3'**) formed *in situ* (right). H atoms, apart from those involved in hydrogen bonding, have been omitted for clarity;  $\text{Cu}^{\text{II}}$  = orange, N = blue, O = red, B = light pink, F = yellow, Cl = green, C = grey, H = white. Hydrogen bonding is represented by red dotted lines. ORTEP view at 30% probability level.

The complex **C4** consists of two molecules of **L3'**, a derivative of **L3** formed *in situ*. A condensation reaction between **L3**, MeOH, and the  $\text{BF}_4^-$  anion of the metal salt resulted in the formation of **L3'**, where a difluoromethoxy borane functionality is bound to the oximic

oxygen atom (Figure 3.13, right). The Cu(II) ions lie anti-parallel to one another, each with a distorted square pyramidal geometry (see Tables 3.6 and 3.7 for selected bond lengths and angles). Each Cu(II) ion is coordinated to an oximic nitrogen atom, two phenolic oxygen atoms (one from each ligand), a chloride anion and a methoxy oxygen from the difluoromethoxy borane functionality. Strong hydrogen bonding (2.122(8) Å) is present within the complex between the protonated amine and phenolic oxygen of the same molecule of **L3'**.<sup>48</sup>

**Table 3.6:** Selected bond lengths of **C4**.

Bond	Length (Å)	Bond	Length (Å)	Bond	Length (Å)
B42-O8	1.47(14)	Cu1-Cl1	2.25(3)	Cu1-O4 <sup>1</sup>	2.39(8)
B42-O9	1.47(15)	Cu1-O4	1.92(6)	N3-O8	1.38(9)
B42-F5	1.40(16)	Cu1-O9	1.97(6)		
B42-F2	1.41(13)	Cu1-N3	1.95(9)		

<sup>1</sup> = 1-x, -y, 2-z

**Table 3.7:** Selected bond angles of **C4**.

Atoms	Angle (°)	Atoms	Angle (°)	Atoms	Angle (°)
O8-B42-O9	107(11)	Cl1-Cu1-O4	90.0(2)	O4-Cu-O9	171(3)
O8-B42-F5	113(11)	Cl1-Cu1-N3	165(3)	O4-Cu-O4 <sup>1</sup>	84.4(3)
O8-B42-F2	107(10)	Cu1-O4-Cu1	95.6(3)	N3-Cu1-O9	79.8(3)
O9-B42-F2	110(10)	Cl1-Cu1-O9	99.5(2)	N3-Cu1-O4 <sup>1</sup>	93.9(3)
O9-B42-F5	111(11)	Cl1-Cu1-O4 <sup>1</sup>	101(2)	O9-Cu1-O4 <sup>1</sup>	94.6(2)
F5-B42-F2	108(11)	O4-Cu-N3	90.8(3)		

<sup>1</sup> = 1-x, -y, 2-z

To confirm the existence of the difluoromethoxy borane functionality, especially the BF<sub>2</sub><sup>+</sup> group, and to ensure it wasn't a boron dioxide type unit, the B-O bond lengths (oximic (O8) and methoxide (O9)) were compared to that of the B-F bonds. The B-O bond lengths of 1.47(15) Å agree within experimental error to the average B-F bond length of 1.41(15) Å, therefore the existence of a BF<sub>2</sub><sup>+</sup> group cannot be conclusively confirmed by bond length. The X-ray data was resolved with oxygen atoms replacing the fluorine atoms, which

resulted in non-positive definite atoms. This alone suggested that the original formula was indeed right, but was further confirmed by  $^{19}\text{F}$  NMR, with a peak at -150.4 ppm. The chloride ions found in the metallic core originated from the anion of a  $4f$  metal salt used during an initial attempt at a  $3d/4f$  metallic complex. To ensure there was no metal contamination in further complexations, the chloride source was changed to  $\text{NH}_4\text{Cl}$ .

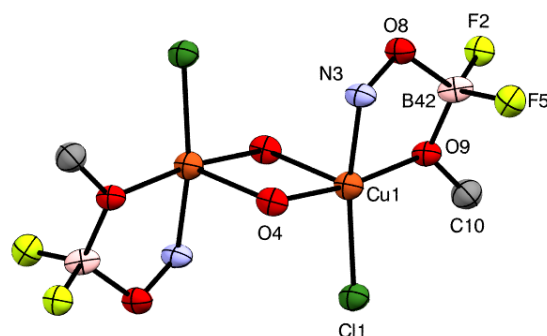


**Figure 3.14:** The metallic core of the complex, **C4**; Cu<sup>II</sup> = orange, N = blue, O = red, B = light pink, F = yellow, Cl = green, C = grey. ORTEP view at 30% probability level.

Conductivity measurements were performed on the complex **C4** to determine how the complex behaves in solution. Measurements indicated that the complex was a 2:1 electrolyte in MeOH, which suggests that each of the chloride anions coordinated to the Cu(II) ions dissociate in the methanolic solution.

Direct current (DC) molar magnetic susceptibility,  $\chi_M$ , measurements were performed on a powdered polycrystalline sample of the complex **C4**. The  $\chi_M$  measurements were measured in an applied magnetic field,  $B$ , of 0.1 T over a temperature ( $T$ ) range of 2 - 300 K. The results are shown in Figure 3.15 in the form of a  $\chi_M T$  vs.  $T$  plot, where  $\chi_M$  is the molar magnetic susceptibility, and  $M$  is the magnetisation of the sample.

$$\hat{H} = \mu_B B \sum_i g_i \hat{S}_i - 2 \sum_{i,j < i} J_{ij} \hat{S}_i \hat{S}_j \quad (\text{eqn. 4})$$

The RT (300 K) measurement of **C4** resulted in a value of  $\chi_M T$  ( $0.91 \text{ cm}^3 \text{ K mol}^{-1}$ ), which agrees with what is expected for a complex containing two non-interacting Cu(II) ions, assuming  $g_{Cu} = 2.2$ . Decreasing the temperature causes the  $\chi_M T$  product to slowly decrease to a value of  $0.82 \text{ cm}^3 \text{ K mol}^{-1}$ , before rapidly decreasing to a value of  $0.71 \text{ cm}^3 \text{ K mol}^{-1}$  at  $T = 2 \text{ K}$ . Behaviour like this is suggestive of extremely weak antiferromagnetic exchange between the two Cu(II) ions.<sup>54</sup>

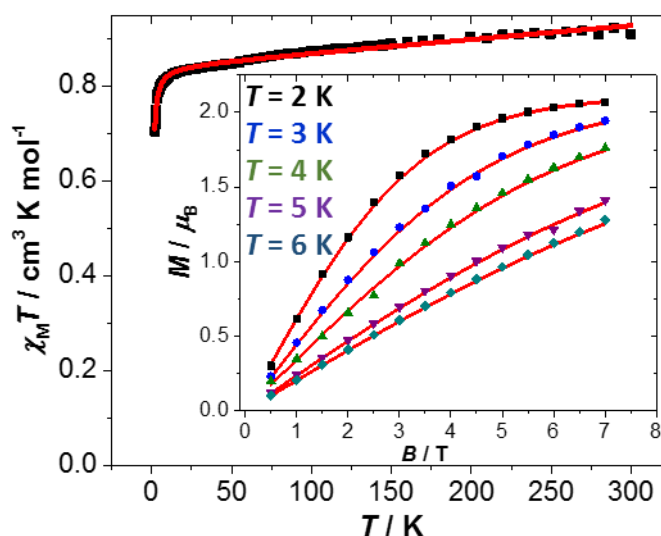


**Figure 3.15:** Plot of  $\chi_M T$  vs.  $T$  for complex **C4** in the  $T = 300\text{-}2 \text{ K}$  temperature range measured in an applied field of  $B = 0.1 \text{ T}$ . The inset shows the VTVB data for **C4** in the  $T = 2\text{-}6 \text{ K}$  and  $B = 0\text{-}7 \text{ T}$  temperature and field ranges. The solid red lines are a fit of the experimental data to spin-Hamiltonian (**eqn. 4**).

Low temperature variable-temperature and variable-field (VTVB) magnetisation measurements were run to obtain a better definition of the low temperature magnetic properties of **C4**. These measurements were performed in a temperature range of  $T = 2\text{-}6 \text{ K}$  and a magnetic field range of  $B = 0\text{-}7 \text{ T}$ , these results can be found in the insert of Figure 3.15. By employing the spin-Hamiltonian (**eqn. 4**), a simultaneous fit of the molar magnetic susceptibility and magnetisation data for **C4** gave best fit parameters of  $J = -0.38 \text{ cm}^{-1}$  and  $g = 2.12$ . This small value of  $J$  is to be expected as the Cu-O-Cu angle for this phenoxo-bridged Cu(II) dimer is  $95.6(3)^\circ$ , very close to the  $90^\circ$  crossover mark for ferro- and antiferromagnetic exchange.<sup>5,54</sup>

Complexes containing dioximate  $\text{BF}_2^+$  bridged ligands have been known since 1962 when the first example was produced by Schrauzer.<sup>55</sup> In 2000, Prushan *et al.* produced Cu(II)/Ni(II) complexes utilising the ligand 4,10-Dithia-7-oxatridecane-2,12-dione dioxime (Figure 3.16, bottom).<sup>34b</sup> The complexation reactions for these complexes formed  $\text{BF}_2^+$  bridged macrocyclic ligands *in situ* in a similar manner as seen by Schrauzer, however, Prushan *et al.* utilised the hydrolysis of  $\text{BF}_4^-$  anions instead of boron trifluoride etherates. A Cu(II) complex was synthesised by adding a methanolic solution of  $\text{Cu}(\text{BF}_4)_2$  to the ligand, also in MeOH. The green solution was further stirred to obtain a purple precipitate, which was recrystallised from hot *n*Hex to yield the Cu(II)  $\text{BF}_2^+$  bridged macrocyclic complex (the structure resembles that of the Ni(II) structure in Figure 3.16, top). A Ni(II)  $\text{BF}_2^+$  bridged complex was also produced by Prushan *et al.*, however, this complex differed from the Cu(II) complex in that it was produced via a stepwise method rather than a one-pot synthesis.<sup>34b</sup> The mononuclear Ni(II) complex, in Figure 3.16, was synthesised initially following the same general procedure used for the previously mentioned Cu(II) complex, however, in order to cap the dioximic ligand and produce a  $\text{BF}_2^+$  bridged macrocyclic complex, the mononuclear Ni(II) complex required treatment with boron trifluoride diethyl etherate.

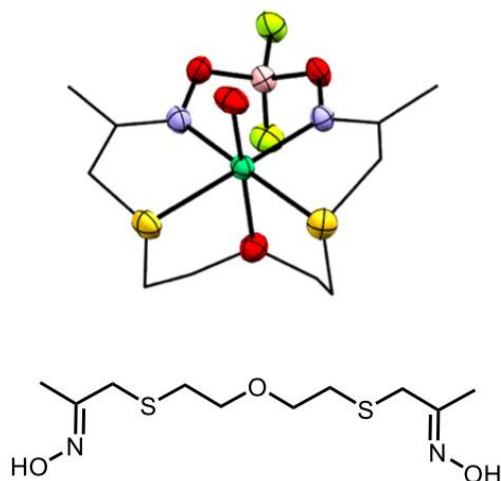


**Figure 3.16:** Crystal structure of the mononuclear  $\text{Ni}^{\text{II}} \text{BF}_2^+$  bridged macrocycle produced by Prushan *et al.* (top), and the ligand utilised (bottom). H atoms omitted for clarity;  $\text{Ni}^{\text{II}}$  = green, N = blue, O = red, S = dark yellow, B = light pink, F = light yellow.

In 2005, Powell and coworkers produced a dinuclear Fe(III) complex with a many structural similarities (Figure 3.17, left) to that of the metallic core found in **C4**.<sup>56</sup> The ligand utilised was a H<sub>2</sub>Sai derivative, 2-[[[3-hydroxypropyl)imino]methyl]-6-methoxyphenol (Figure 3.17, right). Each Fe(III) ion has a square pyramidal geometry and is coordinated to an imine nitrogen atom, a phenolic oxygen atom, a chloride anion, and two deprotonated propanol groups (one from each ligand), with each one bridging the adjacent Fe centre. The magnetic properties of the complex were investigated, and it was found that the two Fe(III) ions had weak antiferromagnetic interactions, as effective coupling pathways were not present within the dinuclear complex, a result which resembled that found for **C4** (further explained above).<sup>56</sup>

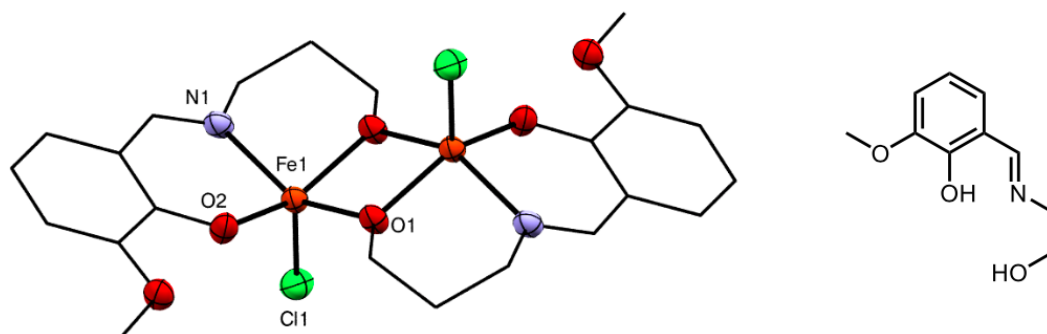


**Figure 3.17:** Crystal structure of the dinuclear Fe<sup>III</sup> complex produced by Powell and co-workers (left) and the ligand utilised (right). H atoms omitted for clarity; Fe<sup>III</sup> = orange, N = blue, O = red, Cl = green.

## 3.4 Trinuclear Complexes

### 3.4.1 $[Fe_3O(L4-H)_3(OAc)_3]^-$ (C5) and $[Mn_3O(L4-H)_2(L4-2H)(OAc)_3]$ (C6)

The trinuclear complexes **C5** and **C6**, were synthesised following the same general procedure as **C1-C3**; the reaction between **L4**, the corresponding metal salt ( $Fe(BF_4)_2 \cdot 6H_2O$  or  $Mn(OAc)_3 \cdot 2H_2O$ ), pyridine, and  $NH_4OAc$  (**C5** only), in a 1:1:1 ratio resulted in the formation of maroon and dark green solutions respectively. Isolation was achieved by vapour diffusion of  $Et_2O$  into the methanolic reaction solutions over three weeks, resulting in the formation of maroon platelet crystals of the complex **C5**  $[Fe_3O(L4-H)_3(OAc)_3]^-$ , and green platelet crystals of the complex **C6**  $[Mn_3O(L4-H)_2(L4-2H)(OAc)_3]$ . The successful complexations were established by IR and confirmed by X-ray crystallography. **C5** and **C6** are both triclinic and crystallise in the  $P\bar{1}$  space group. For both **C5** and **C6**, the complete structure is found within the asymmetric unit (Figures 3.18 and 3.19). In both complexes the X-ray data is weak; regardless of this the connectivity is clearly established.

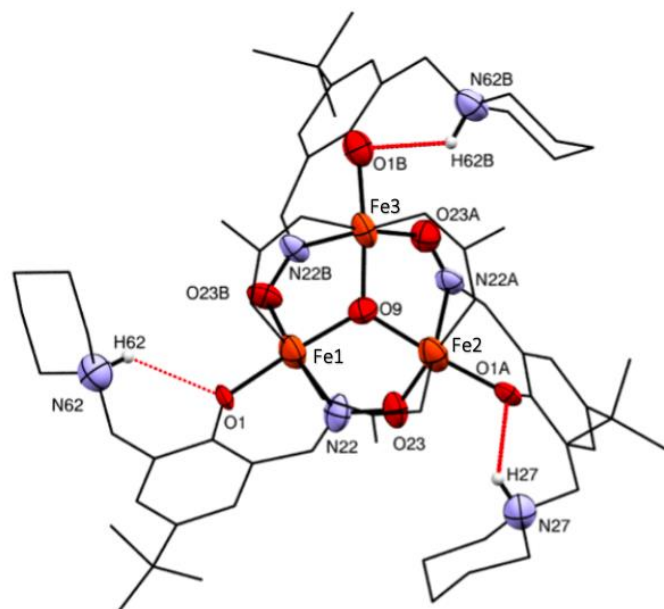


**Figure 3.18:** Crystal structure of the complex  $[Fe_3O(L4-H)_3(OAc)_3]^-$ , (**C5**). H atoms, apart from those involved in hydrogen bonding, have been omitted for clarity;  $Fe^{III}$  = orange, N = blue, O = red, H = white. Hydrogen bonding represented as red dotted lines. ORTEP view at 30% probability level.



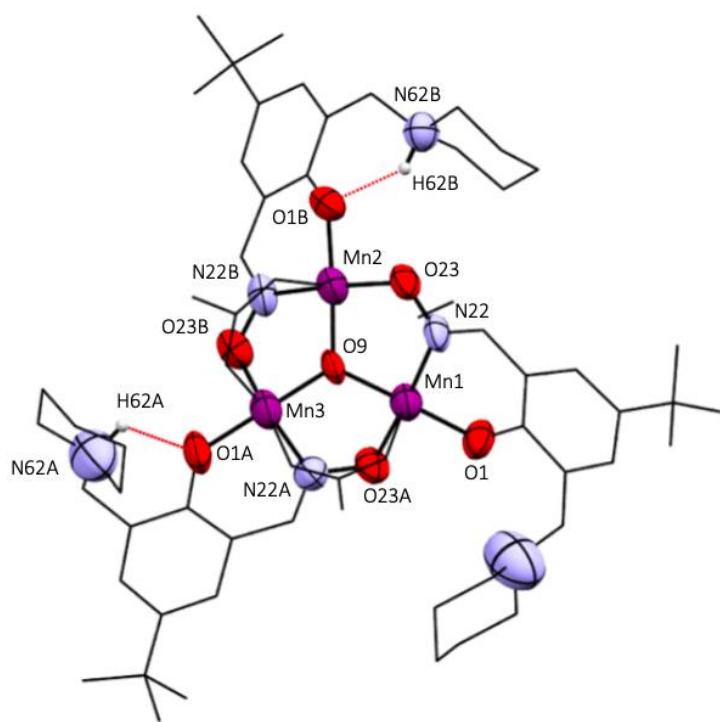


**Figure 3.19:** Crystal structure of the complex  $[\text{Mn}_3\text{O}(\text{L4-H})_2(\text{L4-2H})(\text{OAc})_3]$ , (**C6**). H atoms, apart from those involved in hydrogen bonding have been omitted for clarity;  $\text{Mn}^{\text{III}}$  = purple, N = blue, O = red, H = white. Hydrogen bonding represented as red dotted lines. ORTEP view at 30% probability level.

Both complexes consist of three molecules of **L4**, with both the phenolic and oximic oxygen atoms deprotonated. For **C5**, all of the amino nitrogen atoms are protonated, whereas for **C6**, two amino nitrogen atoms are protonated (based on charge balance analysis). The metal ions each have a distorted octahedral geometry (see Tables 3.8 and 3.9 for selected bond lengths and angles) with an overall triangular topology. Each metal ion is coordinated to an oximic nitrogen and a phenolic oxygen from one ligand, an oximic oxygen from an adjacent ligand, two  $\mu_2$ -bridging  $\text{OAc}^-$  groups and a central  $\mu_3$ -bridging oxygen atom, thought to have originated from the hydrolysis of residual  $\text{H}_2\text{O}$  molecules (Figures 3.18 and 3.19).<sup>22</sup> For **C5**, a  $\text{Fe}(\text{II})$  salt was initially used, however it appears oxidation has occurred, resulting in a  $\text{Fe}(\text{III})$  complex. Evidence was initially given by charge balance of the complex, and was further confirmed by Mössbauer analysis, and magnetic characterisation.

Both **C5** and **C6** have had the SQUEEZE procedure implemented using Olex2.<sup>47</sup> For **C5**, a total of 293 e<sup>-</sup> were removed, corresponding to one BF<sub>4</sub><sup>-</sup> anion (41 e<sup>-</sup>), one pyridine molecule (42 e<sup>-</sup>), and five Et<sub>2</sub>O molecules (210 e<sup>-</sup>). According to Mössbauer analysis (further explained below), the oxidation state of the Fe ions is +3, thus one anion is required to balance the overall charge of the complex. Geometric analysis of the difference map suggests the presence of one BF<sub>4</sub><sup>-</sup> anion. For **C6**, a total of 229 e<sup>-</sup> were removed, corresponding to five Et<sub>2</sub>O molecules (210 e<sup>-</sup>) and one MeOH molecule (18 e<sup>-</sup>). As no anions are found in the lattice, the overall charge of the complex is balanced by the protonation of two of the three amino nitrogens. Despite the weak crystal data, the protonation of only two nitrogen atoms was indicated by the charge balance of the complex, and further confirmed by bond length analysis through comparison with the literature. The interatomic hydrogen bond lengths (2.71(13) Å and 2.74(2) Å (N62B...O1B and N62A...O1A respectively) and the third distance of N62...O1 (2.91(13) Å) however are inconclusive due to the poor data.

**Table 3.8:** Selected bond lengths of the complexes, **C5** and **C6**.

Bond	Length (Å)	Bond	Length (Å)	Bond	Length (Å)
<b>C5</b>					
Fe1-O9	1.86(2)	Fe2-O9	1.93(1)	Fe3-O9	1.84(2)
Fe1-O6	1.89(1)	Fe2-N22A	2.25(3)	Fe3-O23A	1.95(2)
Fe1-O23B	1.96(2)	Fe2-O23	1.99(2)	Fe3-O1B	1.87(2)
Fe1-N22	2.16(2)	Fe2-O1A	2.00(1)	Fe3-N22B	2.11(2)
Fe1-O71	2.07(2)	Fe2-O72	1.99(2)	Fe3-O72A	2.07(1)
Fe1-O71A	2.03(1)	Fe2-O72B	2.06(1)	Fe3-O71B	2.04(1)
<b>C6</b>					
Mn1-O9	1.87(8)	Mn2-O9	1.87(5)	Mn3-O1B	1.88(9)
Mn1-O1	1.86(1)	Mn2-O6	1.94(9)	Mn3-O9	1.82(7)
Mn1-O23B	1.91(7)	Mn2-O1A	1.90(6)	Mn3-O72A	2.02(1)
Mn1-O71	2.18(9)	Mn2-O71A	2.17(1)	Mn3-O23A	2.10(7)
Mn1-O72B	2.39(1)	Mn2-O72	2.32(1)	Mn3-N22B	2.06(1)
Mn1-N37	2.00(8)	Mn2-N22A	2.03(1)	Mn3-O71B	2.30(9)

**Table 3.9:** Selected bond angles of the complexes, C5 and C6.

Atoms	Angle (°)	Atoms	Angle (°)	Atoms	Angle (°)
<b>C5</b>					
O9-Fe1-O6	173(7)	O9-Fe2-N22A	79.7(8)	O9-Fe3-O23A	93.6(8)
O9-Fe1-O23B	91.4(8)	O9-Fe2-O23	93.6(7)	O9-Fe3-O1B	171(8)
O9-Fe1-N22	87.1(8)	O9-Fe2-O1A	174(7)	O9-Fe3-N22B	82.5(8)
O9-Fe1-O71	84.4(6)	O9-Fe2-O72	95.8(7)	O9-Fe3-O72A	92.1(7)
O9-Fe1-O71A	94.0(7)	O9-Fe2-O72B	87.3(7)	O9-Fe3-O71B	95.5(7)
O6-Fe1-O23B	87.1(7)	N22A-Fe2-O23	101(8)	O23A-Fe3-O1B	85.3(8)
O6-Fe1-N22	86.4(8)	N22A-Fe2-O1A	94.2(7)	O23A-Fe3-N22B	93.2(8)
O6-Fe1-O71	97.8(6)	N22A-Fe2-O72	167(7)	O23A-Fe3-O72A	174(7)
O6-Fe1-O71A	92.7(6)	N22A-Fe2-O72B	81.8(7)	O23A-Fe3-O71B	92.3(7)
O23B-Fe1-N22	95.4(9)	O23-Fe2-O1A	86.3(7)	O1B-Fe3-N22B	88.4(8)
O23B-Fe1-O71	172(7)	O23-Fe2-O72	90.8(7)	O1B-Fe3-O72A	89.2(7)
O23B-Fe1-O71A	89.2(7)	O23-Fe2-O72B	177(7)	O1B-Fe3-O71B	93.6(7)
N22-Fe1-O71	90.9(8)	O1A-Fe2-O72	90.3(6)	N22B-Fe3-O72A	87.8(7)
N22-Fe1-O71A	175(8)	O1A-Fe2-O72B	93.1(6)	N22B-Fe3-O71B	174(7)
O71-Fe1-O71A	84.6(6)	O72-Fe2-O72B	86.3(6)	O72A-Fe3-O71B	86.9(6)
Fe1-O9-Fe3	120(9)	Fe1-O9-Fe2	116(9)	Fe3-O9-Fe2	119(9)
<b>C6</b>					
O9-Mn1-O1	172(3)	O9-Mn2-O6	88.5(3)	O1B-Mn3-O9	173(4)
O9-Mn1-O23B	90.2(3)	O9-Mn2-O1A	177(3)	O1B-Mn3-O72A	90.6(4)
O9-Mn1-O71	99.5(3)	O9-Mn2-O71A	89.2(3)	O1B-Mn3-O23A	88.9(4)
O9-Mn1-O72B	88.8(3)	O9-Mn2-O72	97.3(3)	O1B-Mn3-N22B	87.5(4)
O9-Mn1-N37	86.0(3)	O9-Mn2-N22A	88.9(4)	O1B-Mn3-O71B	91.7(4)
O1-Mn1-O23B	93.0(4)	O6-Mn2-O1A	93.4(3)	O9-Mn3-O72A	95.0(3)
O1-Mn1-O71	88.5(4)	O6-Mn2-O71A	96.3(3)	O9-Mn3-O23A	86.8(3)
O1-Mn1-O72B	83.7(4)	O6-Mn2-O72	88.2(3)	O9-Mn3-N22B	88.6(4)
O1-Mn1-N37	90.9(4)	O6-Mn2-N22A	173(4)	O9-Mn3-O71B	93.5(3)
O23B-Mn1-O71	88.7(4)	O1A-Mn2-O71A	88.0(3)	O72A-Mn3-O23A	90.4(3)
O23B-Mn1-O72B	85.8(3)	O1A-Mn2-O72	85.4(3)	O72A-Mn3-N22B	162(4)
O23B-Mn1-N37	176(4)	O1A-Mn2-N22A	89.6(4)	O72A-Mn3-O71B	80.0(4)
O71-Mn1-O72B	170(4)	O71A-Mn2-O72	172(3)	O23A-Mn3-N22B	108(4)
O71-Mn1-N37	90.4(4)	O71A-Mn2-N22A	90.6(4)	O23A-Mn3-O71B	170(4)
O72B-Mn1-N37	95.7(4)	O72-Mn2-N22A	85.3(4)	N22B-Mn3-O71B	81.8(4)
Mn1-O9-Mn2	115(4)	Mn1-O9-Mn3	122(4)	Mn2-O9-Mn3	121(4)

For **C5**, moderate hydrogen bonding is found between all of the phenolic oxygen atoms and amino nitrogen atoms from the same ligand.<sup>48</sup> The hydrogen bonding present in **C6**, differs from **C5** in that only two protonated amino nitrogen atoms hydrogen bond with a phenolic oxygen of the same ligand. These hydrogen bond distances can be found in Table 3.10.

**Table 3.10:** Hydrogen bond distances found in the complexes, **C5** and **C6**.

Atoms (X...A)	Distance (Å)	Atoms (X...A)	Distance (Å)	Atoms (X...A)	Distance (Å)
<b>C5</b>					
N62...O1	3.06(14)	N62A...O1A	2.66(3)	N62B...O1B	2.92(14)
<b>C6</b>					
N62A...O1A	2.74(2)	N62B...O1B	2.71(13)		

The conductivity measurements performed on the complexes **C5** and **C6**, reveal that for both complexes, anions are found in solution. For **C5**, the measurement revealed that for every one complex in solution, three anions are found in solution. One of the anions are believed to be  $\text{BF}_4^-$ , as suggested by the difference map of residual electron density prior to the application of the SQUEEZE protocol as implemented in Olex2, with the other two likely to be dissociated  $\text{OAc}^-$  anions.<sup>47</sup> The measurement of **C6** revealed that for every complex in solution one anion is present, indicating that when in solution one  $\text{OAc}^-$  anion dissociates.

The Mössbauer characterisation undertaken on the complex **C5**, was performed at RT (294 K), liquid nitrogen temperature (LNT) (77 K) and low T (6.3 K) to determine the oxidation state/s, structural, and magnetic properties of the Fe centres. The resulting parameters can be found in Table 3.11.

**Table 3.11:**  $^{57}\text{Fe}$  Mössbauer parameters of the complex, **C5**.  $\delta$ , isomer shift;  $\Delta E_Q$ , quadrupole splitting;  $\Gamma_L$ , line width of the left peak;  $\Gamma_R$ , line width of the right peak.

T (K)	$\delta$ (mm/s)	$\Delta E_Q$ (mm/s)	$\Gamma_L$ (mm/s)	$\Gamma_R$ (mm/s)
294	0.41	0.90	0.60	0.64
77	0.51	1.02	0.55	0.57
6.3	0.54	1.01	0.80	0.80

The Mössbauer spectra of the complex **C5** (Figure 3.20) at RT, LNT, and low T all show a single quadrupole doublet, with isomer shifts of 0.41, 0.51, and 0.54 mm/s respectively. These results are indicative of a single type of high spin Fe(III) ions contained within an octahedral coordination geometry.<sup>57</sup> The small temperature dependence in the quadrupole splittings (0.90 mm/s vs. 1.01 and 1.02 mm/s) and slight asymmetry in the doublet widths (increasing with T) indicates that the environments in which the Fe(III) ions are found may have small structural discrepancies.<sup>57a</sup> X-ray crystallography data supports this finding, as the entire complex is found within the asymmetric unit, suggesting minor structural discrepancies between the Fe coordination environments. Magnetic measurements, discussed further below, found three different exchange couplings between the Fe(III) centres, resulting from three distinct Fe-N-O-Fe torsion angles, further confirming the Mössbauer results. The slight broadening of the doublet in the low T spectrum indicates intermediate relaxation of the Fe(III) centres.<sup>57c</sup>

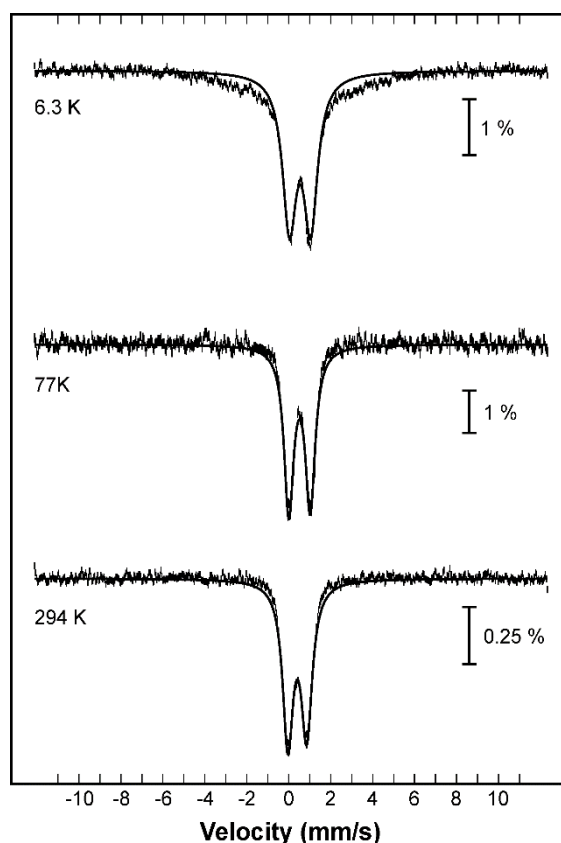


**Figure 3.20:** <sup>57</sup>Fe Mössbauer spectrum of the complex, **C5**, at RT (294 K), LNT (77 K), and low T (6.3 K).

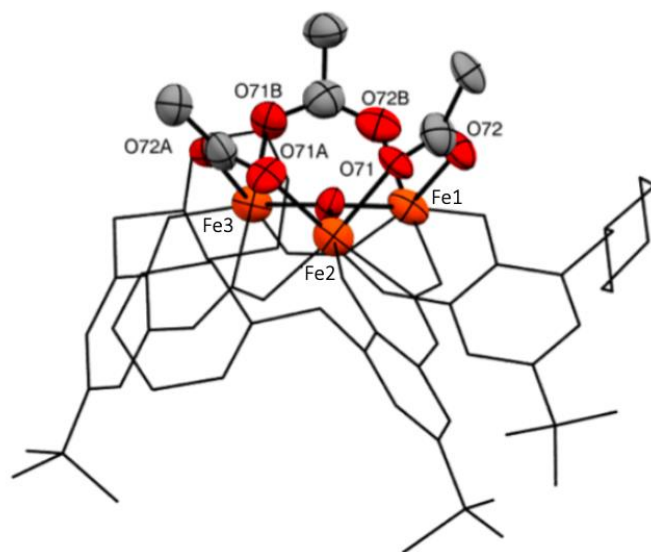


**Figure 3.21:** Crystal structure of **C5**, illustrating the *fac* coordination of the OAc<sup>-</sup> groups. H atoms omitted for clarity; Fe<sup>III</sup> = orange, O = red, C = grey. ORTEP view at 30% probability level.

A key structural difference between **C5** and **C6** is the geometry of the  $\mu_2$ -bridging OAc<sup>-</sup> groups (Figures 3.21 and 3.22). For **C5**, the three  $\mu_2$ -bridging OAc<sup>-</sup> groups all adopt a *fac* geometry, whereas for **C6**, two adopt *mer* geometry and the third a *fac* geometry. It is not fully understood the cause for the different OAc<sup>-</sup> geometries between the two complexes, however, one difference between them that could have a role in the different geometries is the source of the OAc<sup>-</sup> anions. For **C6**, the OAc<sup>-</sup> anions originate from the metal salt, therefore they are already coordinated to the metal ion. For **C5**, the OAc<sup>-</sup> is added in the form of NH<sub>4</sub>OAc; this late addition could have a role in the final geometry. The different OAc<sup>-</sup> geometries however do not cause different distortions in the placement of the central  $\mu_3$ -bridging oxygen atom, as for both **C5** and **C6**, it is found to sit just above the plane containing the three metal ions.

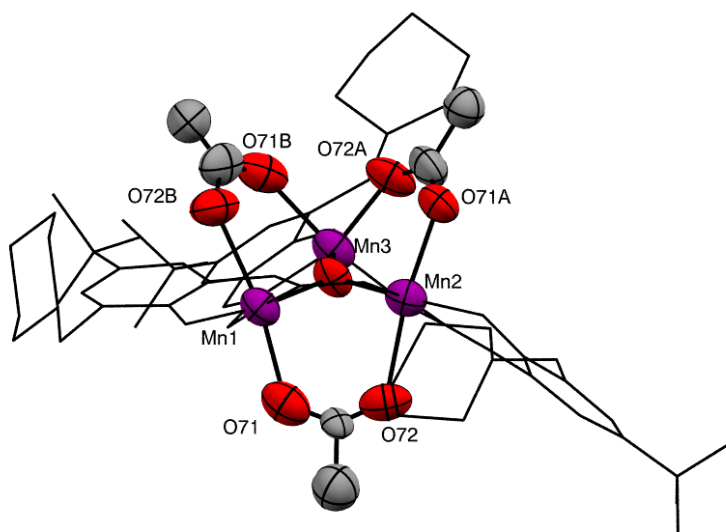


**Figure 3.22:** Crystal structure of **C6** illustrating the *mer-mer-fac* coordination of the OAc<sup>-</sup> anions. H atoms omitted for clarity; Mn<sup>III</sup> = purple, O = red, C = grey. ORTEP view at 30% probability level.

A search of the CCDC (v. 1.20) revealed that 274 Mn complexes with one or more triangular structures exist; 74 of them being discrete complexes with a single triangular topology. The search also revealed that the complex **C6** is the first known H<sub>2</sub>Sao based Mn(III) triangle with three  $\mu_2$ -bridging groups with *mer-mer-fac* coordination geometry. All of the complexes found either had anions or solvent molecules with *fac* coordination geometry or an anion coordinated to all metal ions. The search was extended to pyridyl oximes, and the same result was found; no complexes with single triangular topologies contained a *mer-mer-fac* coordination geometry.

For both complexes, the bond angles between the central oxygen atom and the metal ions do not differ significantly, with them all agreeing within experimental error (Table 3.9). This was surprising as it was proposed that the different coordination geometries between the complexes would cause significant distortions on the M-O-M bond angles (M = Fe or Mn). The bond angles of the oximato bridges however, were found to differ within the complexes and between the two different metals. For the Fe(III) triangle, it was found that three different torsion angles were present within the complex. The most likely cause for this, is that all OAc anions are found on the same face of the triangle, and cause distortions as a result of steric hinderance. For the Mn(III) triangle, only two different oximato torsion

angles are present. For the two oximato bridges found on the same face of the triangle, they are found to have the same distortion, whereas the oximato bridge on the opposite face is found to have a different, smaller distortion. The result of these torsion angles on the complexes magnetic properties is discussed below.

Direct current (DC) molar magnetic susceptibility,  $\chi_M$ , measurements were performed on powdered polycrystalline samples of the complexes **C5** and **C6**. The  $\chi_M$  measurements were measured in an applied magnetic field,  $B$ , of 0.1 T over a temperature ( $T$ ) range of 1.8 - 290 K. The results are shown in Figure 3.23 in the form of a  $\chi_M T$  vs.  $T$  plot, where  $\chi_M$  is the molar magnetic susceptibility, and  $M$  is the magnetisation of the sample. At 290 K the  $\chi_M T$  values of **C5** and **C6** are 4.2 and 6.1  $\text{cm}^3 \text{K mol}^{-1}$ , respectively, lower than that expected for three uncoupled Fe(III) and Mn(III) ions (13.125 and 9.0  $\text{cm}^3 \text{K mol}^{-1}$  with  $g = 2.00$ ). The value of  $\chi_M T$  rapidly decreases with decreasing temperature in both cases reaching values of 0.9 and 1.5  $\text{cm}^3 \text{K mol}^{-1}$  at  $T = 1.8$  K, respectively. Both data sets are indicative of antiferromagnetic exchange interactions between the constituent metal centres.

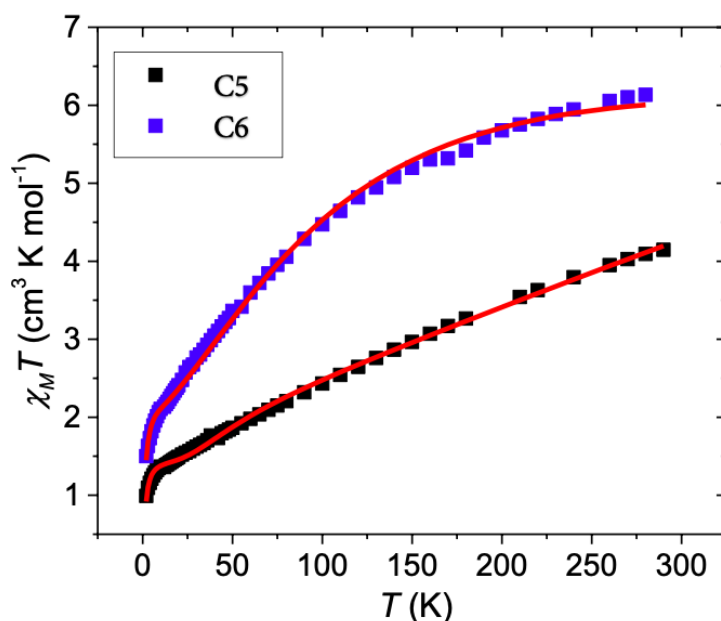


**Figure 3.23:** Plot of the  $\chi_M T$  product versus  $T$  for **C5** and **C6** in the  $T = 290 - 1.8$  K temperature range, in an applied field,  $B = 0.1$  T. The solid red lines are a fit of the experimental data.



A fit of the susceptibility data employing spin-Hamiltonian (**eqn. 4**) and the exchange coupling models depicted in Figure 3.24 afforded the best fit parameters:  $J_1 = -31.6 \text{ cm}^{-1}$ ,  $J_2 = -46.1 \text{ cm}^{-1}$ ,  $J_3 = -25.5 \text{ cm}^{-1}$  for **C5** and  $J_1 = -3.6 \text{ cm}^{-1}$ ,  $J_2 = -9.6 \text{ cm}^{-1}$  for **C6**. In each case  $g$  was fixed to  $g = 2.00$ . In the frame of this (simple) isotropic model, **C5** possesses an  $S = 1/2$  ground state, with **C6** an  $S = 1$  ground state (Figure 3.25), both with numerous low-lying excited states. Note that in the case of **C6**,  $D_{(\text{Mn})}$  may well be of the same order of magnitude as  $J$ , and thus EPR spectroscopy will be required to obtain the axial/rhombic zero-field splitting parameters. The exchange interactions obtained above are in agreement with those previously reported for similar  $[\text{M}^{\text{III}}\text{O}(\text{oxime})(\text{O}_2\text{CR})_3]$  species with  $\text{M} = \text{Mn}(\text{III})$  and  $\text{Fe}(\text{III})$ .<sup>23b, 58</sup>

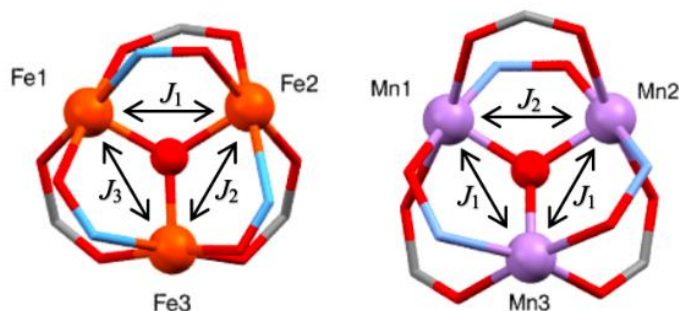


**Figure 3.24:** Exchange interaction models for **C5** (left) and **C6** (right) illustrating the exchange interactions found within the complexes.

In each case the triangles are scalene ( $P\bar{1}$ ), with the whole cluster in the asymmetric unit. However, since each edge of the triangle is bridged by one oxide, one carboxylate and one oxime, the fitting procedure began by employing the simplest (single  $J$ ) model before moving to models containing two or three  $J$ -values. For **C5** there are three different Fe-O-N-Fe torsion angles of  $\sim 0^\circ$  ( $J_2$ ),  $2^\circ$  ( $J_1$ ) and  $4^\circ$  ( $J_3$ ). For **C6** the best fit was obtained from a  $2J$  model where  $J_1 = \text{Mn1-Mn3}$ ,  $\text{Mn2-Mn3}$  containing Mn-O-O-Mn torsion angles of  $\sim 7^\circ$  with the carboxylates on the same side on the  $\text{Mn}_3$  plane, and  $J_2 = \text{Mn1-Mn2}$  with a Mn-O-N-Mn torsion angle of  $\sim 0.3^\circ$  and the carboxylate on the opposite side of the  $\text{Mn}_3$  plane.

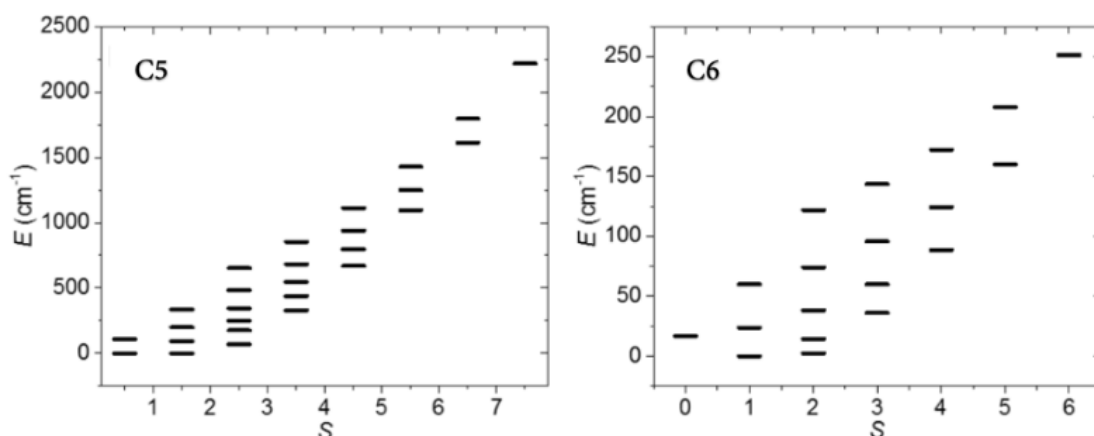


**Figure 3.25:** Plot of lowest lying spin states ( $S$ ) versus energy ( $E$ ) as obtained from the isotropic fit of the susceptibility data for **C5** (left) and **C6** (right).

In 2005, Stamatatos *et al.* produced the first known triangular SMM; a Mn(III) complex with a triangular topology (Figure 3.26) resembling both **C5** and **C6**.<sup>59</sup> Mn triangular structures had been produced in the past, however, these had all exhibited antiferromagnetic interactions.<sup>60</sup> Stamatatos *et al.* discovered that ferromagnetic interactions could be induced through distorting the oximato Mn-N-O-Mn bridges. The ligand utilised was a pyridyl oxime derivative, 1-(2-pyridyl)-ethanone oxime, the structure resembles **C5** as it has three  $\mu_2$ -OAc anions bridging the Mn(III) ions with *fac* coordination. The ferromagnetic interactions present in the Mn(III) complex were induced by the distortion of the central oxygen atom out of the plane which contains the three Mn(III) ions. This distortion differs to what was found for **C5** and **C6**, with the oximato bridge distortion dictating the exchange pathways, as discussed above.

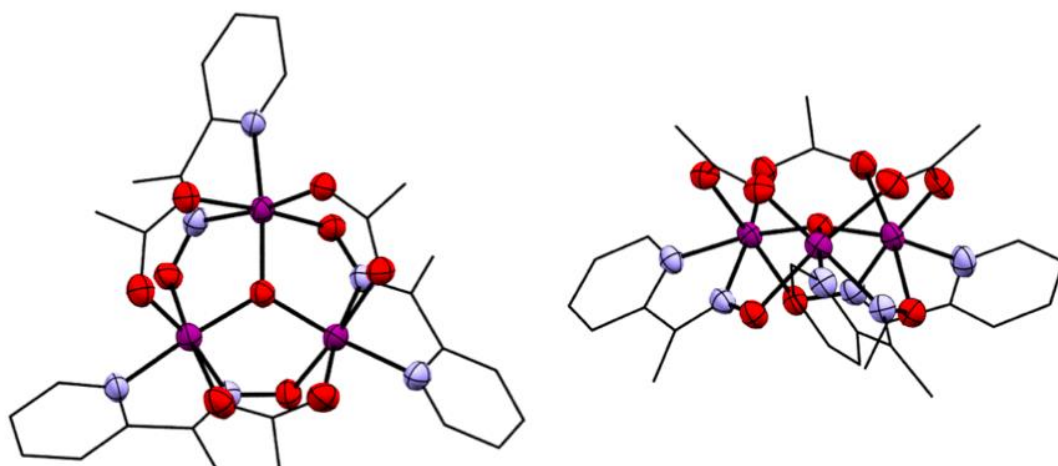


**Figure 3.26:** Crystal structures of the first known triangular SMM produced Stamatatos *et al.*, looking down at the metallic core (left) and illustrating the *fac* coordination geometry of the OAc<sup>-</sup> anions (right). Mn<sup>III</sup> = purple, N = blue, O = red.

There are many variations of the initial Mn triangular SMM produced by Stamatatos *et al.*, found in literature.<sup>59a, 61</sup> All of the complexes, whether pyridyl based oximes or H<sub>2</sub>Sao derivatives, have either coordinating anions with either all *mer* or all *fac* geometries. A couple of the H<sub>2</sub>Sao based complexes, are the structures produced by Yang *et al.* (Figure 3.27, left), Stoumpos *et al.*, and Kozoni *et al.*<sup>61</sup> These structures all have a single triangular topology, and are capped by anions and solvents such as: MeOH, chloride, and OH<sup>-</sup> anions.

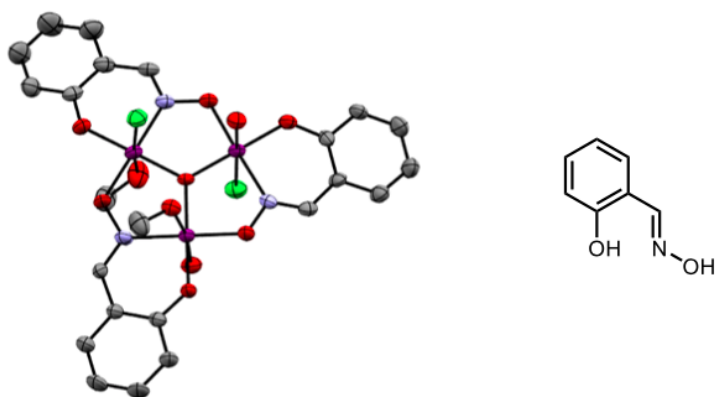


**Figure 3.27:** Crystal structure of the Mn<sup>III</sup> triangular SMM produced by Yang *et al.* (left) and the corresponding ligand used (right). H atoms are omitted for clarity; Mn<sup>III</sup> = purple, N = blue, O = red, Cl = green, C = grey.

These complexes mentioned above, have been characterised and employed for use as magnetic materials, and building blocks for supramolecular structures. The Mn(III) structure synthesised by Yang *et al.* (Figure 3.27) was characterised by SQUID magnetometry to determine the complexes magnetic properties.<sup>61c</sup> The characterisation revealed that the Mn(III) ions are antiferromagnetically coupled, with two exchange pathways present within the complex, resembling **C6**. Yang *et al.* found that the cause for the antiferromagnetic exchange was that the torsion angle of the Mn-N-O-Mn bridges was less than 30°, and the central  $\mu_3$ -oxo bridge was found to be planar with the three Mn(III) ions. This finding is relevant for both the complexes **C5** and **C6**, as the torsion angles of the Mn-N-O-Mn bridges for these complexes range from approximately 0 - 7° (discussed further in the magnetic section above).

## 3.5 Tetranuclear Complexes

### 3.5.1 $[Fe_4(L3)_2(OMe)_6(OH)_6]$ (**C7**)

The reaction between **L3** and  $Fe(BF_4)_2 \cdot 6H_2O$  in a 1:2 ratio resulted in the formation of a maroon solution. Isolation was achieved by vapour diffusion of  $Et_2O$  into the 1:1 MeOH/MeCN solution over five weeks, which resulted in the formation of red platelet crystals of the complex **C7**  $[Fe_4(L3)_2(OMe)_6(OH)_6]$ . The successful complexation was established by IR and confirmed by Mössbauer spectroscopy and X-ray crystallography. **C7** is monoclinic and crystallises in the  $P 2_1/n$  space group. The asymmetric unit contains one-half of the structure with the remaining generated by inversion through the centroid of Fe1-071-Fe1-071 (Figure 3.29). The X-ray data for **C7** is weak, however, like **C5** and **C6**, the connectivity is clearly established.

The complete characterisation of **C7** was not achieved within the time frame of this research due to unforeseen reproducibility issues. A theory for this reproducibility issue is that the 4f metal salt acts as a templating agent, and although it doesn't end up in the final structure, it could be a crucial component for a successful complexation.

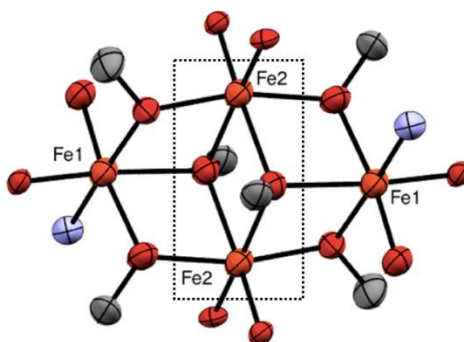


**Figure 3.28:** The metallic core of the complex, **C7**, illustrating the defective dicubane topology. The dotted box indicates the 'body'  $Fe^{III}$  ions (Fe2).  $Fe^{III}$  = orange, N = blue, O = red, C = grey. ORTEP view at 30% probability level.

The complex **C7** consists of two molecules of **L3**, with the phenolic oxygen atom deprotonated and the amino nitrogen atom protonated. Each Fe(III) ion has a distorted octahedral geometry (see Tables 3.12 and 3.13 for selected bond lengths and angles) with an overall defective dicubane or ‘butterfly’ topology. The metal coordination environment differs between the body and wingtip metal ions (Figure 3.28), with the wingtip Fe(III) ions coordinated to an oximic nitrogen, a phenolic oxygen, a terminal OH<sup>-</sup> anion, a bridging  $\mu_3$ -OMe, and two bridging  $\mu_2$ -OMe molecules. The body Fe(III) ions are coordinated by two bridging  $\mu_3$ -OMe groups, two bridging  $\mu_2$ -OMe groups and two terminal OH<sup>-</sup> anions (the hydroxide molecules are thought to have originated from the hydrolysis of water molecules, originating from the hydrated metal salts). The ligands are arranged in a *trans* conformation to each other (Figure 3.29). Within the complex there is hydrogen bonding of moderate strength, found between the body OH<sup>-</sup> anions and the oximic OH (O11...O23, 2.59(2) Å), and amino nitrogen atom (N62...O12, 2.59(2) Å) of opposite ligands (Figure 3.29). The OMe<sup>-</sup> and OH<sup>-</sup> anions found in the metallic core, are assumed to have originated from the hydrolysis of solvent and residual water molecules during the heated complexation reaction.<sup>22</sup>

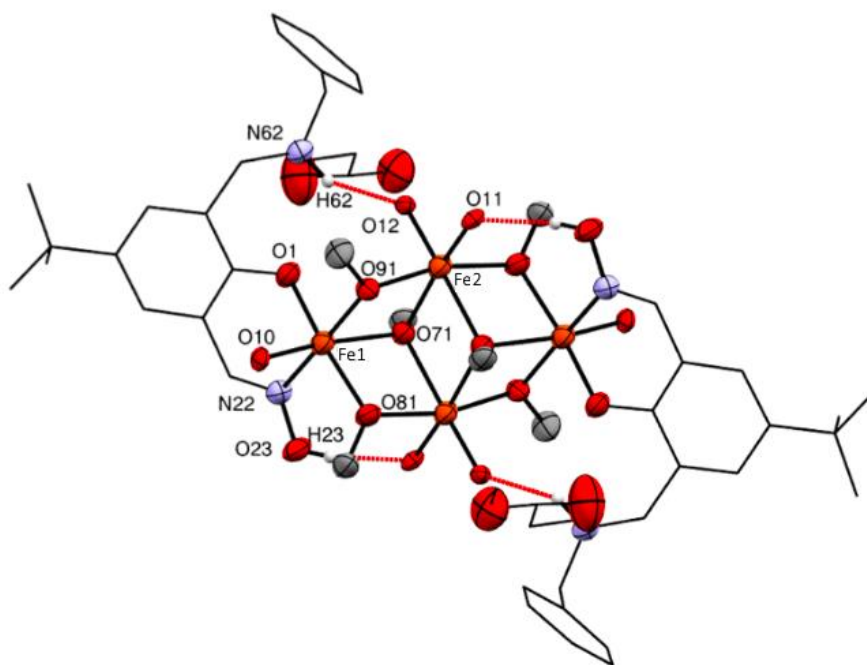


**Figure 3.29:** Crystal structure of the complex  $[\text{Fe}_4(\text{L3})_2(\text{OMe})_6(\text{OH})_6]$ , (**C7**). H atoms, apart from those involved in hydrogen bonding, have been omitted for clarity; Fe<sup>III</sup> = orange, N = blue, O = red, C = grey, H = white. ORTEP view at 30% probability level.

The SQUEEZE procedure was implemented using the crystallographic software, Olex2, to remove disorder in the crystal lattice.<sup>47</sup> The result of this was the removal of 106 e<sup>-</sup>, which equates to five MeCN molecules (110 e<sup>-</sup>).

**Table 3.12:** Selected bond lengths of the complex, C7.

Bond	Length (Å)	Bond	Length (Å)	Bond	Length (Å)
Fe1-O10	1.82(4)	Fe1-N22	2.21(6)	Fe2-O71	2.13(4)
Fe1-O71	2.11(4)	Fe1-O91	1.98(5)	Fe2-O81	1.98(4)
Fe1-O81	1.98(4)	Fe2-O12	1.87(4)	Fe2-O91	1.98(4)
Fe1-O1	1.95(5)	Fe2-O11	1.89(4)	Fe2-O71	2.11(4)

<sup>1</sup> = 1-x, 1-y, 1-z

**Table 3.13:** Selected bond angles of the complex, C7.

Atoms	Angle (°)	Atoms	Angle (°)	Atoms	Angle (°)
O10-Fe1-O71	171(17)	O1-Fe1-N22	82.4(2)	O71-Fe2-O81	76.8(18)
O10-Fe1-O81	94.3(18)	O1-Fe1-O91	90.6(19)	O71-Fe2-O91	89.5(17)
O10-Fe1-O1	97.8(18)	N22-Fe1-O91	169(19)	O71-Fe2-O71	76.1(18)
O10-Fe1-N22	90.7(19)	O12-Fe2-O11	97.8(18)	O81-Fe2-O91	166(18)
O10-Fe1-O91	98.3(17)	O12-Fe2-O71	166(17)	O81-Fe2-O71	94.2(17)
O71-Fe1-O81	77.2(18)	O12-Fe2-O81	95.5(18)	O91-Fe2-O71	78.9(17)
O71-Fe1-O1	91.1(18)	O12-Fe2-O91	97.1(17)	Fe2-O71-Fe1	98.0(18)
O71-Fe1-N22	93.2(19)	O12-Fe2-O71 <sup>1</sup>	92.6(17)	Fe2-O71-Fe2 <sup>1</sup>	103.9(18)
O71-Fe1-O91	78.9(17)	O11-Fe2-O71	94.3(17)	Fe1-O71-Fe2 <sup>1</sup>	96.0(18)
O81-Fe1-O1	166(19)	O11-Fe2-O81	89.2(17)	Fe2-O81-Fe1	108(2)
O81-Fe1-N22	90.9(2)	O11-Fe2-O91	95.3(17)	Fe2 <sup>1</sup> -O91-Fe1	105(2)
O81-Fe1-O91	94.2(18)	O11-Fe2-O71 <sup>1</sup>	167(18)		

<sup>1</sup> = 1-x, 1-y, 1-z

Although a Fe(II) salt was initially used, Mössbauer results (further discussed below) reveal that the oxidation state of all of the Fe ions is +3, indicating that oxidation of the metal salt has occurred during synthesis. This gives rise to two possible formulations for the structure of the complex. The first formulation identifies the oxygen atoms coordinated to the body ions as OH<sup>-</sup> anions, the oxygen atoms coordinated to the wingtips as water molecules, and

no protonation of the amino nitrogens. The second formulation identifies the oxygen atoms coordinated to both the body and wingtip ions as OH<sup>-</sup> anions, with the amino nitrogens protonated. Analysis of the residual electron density contained within the difference map in the X-ray structure, resulted in the identification of a peak at a distance from the nitrogen atom suggestive of protonation, providing evidence for formulation two.

The Mössbauer characterisation performed on the complex **C7**, was performed at RT (294 K), LNT (77 K) and low T (6.3 K) to determine the oxidation state/s, structural, and magnetic properties of the Fe centres. The resulting parameters can be found in Table 3.14. For the low T spectrum of **C7**, magnetic hyperfine splitting was observed, therefore, the spectrum was fitted to a hyperfine field distribution.

**Table 3.14:** <sup>57</sup>Fe Mössbauer parameters of the complex, **C7**.  $\delta$ , isomer shift;  $\Delta E_Q$ , quadrupole splitting;  $\Gamma_L$ , line width of the left peak;  $\Gamma_R$ , line width of the right peak.

T (K)	$\delta$ (mm/s)	$\Delta E_Q$ (mm/s)	$\Gamma_L$ (mm/s)	$\Gamma_R$ (mm/s)
294	0.42	0.72	0.47	0.47
77	0.52	0.74	0.49	0.49

The Mössbauer spectra (Figure 3.30) of the complex **C7** at RT and LNT each show a single quadrupole doublet, with corresponding isomer shifts of 0.42 and 0.52 mm/s respectively, indicative of high spin Fe(III) ions contained within octahedral coordination geometries.<sup>57</sup> The presence of a single quadrupole doublet also indicates that the Fe nuclei are all identical within the complex.<sup>57a</sup> The spectrum recorded at low T exhibits magnetic hyperfine splitting, indicating that the Fe(III) centres are fully relaxed to their magnetic ground state. The data was fitted to a hyperfine field distribution, which is suggestive that different Fe environments could be present within the complex. The expected spectra for **C7**, was a pair of quadrupole doublets, as X-ray crystallography revealed two distinct Fe(III) coordination environments: the body Fe(III) ions have O<sub>6</sub> coordination, and the wingtip Fe(III) ions have O<sub>5</sub>N<sub>1</sub> coordination. However, as the magnetic spectrum indicates two possible Fe environments in the complex, it could be that the different environments are unresolvable at LNT and RT.



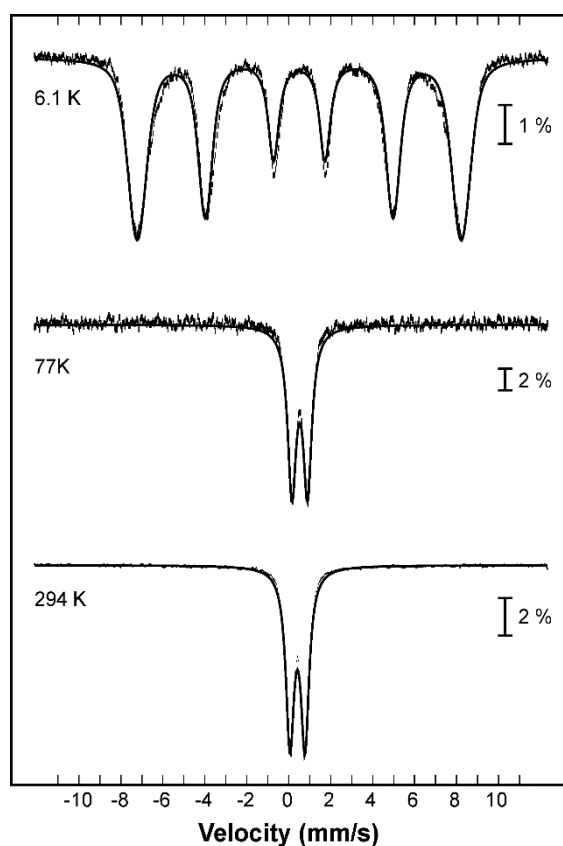
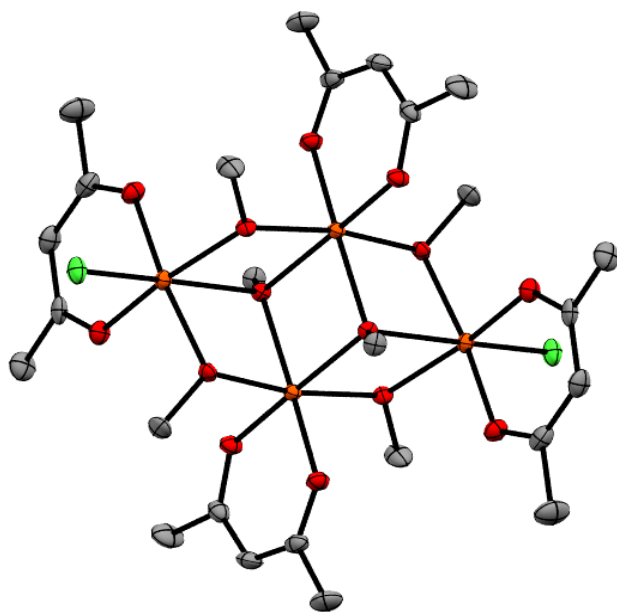


Figure 3.30:  $^{57}\text{Fe}$  Mössbauer spectrum of the complex, **C7**, at RT (294 K), LNT (77 K), and low T (6.3 K).

In 2015, the research group of Gray, synthesised a tetranuclear Fe(III) complex, which had a defective dicubane topology (Figure 3.31).<sup>26</sup> The metallic core of this complex resembles that of the metallic core of **C7**; it has both  $\mu_3^-$ - and  $\mu_2$ -bridging OMe anions. The remaining coordination sites are occupied by acetylacetonate (acac) and chloride anions originating from the Fe(III) metal salt. The complexation differed from that of **C7**, as the reaction was performed at RT, and the source of the OMe<sup>-</sup> anions originated from a methyl silanolate complex (NaOSi(OMe)<sub>2</sub>Me) instead of the solvent, as seen for **C7**. The different coordination geometries of both the body and wingtip Fe(III) ions cause both the bond lengths and bond angles to differ between the two complexes. The simple coordination to acac and chloride anions causes the defective dicubane core to be smaller than the core for **C7**. Neither complex had magnetic measurements performed, therefore the effect of the size difference in relation to magnetic properties could not be compared and/or investigated.



**Figure 3.31:** Crystal structure of the Fe<sup>III</sup> defective dicubane produced by the research group of Gray. H atoms have been omitted for clarity; Fe<sup>III</sup> = orange, O = red, Cl = green, C = grey.

3.5.2  $[Ni_4(L2-H)_2(OAc)_2(OMe)_2Cl_2](Et_2O)_3$  (**C8**) and  $[Ni_4(L3-H)_2(OAc)_2(OMe)_2Cl_2](MeOH)_2$  (**C9**)

The tetranuclear Ni(II) complexes, **C8** and **C9** were synthesised following the same general procedure as **C1-C6**; the reaction between ligand (**L2** and **L3** respectively), Ni(OAc)<sub>2</sub>·6H<sub>2</sub>O, and NH<sub>4</sub>Cl in a 1:2:1 ratio resulted in the formation of green solutions. Isolation was achieved by vapour diffusion of Et<sub>2</sub>O into the methanolic solutions over a period of 8 weeks for **C8** and 3 weeks for **C9**. The result of the recrystallisations was the formation of green prism shaped crystals of **C8**  $[Ni_4(L2-H)_2(OAc)_2(OMe)_2Cl_2](Et_2O)_3$  and **C9**  $[Ni_4(L3-H)_2(OAc)_2(OMe)_2Cl_2](MeOH)_2$ . The successful complexations were established by IR, with confirmation by X-ray crystallography. Both complexes are monoclinic, with **C8** crystallising in the *P* 2<sub>1</sub>/*c* space group and **C9** in the *C* 2/*c* space group. For both complexes, the asymmetric unit contains half of the structure with the remaining generated by inversion through the centroid of Ni1-O3-Ni1-O3 (Figures 3.33 and 3.34).

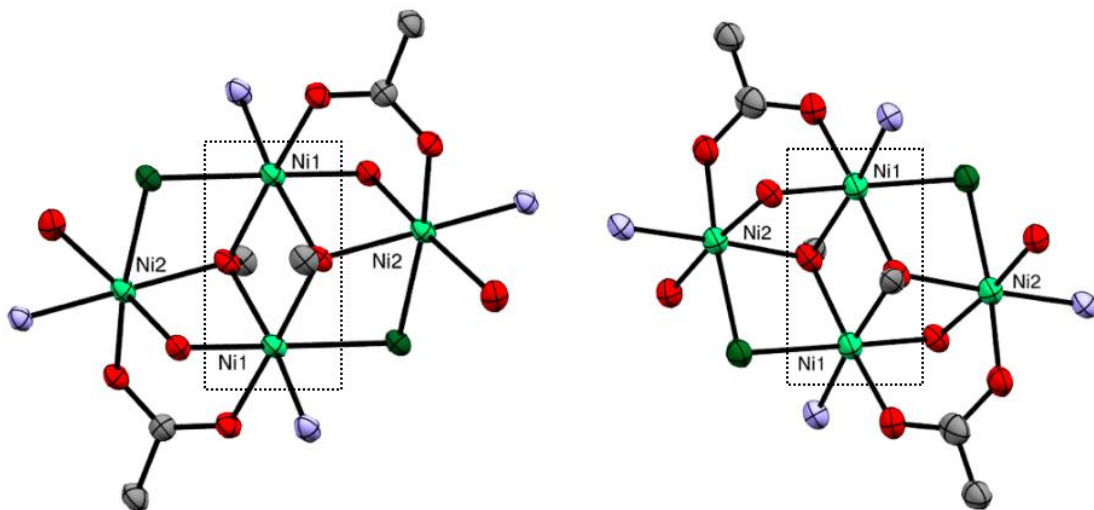


**Figure 3.32:** The metallic cores of the Ni<sup>II</sup> defective dicubane complexes, **C8** (left) and **C9** (right). H atoms omitted for clarity; Ni<sup>II</sup> = light green, N = blue, O = red, Cl = dark green, C = grey. The dotted boxes indicate the Ni<sup>II</sup> 'body' ions (Ni1). ORTEP view at 30% probability level.

The complexes consist of two molecules of **L2-H/L3-H**, with the phenolic oxygen atoms deprotonated. The Ni(II) ions each have a distorted octahedral geometry (see Tables 3.15 and 3.16 for selected bond angles and lengths) with an overall defective dicubane or 'butterfly' topology. The metal coordination differs between the body and wingtip metal ions (Figure 3.32), with the wingtip Ni(II) ions coordinated to a  $\mu_2$ -phenolic oxygen atom, an amino nitrogen atom, a  $\mu_2$ -OAc, a  $\mu_2$ -chloride, a  $\mu_3$ -OMe, and for **C8**, a methoxy oxygen of one of the ether groups and for **C9**, a carbonyl oxygen. The body ions are coordinated to a  $\mu_2$ -phenolic oxygen, oximic nitrogen,  $\mu_2$ -OAc,  $\mu_2$ -chloride, and two  $\mu_3$ -OMe groups. Within the crystal lattices, there are three Et<sub>2</sub>O molecules, with one positionally disordered over two sites, found for **C8**, and two MeOH molecules found for **C9**. For both **C8** and **C9**, two moderate hydrogen bonds are present within the structures, found between the oximic OH groups and  $\mu_2$ -bridging chlorides (O23...Cl1, 2.91(12) Å and 3.01(5) Å respectively).<sup>48</sup> Additional moderate hydrogen bonding (O6...O5, 2.86(1) Å) is present in **C9**, between the lattice MeOH molecule and an oxygen atom of one of the coordinated OAc<sup>-</sup> anions (O5) (Figure 3.34).

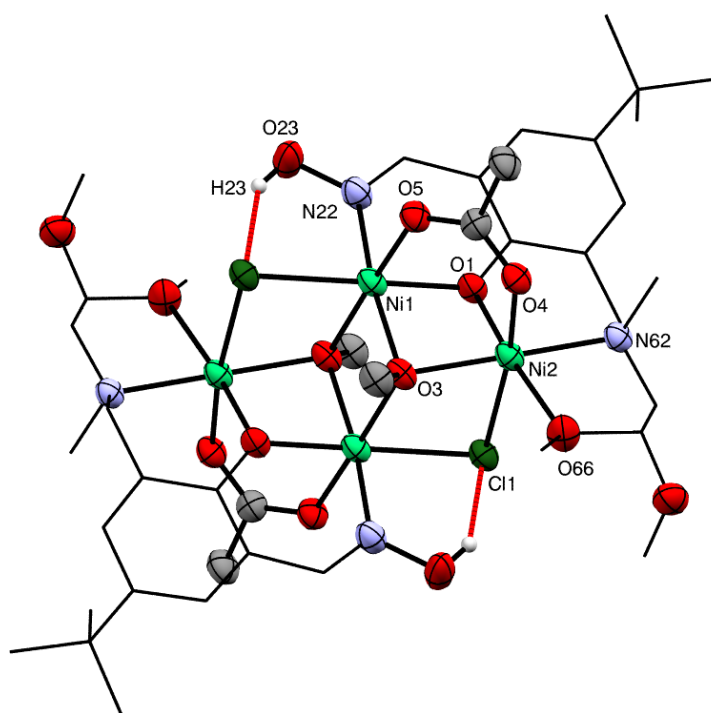


**Figure 3.33:** Crystal structure of the complex [Ni<sub>4</sub>(L2-H)<sub>2</sub>(OAc)<sub>2</sub>(OMe)<sub>2</sub>Cl<sub>2</sub>](Et<sub>2</sub>O)<sub>3</sub>, (**C8**). H atoms, apart from those involved in hydrogen bonding, have been omitted for clarity; Ni<sup>II</sup> = light green, N = blue, O = red, Cl = dark green, C = grey, H = white. Hydrogen bonding represented as red dotted lines. ORTEP view at 30% probability level.

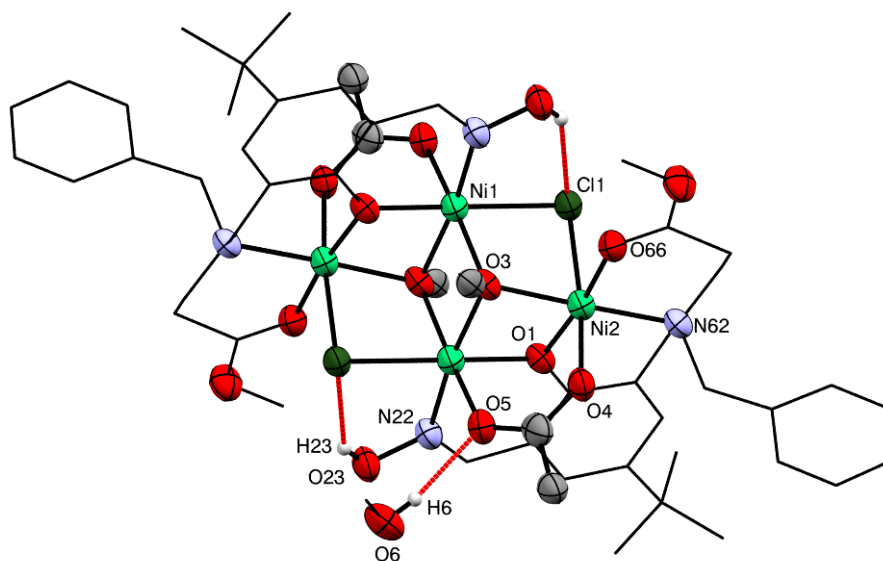


**Figure 3.34:** Crystal structure of the complex  $[\text{Ni}_4(\text{L3-H})_2(\text{OAc})_2(\text{OMe})_2\text{Cl}_2](\text{MeOH})_2$ , (**C9**). H atoms, apart from those involved in hydrogen bonding, have been omitted for clarity; Ni<sup>II</sup> = light green, N = blue, O = red, Cl = dark green, C = grey, H = white. Hydrogen bonding is represented by red dotted lines. ORTEP view at 50% probability level.

**Table 3.15:** Selected bond lengths of the complexes, **C8** and **C9**.

Bond	Length (Å)	Bond	Length (Å)	Bond	Length (Å)
<b>C8</b>					
Ni1-Cl1	2.50(1)	Ni1-N22	1.98(4)	Ni2-O4	2.06(3)
Ni1-O1	2.03(3)	Ni1-O3 <sup>1</sup>	2.12(3)	Ni2-O66	2.09(3)
Ni1-O3	2.01(3)	Ni2-O1	1.95(3)	Ni2-N62	2.11(4)
Ni1-O5	2.11(3)	Ni2-O3	2.08(3)	Ni2-Cl1	2.58(1)
<b>C9</b>					
Ni1-O1	1.99(7)	Ni1-Cl1	2.46(3)	Ni2-N62	2.14(9)
Ni1-N22	2.04(9)	Ni1-O3 <sup>1</sup>	2.05(1)	Ni2-Cl1	2.51(4)
Ni1-O3	2.04(7)	Ni2-O66	2.05(8)	Ni2-O3	2.04(7)
Ni1-O5	2.02(1)	Ni2-O1	1.97(7)	Ni2-O4	2.04(9)

<sup>1</sup> = 1-x, -y, 1-z; <sup>2</sup> = 2-x, 1-y, -z

**Table 3.16:** Selected bond angles of the complexes, **C8** and **C9**.

Atoms	Angle (°)	Atoms	Angle (°)	Atoms	Angle (°)
<b>C8</b>					
Cl1-Ni1-O1	174(9)	O5-Ni1-N22	87.3(1)	O4-Ni2-O66	93.3(1)
Cl1-Ni1-O3	99.5(9)	O5-Ni1-O3 <sup>1</sup>	174(1)	O4-Ni2-N62	90.2(1)
Cl1-Ni1-O5	96.6(8)	N22-Ni1-O3 <sup>1</sup>	98.3(1)	O4-Ni2-Cl1	172(9)
Cl1-Ni1-N22	88.9(1)	O1-Ni2-O3	83.6(1)	O66-Ni2-N62	78.0(1)
Cl1-Ni1-O3 <sup>1</sup>	81.5(8)	O1-Ni2-O4	92.9(1)	O66-Ni2-Cl1	88.1(1)
O1-Ni1-O3	83.4(1)	O1-Ni2-O66	170(1)	N62-Ni2-Cl1	97.5(1)
O1-Ni1-O5	87.9(1)	O1-Ni2-N62	93.7(1)	Ni1-Cl1-Ni2	86.4(4)
O1-Ni1-N22	88.1(1)	O1-Ni2-Cl1	86.8(9)	Ni1-O1-Ni2	95.4(1)
O1-Ni1-O3 <sup>1</sup>	94.4(1)	O3-Ni2-O4	92.0(1)	Ni1-O3-Ni1	92.3(1)
O3-Ni1-O5	93.3(1)	O3-Ni2-O66	104(1)	Ni2-O3-Ni1	98.6(1)
O3-Ni1-N22	171(1)	O3-Ni2-N62	177(1)		
O3-Ni1-O3 <sup>1</sup>	81.4(1)	O3-Ni2-Cl1	80.3(8)		
<b>C9</b>					
O1-Ni1-N22	87.8(3)	O5-Ni1-Cl1	93.6(3)	N62-Ni2-Cl1	92.4(3)
O1-Ni1-O3	83.4(3)	O5-Ni1-O3 <sup>2</sup>	171(3)	N62-Ni2-O3	174(4)
O1-Ni1-O5	89.4(3)	Cl1-Ni1-O3 <sup>2</sup>	84.0(2)	N62-Ni2-O4	93.7(4)
O1-Ni1-Cl1	176(2)	O66-Ni2-O1	173(3)	Cl1-Ni2-O3	83.0(2)
O1-Ni1-O3 <sup>2</sup>	93.4(3)	O66-Ni2-N62	93.8(4)	Cl1-Ni2-O4	174(3)
N22-Ni1-O3	171(4)	O66-Ni2-Cl1	89.2(2)	O3-Ni2-O4	90.9(3)
N22-Ni1-O5	89.6(4)	O66-Ni2-O3	89.6(3)	Ni1-O1-Ni2	96.2(3)
N22-Ni1-Cl1	89.6(3)	O66-Ni2-O4	90.7(3)	Ni2-Cl1-Ni1	84.0(1)
N22-Ni1-O3 <sup>2</sup>	98.9(3)	O1-Ni2-N62	92.7(3)	Ni1-O3-Ni2	92.6(3)
O3-Ni1-O5	91.5(3)	O1-Ni2-Cl1	89.5(2)	Ni1-O3-Ni1	99.6(3)
O3-Ni1-Cl1	99.2(2)	O1-Ni2-O3	83.8(3)		
O3-Ni1-O3 <sup>2</sup>	80.4(3)	O1-Ni2-O4	89.9(3)		

<sup>1</sup> = 1-x, -y, 1-z; <sup>2</sup> = 2-x, 1-y, -z

Conductivity measurements were performed on the complexes **C8** and **C9** to determine their behaviour in solution. For both complexes, measurements performed in DCM indicated that no anions were present in solution, i.e. in DCM, **C8** and **C9** are non-electrolytes. The behaviour of **C9** in MeOH was also measured and it was found that the complex was a 1:1 electrolyte, indicating that for every complex in solution, one chloride anion dissociated from the complex. The measurement of **C8** in MeOH could not be performed due to solubility issues.

The metallic cores of both **C8** and **C9** (Figure 3.32) resemble each other, with the key differences being the Ni-X-Ni angles ( $X = \text{Cl}, \text{OMe}, \text{ or phenolic oxygen}$ ), which results from the different coordination modes of the two different amino chains (R groups) (Figure 3.35). For **C8**, the ligand **L2** is utilised, and coordinates the Ni(II) ion through the amine and one of the methyl ether oxygen atoms (Figure 3.35, left). This bidentate coordination creates a five-membered ring, which is more strained than a six-membered ring and causes the Ni1-Cl1-Ni2, and Ni1-O3-Ni2 angles to become larger and more antiferromagnetically coupled. The complex **C9**, differs from **C8**, by utilising the ligand **L3**. Instead of a five-membered ring, a six-membered ring forms from the coordination of the Ni(II) ion to the amine and carbonyl oxygen (Figure 3.35, right). The extra carbon found between the nitrogen and oxygen binding sites lessens the strain and angle of the Ni1-Cl1-Ni2, and Ni1-O3-Ni2 bridges, a property that leads the exchange pathways towards ferromagnetic coupling (further explained below).

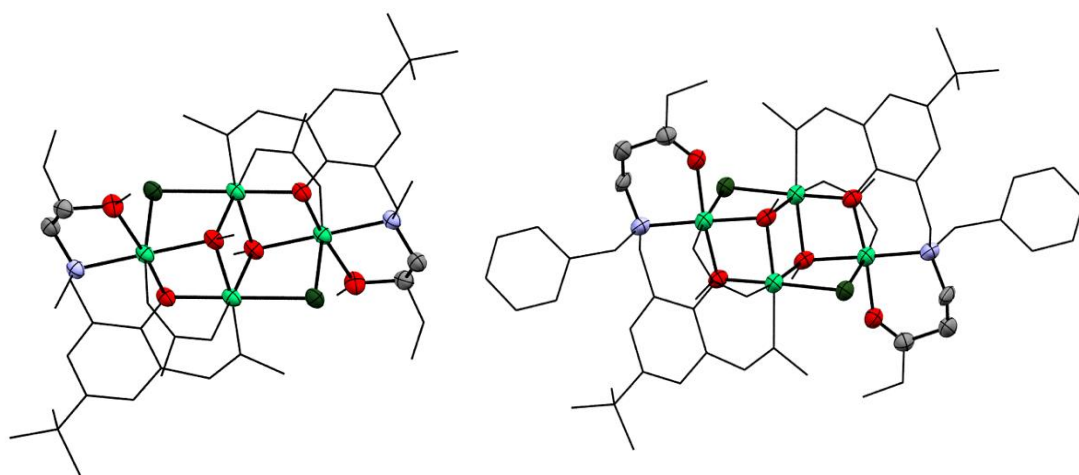


**Figure 3.35:** The metallic cores of the complexes, **C8** and **C9**, illustrating the different coordination modes of the R groups. Ni<sup>II</sup> = light green, N = blue, O = red, Cl = dark green, C = grey. ORTEP view at 30% probability level.

In addition to the two ligands (**L2** and **L3**), there are OMe<sup>-</sup>, OAc<sup>-</sup>, and chloride anions found within the metallic cores. The bridging OMe<sup>-</sup> ions originate from the complexation solvent (MeOH), the OAc anions have come from the Ni(II) metal salt and the chloride anions are from an initial attempt at a 3d/4f structure and are the anion of the 4f metal salt. To avoid any metal contamination during magnetic measurements, the 4f metal salt was able to be replaced with NH<sub>4</sub>Cl during bulk complexations of **C8** and **C9**. The replacement of the chlorine source did not affect the synthesis of **C9** in any way, however, it did result in a longer period of recrystallisation for **C8** (eight weeks instead of five-six weeks), as an ammonium salt impurity crystallised out first.

Direct current (DC) molar magnetic susceptibility,  $\chi_M$ , measurements were performed on powdered polycrystalline samples of the complexes **C8** and **C9**. The  $\chi_M$  measurements were measured in an applied magnetic field,  $B$ , of 0.1 T over a temperature ( $T$ ) range of 2 - 300 K. The results are shown in Figure 3.36 in the form of a  $\chi_M T$  vs.  $T$  plot, where  $\chi_M$  is the molar magnetic susceptibility, and  $M$  is the magnetisation of the sample.

For both complexes, **C8** and **C9**, the  $T = 300$  K  $\chi_M T$  value is close to that expected for four non-interacting Ni(II) ions with  $g = 2.2$  (4.84 cm<sup>3</sup> K mol<sup>-1</sup>). As the temperature is decreased the value of  $\chi_M T$  remains constant to approximately 150 K, below which the two curves diverge. For **C8** the value increases, reaching a maximum of 6.08 cm<sup>3</sup> K mol<sup>-1</sup> at  $T = 15$  K before dropping rapidly to 5.47 cm<sup>3</sup> K mol<sup>-1</sup> at  $T = 2.0$  K. The sharp decrease in  $\chi_M T$  at low temperatures for **C8** can be attributed to intermolecular antiferromagnetic exchange and/or zero-field splitting (ZFS) effects. For **C9** the value of  $\chi_M T$  gradually decreases, reaching a value of 2.04 cm<sup>3</sup> K mol<sup>-1</sup> at  $T = 2.0$  K. The data in both cases is consistent with the presence of competing ferro- and antiferromagnetic exchange interactions between the four Ni(II) ions, with the former dominating in **C8** and the latter dominating in **C9**. The susceptibility were fitted simultaneously using the program PHI and a spin-Hamiltonian of the form:

$$\hat{H} = -2 \sum_{i,j>i}^n \hat{S}_i J_{ij} \hat{S}_j + \mu_B \sum_{i=1}^n \vec{B} g_i \hat{S}_i + \sum_{i=1}^n D [\hat{S}_{z,i}^2 - \hat{S}_i(\hat{S}_i + 1)/3] \quad (\text{eqn. 5})$$



where  $\hat{S}$  is a spin operator,  $J$  is the pairwise isotropic magnetic exchange interaction between constitutive Ni(II) centres,  $\mu_B$  is the Bohr magneton,  $\vec{B}$  the external static magnetic field,  $g$  the isotropic  $g$ -factor of Ni(II) (fixed to  $g = 2.2$ ), the indices  $i$  and  $j$  refer to the Ni ions ( $n = 4$ ),  $D$  is the second-order single-ion uniaxial anisotropy parameter of Ni(II), and  $\hat{S}_{z,i}^2$  is the Cartesian component of spin operator  $\hat{S}$  of the  $i^{\text{th}}$  Ni(II) centre along the  $z$ -direction of the local coordinate frame.<sup>62</sup> Best fit parameters employing the exchange interaction model depicted in the inset of Figure 3.36 afforded the best fit parameters:  $J_1 = +6.23 \text{ cm}^{-1}$ ,  $J_2 = -6.16 \text{ cm}^{-1}$ ,  $J_3 = +3.41 \text{ cm}^{-1}$  and  $D_{\text{Ni}} = -2.99 \text{ cm}^{-1}$  for **C8** and  $J_1 = +4.12 \text{ cm}^{-1}$ ,  $J_2 = -9.93 \text{ cm}^{-1}$ ,  $J_3 = +3.16 \text{ cm}^{-1}$  and  $D_{\text{Ni}} = -2.99 \text{ cm}^{-1}$  for **C9** (Figure 3.36). The sign and magnitude of the exchange interactions are similar to those observed in analogous species containing Ni-O-Ni and Ni-Cl-Ni bridging units.<sup>63</sup> It is interesting to note when comparing **C8** and **C9**, the  $J_1$  [Ni(Cl)( $\mu_3$ -O)Ni] and  $J_3$  [Ni( $\mu_3$ -O)( $\mu_2$ -O)Ni] values become less ferromagnetic, whilst the  $J_2$  [Ni( $\mu_3$ -O) $_2$ Ni] value becomes more ferromagnetic. These differences can be attributed to changes in the Ni-X-Ni angles of the magnetic core brought about by the change in ligand sterics, the most significant of which appears to be the [Ni(Cl)(O)Ni] angles mediating  $J_1$ , both of which increase by up to  $3^\circ$ . For both **C8** and **C9**, the  $S$  states are of the same magnitude as  $D(\text{Ni})$  and thus will be further split by ZFS. The ground  $S$  states become hard to define within the weak exchange limit thus no exact values can be determined (Figure 3.37).

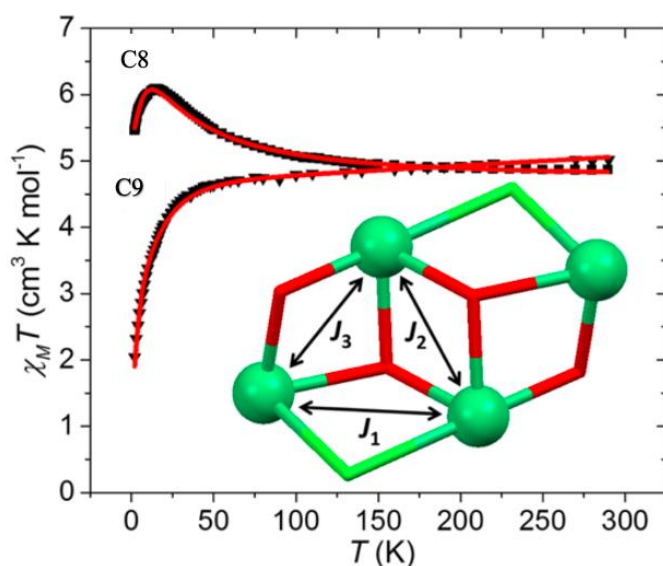


**Figure 3.36:** Plot of the  $\chi_M T$  product versus  $T$  for **C8** and **C9** in the  $T = 300 - 1.8 \text{ K}$  temperature range, in an applied field,  $B = 0.1 \text{ T}$ . The solid red lines are a fit of the experimental data.

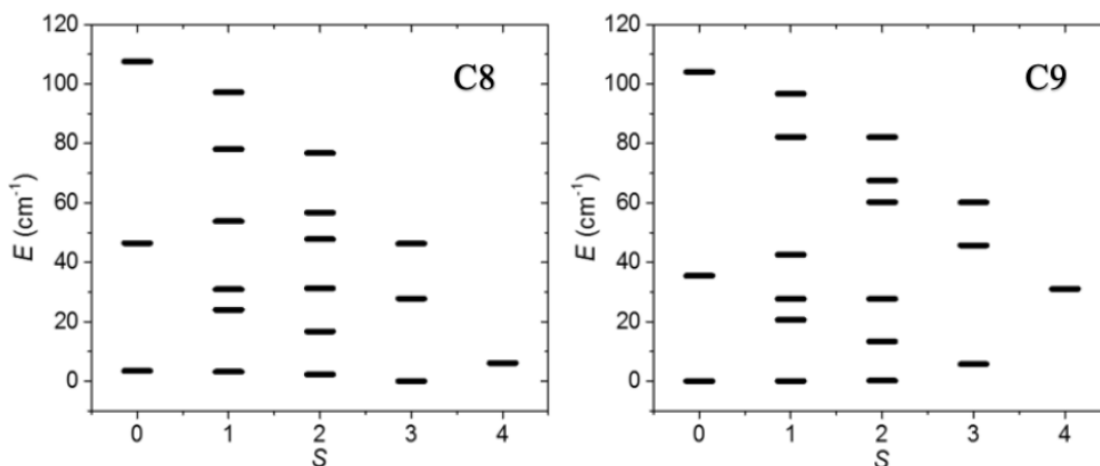


**Figure 3.37:** Plot of lowest lying spin states ( $S$ ) versus energy ( $E$ ) as obtained from the isotropic fit of the susceptibility data for **C8** (left) and **C9** (right).

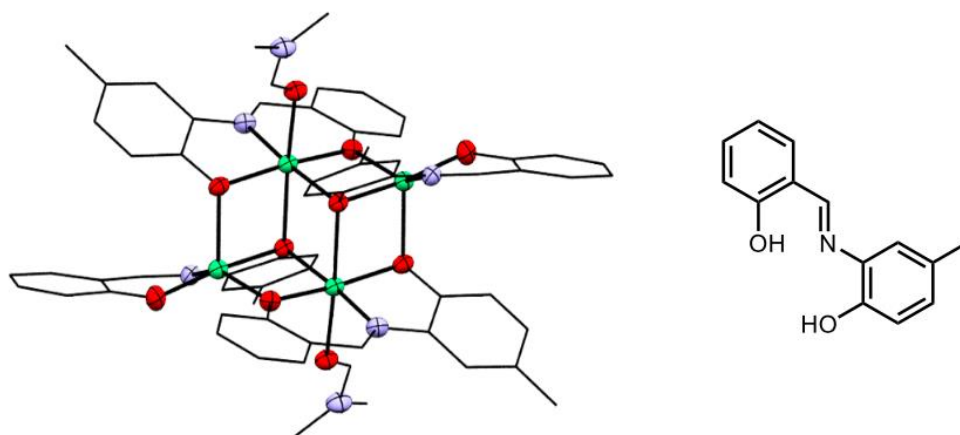


**Figure 3.38:** Crystal structure of the tetranuclear  $\text{Ni}^{\text{II}}$  defective dicubane produced by Perlepes *et al.* (left) and the corresponding ligand utilised (right).  $\text{Ni}^{\text{II}}$  = green, N = blue, O = red.

In 2014 and 2019, similar tetranuclear  $\text{Ni}(\text{II})$  structures with defective dicubanes were produced by Perlepes *et al.* (Figure 3.38) and Slater-Parry *et al.* (Figure 3.39) respectively. The magnetic properties of both complexes were investigated, and it was found that the bridges between the  $\text{Ni}(\text{II})$  ions were crucial to the number of exchange interactions present within the complex, and subsequently the resulting magnetic properties. The complexes

incorporate H<sub>2</sub>Sai and salicylaldamine based ligands, with added functionality in the form of phenolic oxygens for Perlepes *et al.* Both complexes have two different anions bridging the Ni(II) ions; Perlepes *et al.* has two different phenolic oxygens, whereas Slater-Parry *et al.* has phenolic oxygens and OH<sup>-</sup> anions. Although both complexes only have two different types of bridges between metal ions, the structure produced by Perlepes *et al.* has two different body-wingtip bridges producing two different exchange pathways, whereas the structure of Slater-Parry *et al.* has the same bridge between the body and wingtip ions, resulting in a single pathway. The complexes **C8** and **C9** resemble the structure by Perlepes *et al.* in that in addition to the body-body exchange pathway, two different body-wingtip bridges create two different exchange pathways.

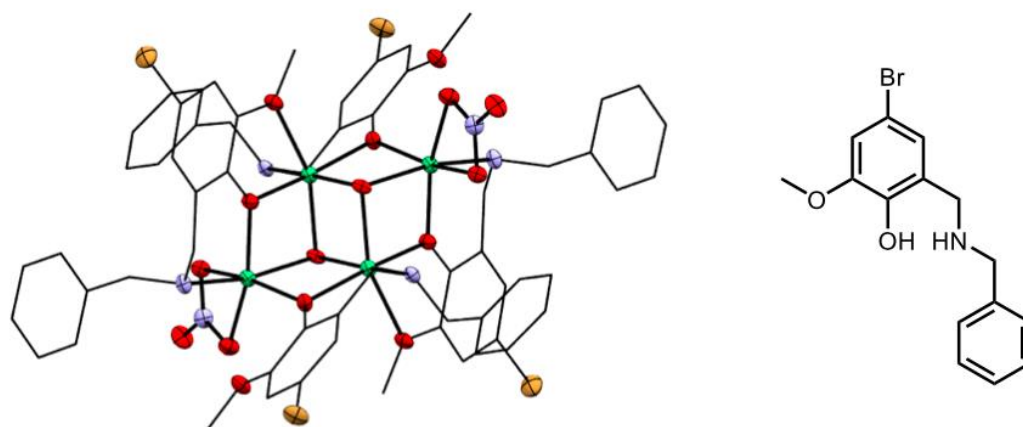


**Figure 3.39:** Crystal structure of the tetranuclear Ni<sup>II</sup> defective dicubane produced by Slater-Parry *et al.* (left) and the corresponding ligand (right). Ni<sup>II</sup> = green, N = blue, O = red, Br = dark yellow.

Chloride bridging, more specifically,  $\mu_2$ -chloride bridging has been seen previously in the Ni(II)<sub>4</sub>Dy(III)<sub>2</sub> complex produced by Zhao *et al.* (Figure 3.40, left).<sup>63f</sup> This complex exhibited a defective dicubane metallic core and was explored for its potential SMM properties and for use as a new magnetic material. The ligand employed was N<sub>1</sub>,N<sub>3</sub>-bis-(3-methoxysalicylidene)-diethylenetriamine (Figure 3.40, right), and provided a phenolic oxygen to bridge between Dy(III) and Ni(II) ions. The remaining bridging groups are OH<sup>-</sup> anions ( $\mu_3$ -bridges), and chloride anions (between Ni ions). The Ni-Cl bond lengths (2.47(2) Å) were found to agree within the average length found for **C8** and **C9** (2.52 Å). The Ni-Cl-Ni bond angle of the structure by Zhao *et al.* was found to resemble both the angles of

**C8** and **C9** as a result of experimental error, however, the exchange couplings between the three structures were found to be significantly different. The bond angle of **C8** ( $86.4(4)^\circ$ ) resulted in a ferromagnetic exchange interaction ( $+6.23 \text{ cm}^{-1}$ ) between the Ni(II) centres; the exchange interaction for **C9** was found to be ferromagnetic ( $+4.12 \text{ cm}^{-1}$ ) with the difference in interactions a result of a  $3^\circ$  difference between the bond angles. The ferromagnetic exchange interaction found for the structure by Zhao *et al.* of  $+1.95 \text{ cm}^{-1}$  indicates that in addition to the bond angle distortion, other factors are at play concerning the exchange interactions of the Ni(II) centres.

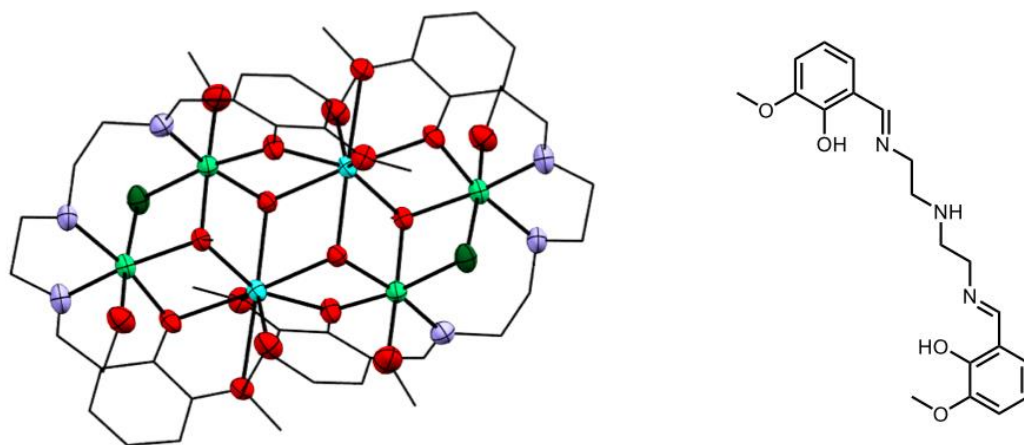


**Figure 3.40:** Crystal structure of the Ni<sup>II</sup>/Dy<sup>III</sup> complex produced by Zhao *et al.*, which contains a double defective dicubane topology (left). The ligand utilised can be found on the right. Ni<sup>II</sup> = light green, Dy<sup>III</sup> = aqua, N = blue, O = red, Cl = dark green.

The tetranuclear Ni(II) complex (Figure 1.15) produced by Jiang *et al.* discussed in Section 1.3, explores the effect of OMe<sup>-</sup> bridging between the two body Ni(II) ions.<sup>28b</sup> Jiang *et al.* found that the OMe<sup>-</sup> bridges between the body ions, enhanced the coupling between the body-wingtip ions. This result is similar to what was found for both **C8** and **C9**, as the body-wingtip couplings were found to be larger and more ferromagnetic than the body-body couplings. Both the complexes by Jiang *et al.* and the complexes **C8** and **C9** indicate that OMe<sup>-</sup> bridging enhances adjacent couplings. This is beneficial as these bridges are generally found to have larger angle distortions and result in larger magnetic couplings.

## 4.0 Experimental Methods

### 4.1 General Procedures

All starting materials purchased from commercial sources were used without purification unless otherwise stated. *t*Bu phenol was dried *in vacuo* prior to use, and NH<sub>4</sub>OH·HCl was not recrystallised from MeOH. Analytical grade solvents used in all reactions were used as purchased, unless stated. HPLC grade MeOH was stored over 3 Å sieves for a week before use. All reactions were carried out in acetone-washed, oven-dried glassware under ambient conditions unless otherwise stated. Glassware utilised in crystallisation attempts was either used straight from purchase, or washed with deionised H<sub>2</sub>O, soaked in a KOH/IPA base bath, rinsed with H<sub>2</sub>O and acetone, and air dried. Column chromatography was performed on silica gel (grade 60, mesh size 230-400, Scharlau) in a slurry of the eluent.

All new organic compounds have been characterised by NMR, ESI-MS, and ATR-FTIR. New 3d complexes have been characterised by a combination of X-ray, IR, CHN, UV/Vis, and magnetic susceptibility measurements, with ESI-MS characterisation performed on complexes **C1-C4**, <sup>19</sup>F NMR performed on **C4**, and Mössbauer measurements performed on the iron complexes, **C5** and **C7**. <sup>1</sup>H and <sup>13</sup>C NMR spectra were recorded at room temperature on Bruker-500 and Bruker-700 Avance instruments, with the <sup>1</sup>H shift of the solvent used as an internal standard; Microwave syntheses were performed using a CEM Discovery Monomode microwave synthesiser; <sup>19</sup>F NMR spectrum was recorded on a Magritek Spinsolve benchtop NMR instrument (43 MHz) and referenced to a trifluoroethanol external standard. ESI-MS spectra were collected on a Dionex UltiMate 3000 and run in positive ion mode; ATR-FTIR spectra were collected on a Nicolett 5700 FT-IR; UV/Vis spectroscopy measurements were performed on a Shimadzu UV-3101PC Spectrophotometer; Conductivity measurements were performed on a Phillips PW9509 Conductivity meter; The magnetic susceptibility measurements of **C1-C3** were performed on a Sherwood Scientific magnetic susceptibility balance, and the CHN elemental analysis was collected by the Campbell Microanalytical Laboratory, Chemistry Department, University of Otago. Consistent elemental analysis was not achieved for the ligand precursor, **L3a**, and the ligand, **L2**, due to their oily nature. The elemental analyses for complexes, **C3-C5**, **C7**, and **C9** were shown to obtain a small amount of impurity (most likely

an ammonium salt) resulting from the isolation process of the crystals, hence CHN results for these complexes were not consistent with the X-ray formulations. Time constraints have meant that analysis will now need to be repeated at a later date.

Variable-temperature, solid-state DC magnetic susceptibility data of **C4-C6** and **C8-C9** were performed by Prof. Euan Brechin at the University of Edinburgh. The data was collected with a Quantum Design MPMS-XL SQUID magnetometer equipped with a 7 T DC magnet on powdered polycrystalline samples embedded in eicosane. Diamagnetic corrections were applied to the observed paramagnetic susceptibilities by using Pascal's constants.

Mössbauer measurements were performed by Assoc. Prof. Guy Jameson at the University of Melbourne. Data was recorded on a SEE Co. (Science Engineering and Education Co., MN) spectrometer, equipped with a closed cycle SVT-400 cryostat from Janis Research Co. The data was collected in a constant acceleration mode in a transmission geometry. The isomer shift (zero velocity) of the Mössbauer spectra were determined relative to the centroid of the RT spectrum of a metallic iron foil. The data analysis was performed using the program WMOSS.

The X-ray data for **C3** was collected at the Haijima Rigaku laboratory, Tokyo. Data was collected at reduced temperature (130 K) on a four-circle diffractometer, XtaLAB AFC12 (RINC): Kappa single, equipped with a rotating-anode X-ray tube (dual wavelength) Rigaku (Mo) X-ray DW source and a CCD plate. Crystals were irradiated with Mo K $\alpha$  ( $\lambda = 0.71073$  Å) X-rays. Data was collected and processed using the program CrysAlisPro 1.171.40.12b (Rigaku Oxford Diffraction, 2018), Empirical absorption correction using spherical harmonics, implemented in SCALE3 ABSPACK scaling algorithm.<sup>64</sup> The structure was solved by direct methods SHELXT and was refined using SHEXL in the OLEX2 program.<sup>47a, 65</sup> Non-hydrogen atoms were refined anisotropically. Hydrogen atoms were calculated to their ideal positions unless stated otherwise and refined by using a riding model with fixed isotropic *U* values.

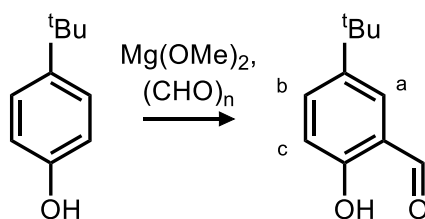
The X-ray data for the remaining structures (**C1-2**, **C4-9**) was collected at reduced temperature (123 K) on a Rigaku Spider diffractometer equipped with a copper rotating anode X-ray source and a curved image plate detector. Crystals were mounted in Fomblin and transferred into the cold gas stream of the detector and irradiated with graphite

monochromated Cu K $\alpha$  ( $\lambda = 1.54178 \text{ \AA}$ ) X-rays. Data was collected using the program Crystal Clear (v. 1.4.0) and processed using FS PROCESS. The structures were solved by direct methods SHELXS and Superflip, and were refined using SHELXL in the OLEX2 program.<sup>47a, 65a, 66</sup> Non-hydrogen atoms were refined anisotropically; hydrogen atoms were calculated to their ideal positions unless stated otherwise and refined by using a riding model with fixed isotropic  $U$  values. Disordered solvent and anion regions in the complexes, **C3**, **C5**, **C6**, and **C7** were treated in the manner described by Spek as implemented in Olex2, the details of which can be found in Chapter 3.0.<sup>47</sup>

## 4.2 Ligand Synthesis

### 4.2.1 Synthesis of Precursors 1 and 2

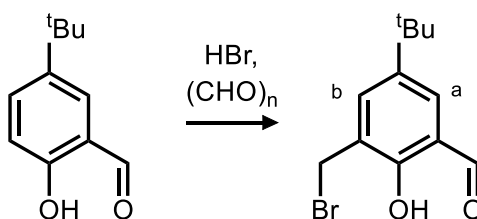
#### 5-*tert*-Butyl-2-hydroxybenzaldehyde (**1**)



The compound **1** was prepared from an adapted version of Aldred *et al.*<sup>38</sup> Dry Mg turnings (14.8 g, 0.609 mol, 1.70 eq) were added to a stirred solution of 3:7 dry MeOH/toluene (200 mL) and 8% Mg(OMe)<sub>2</sub> solution (100 mL), and refluxed under argon overnight, ensuring all Mg had dissolved. The reaction mixture was then added to a stirred solution of 4-*tert*-butylphenol (153 g, 1.02 mol, 1.00 eq) in toluene (100 mL) and refluxed for three hours. Toluene (100 mL) was added prior to fractionally distilling off a MeOH/toluene azeotrope under reduced pressure until the reaction mixture appeared to be a thick consistency. A paraformaldehyde slurry (22.5 g, 1.50 mol, 1.50 eq) in toluene (150 mL) was added piecewise over one hour, with volatile by-products removed by vacuum distillation between aliquots. Toluene (150 mL) was added to the reaction mixture and left to stir overnight at 85 °C under dry conditions, producing a thick yellow/brown mixture. A solution of 30% H<sub>2</sub>SO<sub>4</sub> (500 mL) was added dropwise over an hour, then stirred vigorously for a further two hours forming two yellow layers. The aqueous layer was extracted with toluene (3 x 100 mL), and the combined organic layers were washed with a 10% H<sub>2</sub>SO<sub>4</sub> solution (100 mL) and deionised H<sub>2</sub>O (3 x 100 mL), dried over anhydrous MgSO<sub>4</sub>, filtered and concentrated *in vacuo* to afford crude **1** (82.4 g, 0.473 mol) as a brown oil. This was subsequently purified by silica gel column chromatography, eluting with 4:1 *n*Hex : EtOAc, (*R*<sub>f</sub> = 0.75) affording purified **1** as a dark orange oil (55.3 g, 62%). The <sup>1</sup>H NMR spectrum agreed with literature values (500 MHz, CDCl<sub>3</sub>): δ 10.90 (1H, s, Ar-OH), 9.92 (1H, s, CH=O), 7.61 (1H, dd, *J*<sub>1</sub> = 8.8 Hz, *J*<sub>2</sub> = 2.5 Hz, *c*), 7.54 (1H, d, *J* = 2.5 Hz, *b*), 6.97 (1H, d, *J* = 8.8 Hz, *a*), 1.36 (9H, s, *t*Bu).



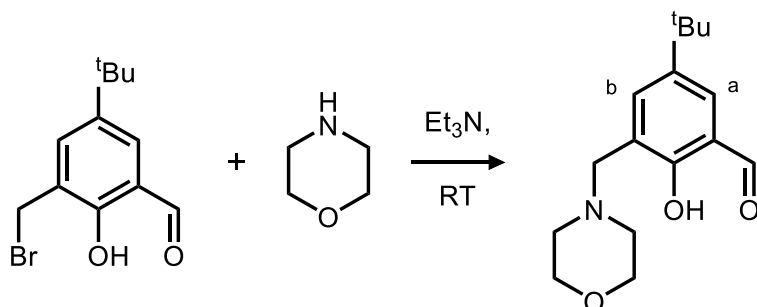
## 5-*tert*-Butyl-3-bromomethyl-2-hydroxybenzaldehyde (**2**)



The compound **2** was prepared as per the method of Meier *et al.*<sup>39</sup> **1** (81.6 g, 0.458 mol, 1.00 eq), HBr (48%, 390 mL, 3.45 mol, 7.50 eq), and paraformaldehyde (20.4 g, 0.680 mol, 1.50 eq) were added together and stirred at 0 °C. Concentrated H<sub>2</sub>SO<sub>4</sub> (6.00 mL) was added slowly dropwise to the mixture stirring at 0 °C until a light-yellow colour persisted, the mixture was then refluxed for 20 hours at 70 °C. After cooling to RT, deionised H<sub>2</sub>O (250 mL) was added. The aqueous layer extracted with DCM (5 x 200 mL) and combined organic layers were dried over anhydrous Na<sub>2</sub>SO<sub>4</sub>, filtered and concentrated *in vacuo* to produce crude **2** as a brown oil (80.0 g, 64.5%). The crude material was recrystallised from hot pentane (10% w/v) to give light yellow block shaped crystals of purified **2** (78.8 g, 0.291 mol, 63.5%). The <sup>1</sup>H NMR spectrum was in agreement with literature values, (500 MHz, CDCl<sub>3</sub>): δ 11.32 (1H, s, Ar-OH), 9.90 (1H, s, CH=O), 7.64 (1H, d, J = 2.4 Hz, b), 7.51 (1H, d, J = 2.5 Hz, a), 4.59 (2H, s, CH<sub>2</sub>-Br), 1.34 (9H, s, *t*Bu).

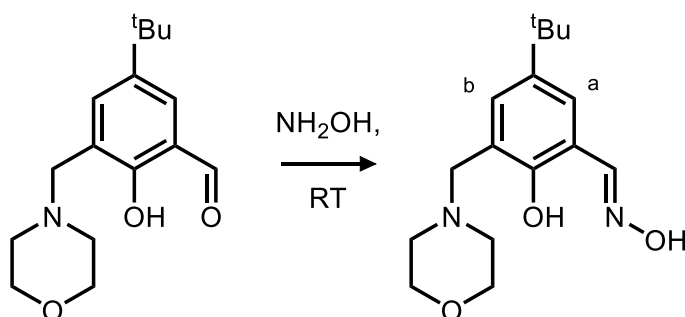
#### 4.2.2 Synthesis of L1

##### 5-*tert*-Butyl-3-(4-morpholinomethyl)-2-hydroxybenzaldehyde (**L1a**)



The compound **L1a** was prepared from an adapted version of Stevens and Plieger.<sup>41</sup> Solutions of Morpholine (0.32 mL, 3.71 mmol, 1.0 eq.) and **2** (1.02 g, 3.71 mmol, 1.0 eq.), both in  $\text{CHCl}_3$  (20 mL) were added dropwise to a stirred solution of  $\text{Et}_3\text{N}$  (0.51 mL, 3.71 mmol, 1.0 eq.) in  $\text{CHCl}_3$  (20 mL). The resulting bright yellow solution was stirred for 24 hours at RT. The solution was washed with deionised  $\text{H}_2\text{O}$  (3 x 60 mL), and the combined organic layers were dried over anhydrous  $\text{MgSO}_4$ , filtered and concentrated *in vacuo* to afford **L1a** as a white solid (0.96 g, 3.46 mmol, 91%). The  $^1\text{H}$  NMR spectrum agreed with literature values (500 MHz,  $\text{CDCl}_3$ ):  $\delta$  10.25 (1H, s,  $\text{CH}=\text{O}$ ), 7.61 (1H, d,  $J = 2.5$  Hz, *b*), 7.40 (1H, d,  $J = 2.5$  Hz, *a*), 3.76 (4H, t,  $J = 4.5$  Hz,  $\text{CH}_2\text{-CH}_2\text{-O}$ ), 3.71 (2H, s, Ar- $\text{CH}_2\text{-N}$ ), 2.58 (4H, br s,  $\text{CH}_2\text{-CH}_2\text{-N}$ ), 1.30 (9H, s, *tBu*).

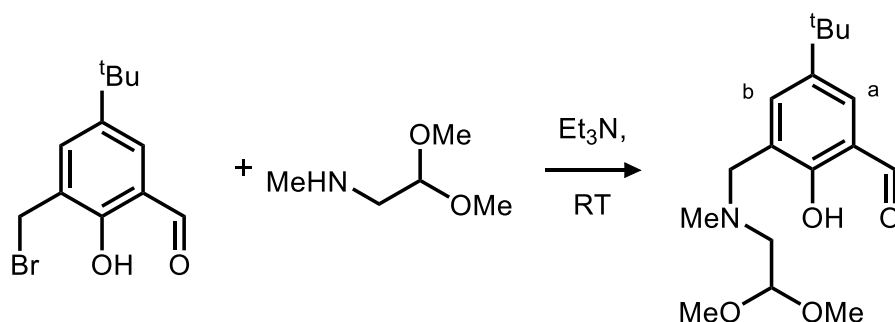
### 5-*tert*-Butyl-3-(4-morpholinomethyl)-2-hydroxybenzaldehyde oxime (L1)



The compound **L1** was prepared from an adapted version of De Silva *et al.*<sup>35e</sup> A solution of  $\text{NH}_2\text{OH}\cdot\text{HCl}$  (0.25 g, 3.54 mmol, 1.0 eq.) in EtOH (30 mL) was neutralised with a solution of KOH (0.20 g, 3.53 mmol, 1.0 eq.) in EtOH (30 mL). The filtered solution was added slowly dropwise into a solution of **L1a** (0.96 g, 3.53 mmol, 1.0 eq.) in EtOH (50 mL). The resulting solution was stirred for 24 hours at RT. The light-yellow solution was concentrated *in vacuo* affording an oil, which was redissolved in  $\text{CHCl}_3$  (30 mL). This solution was washed with deionised  $\text{H}_2\text{O}$  (3 x 30 mL) and the combined organic layers dried over anhydrous  $\text{MgSO}_4$ , filtered and concentrated *in vacuo* affording **L1** as a white solid (0.88 g, 87%). The  $^1\text{H}$  NMR spectrum was in agreement with literature values, (500 MHz,  $\text{CDCl}_3$ ):  $\delta$  8.42 (1H, s,  $\text{CH}=\text{N}$ ), 7.45 (1H, d,  $J = 2.6$  Hz, *b*), 7.12 (1H, d,  $J = 2.6$  Hz, *a*), 3.77 (4H, t,  $J = 4.6$  Hz,  $\text{CH}_2-\text{CH}_2-\text{O}$ ), 3.71 (2H, s, Ar- $\text{CH}_2-\text{N}$ ), 2.59 (4H, br s,  $\text{CH}_2-\text{CH}_2-\text{N}$ ), 1.29 (9H, s, *t*Bu).

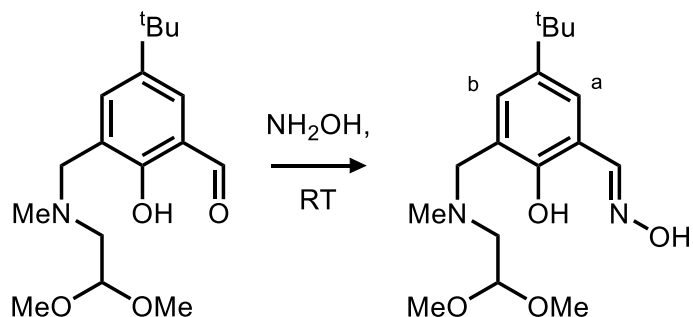
### 4.2.3 Synthesis of L2

#### 5-*tert*-Butyl-3-(4-(1,1-dimethoxy-*N*-methylmethanamino))-2-hydroxybenzaldehyde (L2a)



The compound **L2a** was prepared from an adapted version of Stevens and Plieger.<sup>41</sup> Solutions of 1,1-dimethoxy-*N*-methylmethanamine (0.47 mL, 3.71 mmol, 1.0 eq.) and **2** (1.03 g, 3.71 mmol, 1.0 eq.), both in  $\text{CHCl}_3$  (20 mL) were added dropwise to a stirred solution of  $\text{Et}_3\text{N}$  (0.51 mL, 3.71 mmol, 1.0 eq.) in  $\text{CHCl}_3$  (20 mL). The resulting bright yellow solution was stirred for 24 hours at RT. The solution was washed with deionised  $\text{H}_2\text{O}$  (3 x 60 mL), and the combined organic layers were dried over anhydrous  $\text{MgSO}_4$ , filtered and concentrated *in vacuo* to afford a **L2a** as a yellow oil (1.10 g, 3.56 mmol, 97%).  $^1\text{H}$  NMR (500 MHz,  $\text{CDCl}_3$ ):  $\delta$  10.33 (1H, s,  $\text{CH}=\text{O}$ ), 7.62 (1H, d,  $J = 2.2$  Hz, *b*), 7.35 (1H, d,  $J = 2.2$  Hz, *a*), 4.59 (1H, t,  $J = 5.4$  Hz,  $\text{CH}_2\text{-CH}$ ), 3.77 (2H, s,  $\text{Ar-CH}_2\text{-N}$ ), 3.38 (6H, s,  $\text{O-CH}_3$ ), 2.66 (2H, d,  $J = 5.4$  Hz,  $\text{N-CH}_2\text{-CH}$ ), 2.37 (3H, s,  $\text{N-CH}_3$ ), 1.30 (9H, s, *t*Bu);  $^{13}\text{C}$  NMR (125.7 MHz,  $\text{CDCl}_3$ ):  $\delta$  192.4, 159.2, 141.9, 133.3, 125.0, 123.7, 122.0, 102.2, 59.6, 58.2, 53.7, 42.6, 34.1, 31.3; IR:  $\bar{\nu} = 2957$  (C-H); 1678 (C=O); 1652 (C-H); 1604 (C=C); 1395 (C-H); 1364 (O-H); 1124 (C-N); 1073  $\text{cm}^{-1}$  (C-O); MS:  $m/z$  (ESI) 310  $[\text{M}+\text{H}]^+$ ; UV/Vis ( $\epsilon$ , L/mol cm) in MeOH: 337.0 (3286), 259.5 (7360), 218.0 (14258); elemental analysis calcd (%) for  $\text{C}_{17}\text{H}_{27}\text{NO}_4$ : C 65.99, H 8.80, N 4.53; found: C 66.55, H 8.64, N 4.76.

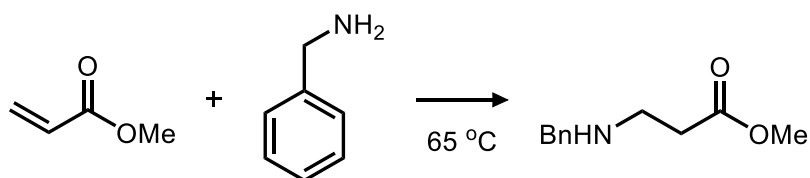
**5-*tert*-Butyl-3-(4-(1,1-dimethoxy-*N*-methylmethanamino))-2-hydroxybenzaldehyde oxime (L2)**



The compound **L2** was prepared from an adapted version of De Silva *et al.*<sup>35e</sup> A solution of  $\text{NH}_2\text{OH}\cdot\text{HCl}$  (0.24 g, 3.54 mmol, 1.0 eq.) in EtOH (30 mL) was neutralised with a solution of KOH (0.20 g, 3.53 mmol, 1.0 eq.) in EtOH (30 mL). The filtered solution was added slowly dropwise to a solution of **L2a** (0.98 g, 3.53 mmol, 1.0 eq.) in EtOH (50 mL). The resulting solution was stirred for 24 hours at RT. The light-yellow solution was concentrated *in vacuo* affording an oil, which was redissolved in  $\text{CHCl}_3$  (30 mL). This solution was washed with deionised  $\text{H}_2\text{O}$  (3 x 30 mL) and the combined organic layers were dried over anhydrous  $\text{MgSO}_4$ , filtered and concentrated *in vacuo* affording **L2** as a yellow oil (0.94 g, 91%).  $^1\text{H}$  NMR (500 MHz,  $\text{CDCl}_3$ ):  $\delta$  8.37 (1H, s,  $\text{CH}=\text{N}$ ), 7.36 (1H, d,  $J = 2.5$  Hz, *b*), 7.13 (1H, d,  $J = 2.5$  Hz, *a*), 4.62 (1H, t,  $J = 5.2$  Hz,  $\text{CH}_2\text{-CH}$ ), 3.74 (2H, s,  $\text{Ar-CH}_2\text{-N}$ ), 3.36 (6H, s,  $\text{O-CH}_3$ ), 2.67 (2H, d,  $J = 5.2$  Hz,  $\text{N-CH}_2\text{-CH}$ ), 2.36 (3H, s,  $\text{N-CH}_3$ ), 1.27 (9H, s, *tBu*);  $^{13}\text{C}$  NMR (125.7 MHz,  $\text{CDCl}_3$ ):  $\delta$  154.2, 148.6, 141.6, 128.2, 123.6, 122.4, 117.7, 102.2, 60.2, 58.2, 53.6, 42.5, 34.0, 31.4; IR:  $\bar{\nu} = 3279$  (O-H); 2959 (C-H); 1616 (C=N); 1394 (C-H); 1363 (O-H); 1126 (C-N);  $1070\text{ cm}^{-1}$  (C-O); MS:  $m/z$  (ESI) 325  $[\text{M}+\text{H}]^+$ ; UV/Vis ( $\epsilon$ , L/mol cm) in MeOH: 315.0 (3693), 261.0 (8515), 217.5 (18479).

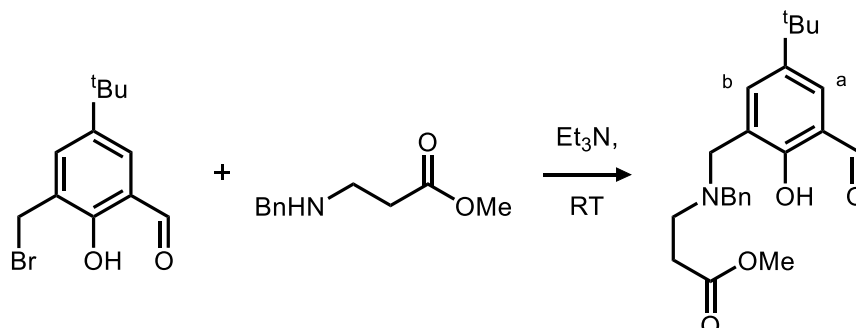
#### 4.2.4 Synthesis of L3

##### ***N*-Benzyl- $\beta$ -alanine methyl ester**



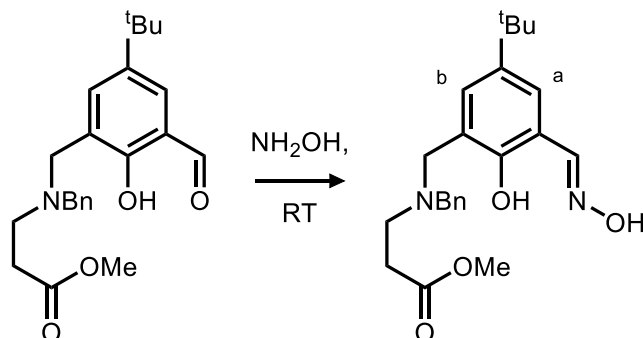
*N*-Benzyl- $\beta$ -alanine methyl ester was prepared as per the method of Cruz-Huerta *et al.*<sup>40</sup> Methyl acrylate (1.70 mL, 18.5 mmol, 1.1 eq.) and benzylamine (1.85 mL, 16.8 mmol, 1.0 eq.) were added together in MeOH (10 mL) and placed in a microwave reaction vessel. The solution was degassed, charged with argon, then sealed and reacted for 10 minutes at 65 °C. The resulting colourless solution was concentrated *in vacuo* to afford crude *N*-benzyl- $\beta$ -alanine methyl ester as a colourless oil. Crude *N*-benzyl- $\beta$ -alanine methyl ester was purified by silica gel column chromatography, eluting with 4:1 *n*Hex : EtOAc ( $R_f$  = 0.75) affording purified *N*-benzyl- $\beta$ -alanine methyl ester as a colourless oil (3.27 g, 16.9 mmol, 95%). The <sup>1</sup>H NMR spectrum was in agreement with literature values, (500 MHz, CDCl<sub>3</sub>):  $\delta$  7.42-7.29 (5H, m, C<sub>6</sub>H<sub>5</sub>), 3.80 (2H, s, C<sub>6</sub>H<sub>5</sub>-CH<sub>2</sub>), 3.67 (3H, s, OMe), 2.89 (2H, t, J = 6.5 Hz, BnHN-CH<sub>2</sub>), 2.54 (2H, t, J = 6.5 Hz, CH<sub>2</sub>-COO), 1.82 (1H, br s, NH).

**5-tert-Butyl-3-methylene-(N-benzyl-β-alanine methyl ester)-2-hydroxybenzaldehyde (L3a)**



The compound **L3a** was prepared from an adapted version of Stevens and Plieger.<sup>41</sup> Solutions of *N*-benzyl-β-alanine methyl ester (13.5 g, 75.4 mmol, 1.0 eq.) and **2** (20.5 g, 75.4 mmol, 1.0 eq.), both in CHCl<sub>3</sub> (100 mL) were added dropwise to a stirred solution of Et<sub>3</sub>N (10.5 mL, 75.4 mmol, 1.0 eq.) in CHCl<sub>3</sub> (100 mL). The resulting bright yellow solution was stirred for 24 hours at RT. The solution was washed with deionised H<sub>2</sub>O (3 x 100 mL), and the combined organic layers were dried over anhydrous MgSO<sub>4</sub> and concentrated *in vacuo* to afford crude **L3a** as a yellow oil. This was purified by silica gel column chromatography, eluting with 1:1 *n*Hex : Et<sub>2</sub>O (*R<sub>f</sub>* = 0.75) affording purified **L3a** as a dark yellow oil (24.2 g, 60.7 mmol, 87%). <sup>1</sup>H NMR (500 MHz, CDCl<sub>3</sub>): δ 10.19 (1H, s, CH=O), 7.55 (1H, d, *J* = 2.5 Hz, *b*), 7.50 (1H, d, *J* = 2.5 Hz, *a*), 7.36-7.28 (5H, m, C<sub>6</sub>H<sub>5</sub>-CH<sub>2</sub>), 3.75 (2H, s, C<sub>6</sub>H<sub>5</sub>-CH<sub>2</sub>), 3.66 (2H, s, Ar-CH<sub>2</sub>-NBn), 3.64 (3H, s, OMe), 2.89 (2H, t, *J* = 7.2 Hz, NBn-CH<sub>2</sub>-CH<sub>2</sub>), 2.58 (2H, t, *J* = 7.2 Hz, CH<sub>2</sub>-CH<sub>2</sub>-COO), 1.31 (9H, s, *t*Bu); <sup>13</sup>C NMR (176 MHz, CDCl<sub>3</sub>): δ 193.5, 172.5, 158.6, 142.2, 137.5, 133.93, 129.2, 128.5, 127.5, 126.0, 124.8, 121.4, 58.3, 53.9, 51.7, 49.3, 34.1, 32.2, 31.3; IR:  $\bar{\nu}$  = 2956 (C-H); 1737 (C=O); 1679 (C=O); 1651 (C=C); 1454 (C-H); 1364 (O-H); 1215 (C-O); 1028 cm<sup>-1</sup> (C-N); MS: *m/z* (ESI) 384 [M+H]<sup>+</sup>; UV/Vis ( $\epsilon$ , L/mol cm) in MeOH: 339.5 (3455), 260.0 (8766), 205.5 (22883).

**5-tert-Butyl-3-methylene-(N-benzyl-β-alanine methyl ester)-2-hydroxybenzaldehyde oxime (L3)**

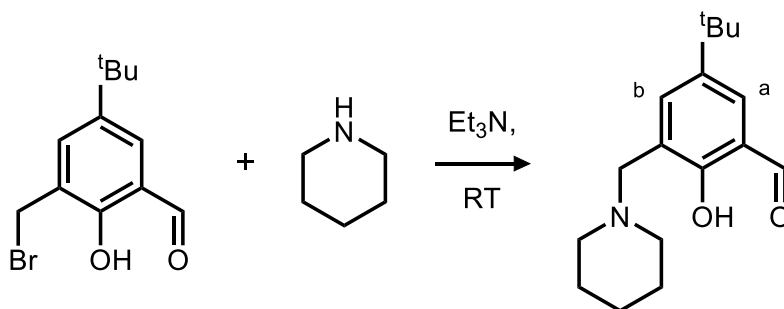


The compound **L3** was prepared from an adapted version of De Silva *et al.*<sup>35e</sup> A solution of  $\text{NH}_2\text{OH}\cdot\text{HCl}$  (0.29 g, 4.16 mmol, 1.0 eq.) in EtOH (50 mL) was neutralised with a solution of KOH (0.23 g, 4.16 mmol, 1.0 eq.) in EtOH (50 mL). The filtered solution was added slowly dropwise into a solution of **L3a** (1.60 g, 4.16 mmol, 1.0 eq.) in EtOH (50 mL). The resulting solution was stirred for 24 hours at RT. The light orange solution was concentrated *in vacuo* affording an oil, which was redissolved in  $\text{CHCl}_3$  (50 mL). This solution was washed with deionised  $\text{H}_2\text{O}$  (3 x 50 mL) and the combined organic layers dried over anhydrous  $\text{MgSO}_4$  and concentrated *in vacuo* affording **L3** as a yellow oil (1.60 g, 4.02 mmol, 96.7%).  $^1\text{H}$  NMR, (500 MHz,  $\text{CDCl}_3$ ):  $\delta$  8.45 (1H, s,  $\text{CH}=\text{N}$ ), 7.44 (1H, d,  $J = 2.5$  Hz, *b*), 7.35-7.27 (5H, m,  $\text{C}_6\text{H}_5\text{-CH}_2$ ), 7.17 (1H, d,  $J = 2.5$  Hz, *a*), 3.77 (2H, s,  $\text{C}_6\text{H}_5\text{-CH}_2$ ), 3.66 (2H, s,  $\text{Ar-CH}_2\text{-NBn}$ ), 3.33 (3H, s, *OMe*), 2.23 (2H, t,  $J = 7.2$  Hz,  $\text{NBn-CH}_2\text{-CH}_2$ ), 2.59 (2H, t,  $J = 7.2$  Hz,  $\text{CH}_2\text{-CH}_2\text{-COO}$ ), 1.29 (9H, s, *tBu*);  $^{13}\text{C}$  NMR (125.7 MHz,  $\text{CDCl}_3$ ):  $\delta$  172.5, 153.9, 149.0, 142.0, 136.9, 129.4, 128.5, 128.3, 127.6, 123.6, 122.7, 117.5, 58.1, 55.8, 51.8, 49.0, 34.1, 31.9, 31.4; IR:  $\bar{\nu} = 3397$  (O-H); 2955 (C-H); 1736 (C=O); 1626 (C=N); 1454 ( $-\text{CH}_2$ ); 1393 (*tBu*); 1363 (O-H); 1212 (C-O); 1114 (C-N);  $1027\text{ cm}^{-1}$  (C-O); MS:  $m/z$  (ESI) 399 [ $\text{M}+\text{H}$ ] $^+$ ; UV/Vis ( $\epsilon$ , L/mol cm) in MeOH: 315.0 (4135), 261.5 (10090), 214.5 (25835); elemental analysis calcd (%) for  $\text{C}_{23}\text{H}_{30}\text{N}_2\text{O}_4$ : C 69.15, H 7.82, N 7.01; found: C 68.77, H 7.65, N 6.99.



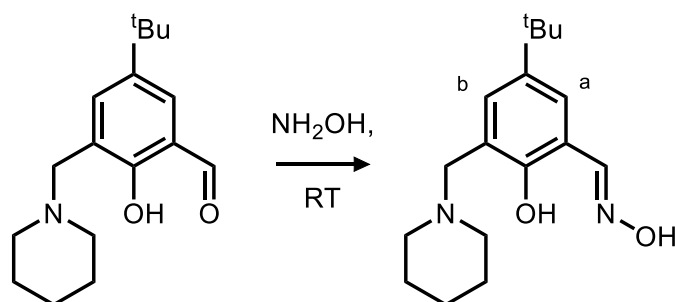
#### 4.2.5 Synthesis of L4

##### 5-*tert*-Butyl-3-(piperidinylmethyl)-2-hydroxybenzaldehyde (L4a)



The compound **L4a** was prepared from an adapted version of Stevens and Plieger.<sup>41</sup> Solutions of Piperidine (0.73 mL, 7.37 mmol, 1.0 eq.) and **2** (2.00 g, 7.37 mmol, 1.0 eq.), both in CHCl<sub>3</sub> (50 mL) were added dropwise to a stirred solution of Et<sub>3</sub>N (1.04 mL, 7.37 mmol, 1.0 eq.) in CHCl<sub>3</sub> (50 mL). The resulting bright orange solution was stirred for 24 hours at RT. The solution was washed with deionised H<sub>2</sub>O (3 x 60 mL), and the combined organic layers were dried over anhydrous MgSO<sub>4</sub> and concentrated *in vacuo* to afford **L4a** as an orange oil (1.98 g, 7.19 mmol, 97.7%). The <sup>1</sup>H NMR spectrum agreed with the literature values (500 MHz, CDCl<sub>3</sub>): δ 10.41 (1H, s, CH=O), 7.65 (1H, d, J = 2.6 Hz, *b*), 7.24 (1H, d, J = 2.6 Hz, *a*), 3.71 (2H, s, Ar-CH<sub>2</sub>-N), 2.55 (4H, s, N-CH<sub>2</sub>-CH<sub>2</sub>), 1.67 (4H, t, J = 5.3 Hz, N-CH<sub>2</sub>-CH<sub>2</sub>), 1.52 (2H, s, N-(CH<sub>2</sub>)<sub>2</sub>-CH<sub>2</sub>), 1.29 (9H, s, *t*Bu).

### 5-*tert*-Butyl-3-(piperidinylmethyl)-2-hydroxybenzaldehyde oxime (L4)



The compound **L4** was prepared from an adapted version of De Silva *et al.*<sup>35e</sup> A solution of  $\text{NH}_2\text{OH}\cdot\text{HCl}$  (0.25 g, 4.10 mmol, 1.0 eq.) in EtOH (50 mL) was neutralised with a solution of KOH (0.20 g, 4.10 mmol, 1.0 eq.) in EtOH (50 mL). The filtered solution was added slowly dropwise into a solution of **L4a** (1.00 g, 4.10 mmol, 1.0 eq.) in EtOH (50 mL). The resulting solution was stirred for 24 hours at RT. The light orange solution was concentrated *in vacuo* affording an oil, which was redissolved in  $\text{CHCl}_3$  (50 mL). This solution was washed with deionised  $\text{H}_2\text{O}$  (3 x 50 mL) and the combined organic layers dried over anhydrous  $\text{MgSO}_4$  and concentrated *in vacuo* affording **L4** as an orange oil (0.70 g, 2.41 mmol, 65.2%). The  $^1\text{H}$  NMR spectrum agreed with the literature values, (500 MHz,  $\text{CDCl}_3$ ):  $\delta$  8.47 (1H, s,  $\text{CH}=\text{N}$ ), 7.50 (1H, d,  $J = 2.1$  Hz, *b*), 7.15 (1H, d,  $J = 2.1$  Hz, *a*), 3.76 (2H, s, Ar- $\text{CH}_2$ -N), 2.61 (4H, s, N- $\text{CH}_2$ - $\text{CH}_2$ ), 1.70 (4H, t,  $J = 5.8$  Hz, N- $\text{CH}_2$ - $\text{CH}_2$ ), 1.53 (2H, s, N-( $\text{CH}_2$ )<sub>2</sub>- $\text{CH}_2$ ), 1.31 (9H, s, *tBu*).

## 4.3 Complexation Synthesis

### 4.3.1 [Cu(L1)<sub>2</sub>(BF<sub>4</sub>)<sub>2</sub>] (C1)

To **L1** (0.427 g, 1.460 mmol, 2.0 eq.) in MeOH (15 mL) was added Cu(BF<sub>4</sub>)<sub>2</sub>·6H<sub>2</sub>O (0.252 g, 0.730 mmol, 1.0 eq.) in MeOH (15 mL). The green solution was stirred at RT for 30 minutes. Isolation of the complex was achieved by the diffusion of Et<sub>2</sub>O into the reaction solution. Green platelet X-ray quality crystals were produced after three weeks. The crystals were crushed and dried prior to further analysis. Yield (0.537 g, 89.6%); IR:  $\bar{\nu}$  = 3123 (O-H); 2973 (C-H); 1560 (C=N); 1470 (C-H); 1219 (C-O); 1121 cm<sup>-1</sup> (C-N); 1020 (C-O); 952 (N-O); 866 (B-F) cm<sup>-1</sup>; MS: *m/z* (ESI) 733 [Cu(L1)<sub>2</sub>(BF<sub>4</sub>)<sub>2</sub>]<sup>+</sup>; UV/Vis ( $\epsilon$ , L/mol cm) in MeOH: 351.0 (7673), 268.5 (25471), 247.0 (33522), 229.5 (35408); Conductivity (MeOH):  $\lambda$  = 167 S cm<sup>2</sup> mol<sup>-1</sup>, a 1:1 electrolyte in the range 100–130 S cm<sup>2</sup> mol<sup>-1</sup>; elemental analysis calcd (%) for C<sub>32</sub>H<sub>46</sub>N<sub>4</sub>O<sub>6</sub>B<sub>2</sub>F<sub>8</sub>Cu·2MeOH·H<sub>2</sub>O: C 45.27, H 6.26, N 6.21; found: C 44.93, H 6.27, N 6.28. **Crystal Data** for C<sub>32</sub>H<sub>48</sub>B<sub>2</sub>CuF<sub>8</sub>N<sub>4</sub>O<sub>6</sub> (*M* = 821.90 g/mol): triclinic, space group *P* $\bar{1}$  (no. 2), *a* = 8.3510(6) Å, *b* = 10.8693(7) Å, *c* = 10.9418(8) Å,  $\alpha$  = 82.758(6)°,  $\beta$  = 69.225(5)°,  $\gamma$  = 79.053(6)°, *V* = 909.84(12) Å<sup>3</sup>, *Z* = 1, *T* = 123.0 K,  $\mu$ (CuK $\alpha$ ) = 1.644 mm<sup>-1</sup>, *D*<sub>calc</sub> = 1.500 g/cm<sup>3</sup>, 9153 reflections measured (8.302° ≤ 2 $\theta$  ≤ 130.146°), 3011 unique (*R*<sub>int</sub> = 0.0855, *R*<sub>sigma</sub> = 0.1113) which were used in all calculations. The final *R*<sub>1</sub> was 0.0762 (*I* > 2 $\sigma$ (*I*)) and *wR*<sub>2</sub> was 0.2467 (all data).

### 4.3.2 [Ni(L1-H)<sub>2</sub>] (C2)

To **L1** (0.545 g, 1.86 mmol, 2.0 eq.) in MeOH (15 mL) was added Ni(OAc)<sub>2</sub>·6H<sub>2</sub>O (0.231 g, 0.930 mmol, 1.0 eq.) in MeOH (15 mL) and pyridine (0.5 mL). The green solution was stirred at RT for 30 minutes. Isolation of the complex was achieved by the diffusion of Et<sub>2</sub>O into the reaction solution. Green prism shaped X-ray quality crystals were produced after three weeks. The crystals were crushed and dried prior to further analysis. Yield (0.435 g, 72.8%); IR:  $\bar{\nu}$  = 3056 (O-H); 2952 (C-H); 1562 (C=N); 1465 (C-H); 1222 (C-O); 1114 (C-N); 1033 (C-O) cm<sup>-1</sup>; MS: *m/z* (ESI) 641 [Ni(L1-H)<sub>2</sub>]<sup>+</sup>; UV/Vis ( $\epsilon$ , L/mol cm) in MeCN: 397.5 (4787), 312.5 (10446), 243.0 (36235); Conductivity (Acetone):  $\lambda$  = 0.519 S cm<sup>2</sup> mol<sup>-1</sup>,

non-electrolyte; elemental analysis calcd (%) for  $C_{32}H_{46}N_4O_6Ni$ : C 59.92, H 7.23, N 8.73; found: C 60.33, H 6.91, N 8.55. **Crystal Data** for  $C_{32}H_{46}N_4NiO_6$  ( $M=641.44$  g/mol): triclinic, space group  $P\bar{1}$  (no. 2),  $a = 6.1811(7)$  Å,  $b = 10.7083(14)$  Å,  $c = 13.2202(15)$  Å,  $\alpha = 80.688(8)^\circ$ ,  $\beta = 76.982(7)^\circ$ ,  $\gamma = 74.772(9)^\circ$ ,  $V = 817.69(17)$  Å<sup>3</sup>,  $Z = 1$ ,  $T = 396.15$  K,  $\mu(CuK\alpha) = 1.245$  mm<sup>-1</sup>,  $D_{calc} = 1.303$  g/cm<sup>3</sup>, 9911 reflections measured ( $6.904^\circ \leq 2\theta \leq 131.97^\circ$ ), 2777 unique ( $R_{int} = 0.0779$ ,  $R_{\sigma} = 0.1316$ ) which were used in all calculations. The final  $R_1$  was 0.0680 ( $I > 2\sigma(I)$ ) and  $wR_2$  was 0.2472 (all data).

#### 4.3.3 $[Mn(L4a)_2(NO_3)_2](NO_3)$ (C3)

To **L4** (0.454 g, 1.56 mmol, 1.0 eq.) in MeOH (10 mL) was added  $Mn(NO_3)_2 \cdot 4H_2O$  (0.412 g, 1.56 mmol, 1.0 eq.) in MeOH (10 mL),  $NH_4OAc$  (0.122 g, 1.56 mmol, 1.0 eq.) in MeOH (10 mL), and pyridine (0.5 mL). The brown/green solution was stirred at RT for 30 minutes. Isolation of the complex was achieved by the diffusion of  $Et_2O$  into the reaction solution. Dark green platelet shaped X-ray quality crystals were produced after two weeks. The crystals were crushed and dried prior to further analysis. Yield (0.152 g, 12.3%); IR:  $\bar{\nu} = 3429$  (N-H); 2957 (C-H); 1671 (C=O); 1457 (C-H); 1409 ( $NO_2$ ); 1295 (N-O); 1221 (C-N); 1030 cm<sup>-1</sup> (C-O); MS:  $m/z$  (ESI) 585  $[Mn(L4a)_2(NO_3)]Na^+$ ; UV/Vis ( $\epsilon$ , L/mol cm) in MeOH: 369.5 (8926), 258.0 (34793); Conductivity (MeOH):  $\lambda = 145$  S cm<sup>2</sup> mol<sup>-1</sup>, a 1:1 electrolyte in the range 100-130 S cm<sup>2</sup> mol<sup>-1</sup>. **Crystal Data** for  $C_{35}H_{56}MnN_5O_{14}$  ( $M=825.78$  g/mol): monoclinic, space group  $P2/c$  (no. 13),  $a = 15.31(3)$  Å,  $b = 6.112(3)$  Å,  $c = 22.18(2)$  Å,  $\beta = 106.65(15)^\circ$ ,  $V = 1988(5)$  Å<sup>3</sup>,  $Z = 2$ ,  $T = 100$  K,  $\mu(MoK\alpha) = 0.403$  mm<sup>-1</sup>,  $D_{calc} = 1.379$  g/cm<sup>3</sup>, 5224 reflections measured ( $6.936^\circ \leq 2\theta \leq 50.218^\circ$ ), 2268 unique ( $R_{int} = 0.2991$ ,  $R_{\sigma} = 0.5456$ ) which were used in all calculations. The final  $R_1$  was 0.1286 ( $I > 2\sigma(I)$ ) and  $wR_2$  was 0.2782 (all data).

#### 4.3.4 $[Cu_2(L3')Cl_2]$ (C4)

To **L3** (0.338 g, 0.85 mmol, 1.0 eq.) in MeOH (10 mL) was added  $Cu(BF_4)_2 \cdot 6H_2O$  (0.293 g, 0.85 mmol, 1.0 eq.) and  $NH_4Cl$  (0.0450 g, 0.85 mmol, 1.0 eq.), both in MeOH (10 mL). The dark green solution was stirred at RT for 30 minutes. Isolation of the complex was achieved

by the diffusion of Et<sub>2</sub>O into the reaction solution. Green platelet shaped X-ray quality crystals were produced after two weeks. The crystals were crushed and dried prior to further analysis. Yield (0.230 g, 24%); <sup>19</sup>F NMR (30 MHz, CDCl<sub>3</sub>, Trifluoroethanol): δ -150.4; IR:  $\bar{\nu}$  = 3324 (N-H); 2965 (C-H); 1738 (C=O); 1565 (C=N); 1462 (C-H); 1267 (C-O); 1044 (C-N) cm<sup>-1</sup>; MS: *m/z* (ESI) 1001 [Cu<sub>2</sub>(L3')<sub>2</sub>Cl<sub>2</sub>]<sup>+</sup>; UV/Vis ( $\epsilon$ , L/mol cm) in MeOH: 348.0 (11991), 298.5 (12068), 207.0 (197674); Conductivity (MeOH):  $\lambda$  = 222 S cm<sup>2</sup> mol<sup>-1</sup>, a 2:1 electrolyte in the range 210-250 S cm<sup>2</sup> mol<sup>-1</sup>; **Crystal Data** for C<sub>48</sub>H<sub>64</sub>N<sub>4</sub>O<sub>10</sub>Cu<sub>2</sub>Cl<sub>2</sub>B<sub>2</sub>F<sub>4</sub> (*M* = 1152.63 g/mol): triclinic, space group *P* $\bar{1}$  (no. 2), *a* = 10.0416(13) Å, *b* = 10.2816(14) Å, *c* = 13.6830(15) Å,  $\alpha$  = 104.670(7)°,  $\beta$  = 95.931(7)°,  $\gamma$  = 110.168(8)°, *V* = 1254.2(3) Å<sup>3</sup>, *Z* = 1, *T* = 103 K,  $\mu$ (CuK $\alpha$ ) = 2.678 mm<sup>-1</sup>, *D*<sub>calc</sub> = 1.526 g/cm<sup>3</sup>, 11410 reflections measured (6.83° ≤ 2 $\theta$  ≤ 117.818°), 3489 unique (*R*<sub>int</sub> = 0.1932, *R*<sub>sigma</sub> = 0.4606) which were used in all calculations. The final *R*<sub>1</sub> was 0.0838 (*I* > 2 $\sigma$ (*I*)) and *wR*<sub>2</sub> was 0.2320 (all data).

#### 4.3.5 [Fe<sub>3</sub>O(L4-H)<sub>3</sub>(OAc)<sub>3</sub>]<sup>-</sup> (C5)

To **L4** (0.498 g, 1.72 mmol, 1.0 eq.) in MeOH (10 mL) was added Fe(BF<sub>4</sub>)<sub>2</sub>·6H<sub>2</sub>O (0.579 g, 1.72 mmol, 1.0 eq.), and NH<sub>4</sub>OAc (0.132 g, 1.72 mmol, 1.0 eq), both in MeOH (15 mL) and pyridine (1 mL). The dark maroon solution was stirred at RT for 30 minutes. Isolation of the complex was achieved by the diffusion of Et<sub>2</sub>O into the reaction solution. Red platelet shaped X-ray quality crystals were produced after three weeks. The crystals were dried and crushed prior to further analysis. Yield (0.289 g, 13.7%); IR:  $\bar{\nu}$  = 3333 (N-H); 2956 (C-H); 1554 (C=N); 1433 (C-H); 1220 (C-O); 1028 (C-N) cm<sup>-1</sup>; UV/Vis ( $\epsilon$ , L/mol cm) in MeOH: 317.0 (15185), 254.0 (28888), 221.0 (35679); Conductivity (MeOH):  $\lambda$  = 389 S cm<sup>2</sup> mol<sup>-1</sup>, a 3:1 electrolyte in the range 340-380 S cm<sup>2</sup> mol<sup>-1</sup>; **Crystal Data** for C<sub>57</sub>H<sub>84</sub>N<sub>6</sub>O<sub>13</sub>Fe<sub>3</sub> (*M* = 1228.85 g/mol): triclinic, space group *P* $\bar{1}$  (no. 2), *a* = 14.683(4) Å, *b* = 15.057(4) Å, *c* = 18.384(3) Å,  $\alpha$  = 68.134(15)°,  $\beta$  = 77.841(16)°,  $\gamma$  = 74.662(16)°, *V* = 3609.1(15) Å<sup>3</sup>, *Z* = 2, *T* = 123 K,  $\mu$ (CuK $\alpha$ ) = 5.218 mm<sup>-1</sup>, *D*<sub>calc</sub> = 1.131 g/cm<sup>3</sup>, 37663 reflections measured (5.22° ≤ 2 $\theta$  ≤ 144.232°), 12283 unique (*R*<sub>int</sub> = 0.3197, *R*<sub>sigma</sub> = 1.1440) which were used in all calculations. The final *R*<sub>1</sub> was 0.1356 (*I* > 2 $\sigma$ (*I*)) and *wR*<sub>2</sub> was 0.3993 (all data).

#### 4.3.6 $[Mn_3O(L4-H)_2(L4-2H)(OAc)_3]$ (C6)

To **L4** (0.420 g, 1.45 mmol, 1.0 eq.) in MeOH (15 mL) was added  $Mn(OAc)_3 \cdot 2H_2O$  (0.388 g, 1.45 mmol, 1.0 eq.) in MeOH (15 mL) and pyridine (0.5 mL). The dark green solution was stirred at RT for 30 minutes. Isolation of the complex was achieved by the diffusion of  $Et_2O$  into the reaction solution. Green platelet shaped X-ray quality crystals were produced after three weeks. The crystals were crushed and dried prior to further analysis. Yield (0.316 g, 19.1%); IR:  $\bar{\nu}$  = 3422 (N-H); 2955 (C-H); 1575 (C=N); 1407 (C-H); 1219 (C-O); 1038 (C-N); 937 (N-O)  $cm^{-1}$ ; UV/Vis ( $\epsilon$ , L/mol cm) in MeOH: 377.5 (12615), 304.0 (25077), 204.0 (47706); Conductivity (MeOH):  $\lambda$  = 132 S  $cm^2 mol^{-1}$ , a 1:1 electrolyte in the range 100-130 S  $cm^2 mol^{-1}$ ; **Crystal Data** for  $C_{57}H_{81}N_6O_{13}Mn_3$  ( $M=1223.09$  g/mol): triclinic, space group  $P\bar{1}$  (no. 2),  $a = 14.7233(5)$  Å,  $b = 15.7675(5)$  Å,  $c = 16.5710(12)$  Å,  $\alpha = 93.615(7)^\circ$ ,  $\beta = 112.078(8)^\circ$ ,  $\gamma = 107.459(8)^\circ$ ,  $V = 3332.7(4)$  Å<sup>3</sup>,  $Z = 2$ ,  $T = 123$  K,  $\mu(CuK\alpha) = 5.039$  mm<sup>-1</sup>,  $D_{calc} = 1.219$  g/cm<sup>3</sup>, 33045 reflections measured ( $9.988^\circ \leq 2\theta \leq 130.18^\circ$ ), 10463 unique ( $R_{int} = 0.0977$ ,  $R_{\sigma} = 0.2723$ ) which were used in all calculations. The final  $R_1$  was 0.1136 ( $I > 2\sigma(I)$ ) and  $wR_2$  was 0.3751 (all data).

#### 4.3.7 $[Fe_4(L3)_2(OMe)_6(OH)_6]$ (C7)

To **L3** (0.230 g, 0.577 mmol, 6.0 eq.) in MeOH (10 mL) was added  $Dy(NO_3)_3 \cdot 6H_2O$  (0.044 g, 0.096 mmol, 1.0 eq.) in MeOH (5 mL), and  $Et_3N$  (1 mL). The dark yellow mixture was refluxed for two hours, then cooled to RT. To the reaction mixture,  $Fe(BF_4)_2 \cdot 6H_2O$  (0.194 g, 0.575 mmol, 6.0 eq.) in MeOH (15 mL) and pyridine (1 mL) were added, and then the maroon solution was stirred at RT for 30 minutes. Isolation of the complex was achieved by concentrating the solution *in vacuo*, redissolving in 1:1 MeOH : MeCN and then diffusing  $Et_2O$  into the solution. Red platelet shaped X-ray quality crystals were produced after 4 weeks. The crystals were crushed and dried prior to further analysis. Yield (0.064 g, 8.51%); IR:  $\bar{\nu}$  = 3269 (N-H); 3043 (O-H); 2956 (C-H); 2253 (C≡N); 1562 (C=N); 1469 (CH<sub>2</sub>); 1220 (C-O); 1054 (C-N); 946 (N-O)  $cm^{-1}$ . **Crystal Data** for  $C_{52}H_{84}Fe_4N_4O_{20}$  ( $M=1308.63$  g/mol): monoclinic, space group  $P2_1/n$  (no. 14),  $a = 12.6467(7)$  Å,  $b = 13.4352(6)$  Å,  $c = 19.5907(14)$  Å,  $\beta = 96.679(7)^\circ$ ,  $V = 3306.1(3)$  Å<sup>3</sup>,  $Z = 2$ ,  $T = 133$  K,  $\mu(CuK\alpha) = 7.471$  mm<sup>-1</sup>,  $D_{calc} = 1.315$  g/cm<sup>3</sup>, 29690 reflections measured

( $7.922^\circ \leq 2\theta \leq 144.184^\circ$ ), 6353 unique ( $R_{\text{int}} = 0.1307$ ,  $R_{\text{sigma}} = 0.2056$ ) which were used in all calculations. The final  $R_1$  was 0.0844 ( $I > 2\sigma(I)$ ) and  $wR_2$  was 0.2412 (all data).

#### 4.3.8 $[Ni_4(L2-H)_2(OAc)_2(OMe)_2Cl_2](Et_2O)_3$ (C8)

To **L2** (0.421 g, 1.06 mmol, 1.0 eq.) in MeOH (10 mL) was added Ni(OAc)<sub>2</sub>·4H<sub>2</sub>O (0.526 g, 2.11 mmol, 2.0 eq.) and NH<sub>4</sub>Cl (0.0565 g, 1.06 mmol, 1.0 eq.), both in MeOH (10 mL). The green solution was stirred at RT for 30 minutes. Isolation of the complex was achieved by the diffusion of Et<sub>2</sub>O into the reaction solution. Green prism shaped X-ray quality crystals were produced after 8 weeks. The crystals were crushed and dried prior to further analysis. Yield (0.169 g, 12.4%); IR:  $\bar{\nu} = 3249$  (O-H); 2953 (C-H); 1575 (C=N); 1486 (C=C); 1463 (CH<sub>2</sub>); 1414 (N-O); 1219 (C-O); 1030 (C-N) cm<sup>-1</sup>; UV/Vis ( $\epsilon$ , L/mol cm) in MeOH: 344.5 (12500), 267.0 (101146); Conductivity (DCM):  $\lambda = 2.00$  S cm<sup>2</sup> mol<sup>-1</sup>, non-electrolyte; elemental analysis calcd (%) for C<sub>39</sub>H<sub>68</sub>N<sub>4</sub>O<sub>14</sub>Cl<sub>2</sub>Ni<sub>4</sub>·Et<sub>2</sub>O·2H<sub>2</sub>O: C 42.45, H 6.64, N 4.50; found: C 42.07, H 6.24, N 4.51. **Crystal Data** for C<sub>52</sub>H<sub>94</sub>Cl<sub>2</sub>N<sub>4</sub>Ni<sub>4</sub>O<sub>17</sub> ( $M = 1353.05$  g/mol): monoclinic, space group  $P 2_1/c$  (no. 14),  $a = 13.3361(6)$  Å,  $b = 13.8643(7)$  Å,  $c = 17.3381(12)$  Å,  $\beta = 90^\circ$ ,  $V = 3205.7(3)$  Å<sup>3</sup>,  $Z = 2$ ,  $T = 123$  K,  $\mu(\text{CuK}\alpha) = 2.628$  mm<sup>-1</sup>,  $D_{\text{calc}} = 1.402$  g/cm<sup>3</sup>, 18623 reflections measured ( $12.77^\circ \leq 2\theta \leq 130.178^\circ$ ), 5289 unique ( $R_{\text{int}} = 0.0908$ ,  $R_{\text{sigma}} = 0.0785$ ) which were used in all calculations. The final  $R_1$  was 0.0690 ( $I > 2\sigma(I)$ ) and  $wR_2$  was 0.2162 (all data).

#### 4.3.9 $[Ni_4(L3-H)_2(OAc)_2(OMe)_2Cl_2](MeOH)_2$ (C9)

To **L3** (0.304 g, 0.76 mmol, 1.0 eq.) in MeOH (10 mL) was added Ni(OAc)<sub>2</sub>·4H<sub>2</sub>O (0.467 g, 1.88 mmol, 2.0 eq.) and NH<sub>4</sub>Cl (0.0409 g, 0.76 mmol, 1.0 eq.), both in MeOH (10 mL). The green solution was stirred at RT for 30 minutes. Isolation of the complex was achieved by the diffusion of Et<sub>2</sub>O into the reaction solution. Green prism shaped X-ray quality crystals were produced after three weeks. The crystals were crushed and dried prior to further analysis. Yield (0.204 g, 20.8%); IR:  $\bar{\nu} = 3258$  (O-H); 2959 (C-H); 1699 (C=O); 1570 (C=N); 1489 (C=C); 1469 (CH<sub>2</sub>); 1417 (N-O); 1235 (C-O); 1030 (C-N) cm<sup>-1</sup>; UV/Vis ( $\epsilon$ , L/mol cm) in MeOH: 349.5 (8888); Conductivity (DCM):  $\lambda = 1.18$  S cm<sup>2</sup> mol<sup>-1</sup>, non-electrolyte;

Conductivity (MeOH):  $\lambda = 122 \text{ S cm}^2 \text{ mol}^{-1}$ , a 1:1 electrolyte in the range 100-130  $\text{S cm}^2 \text{ mol}^{-1}$ ; **Crystal Data** for  $\text{C}_{54}\text{H}_{78}\text{N}_4\text{O}_{16}\text{Cl}_2\text{Ni}_4$  ( $M = 1344.94 \text{ g/mol}$ ): monoclinic, space group  $C 2/c$  (no. 15),  $a = 28.3807(13) \text{ \AA}$ ,  $b = 11.6847(4) \text{ \AA}$ ,  $c = 17.6764(16) \text{ \AA}$ ,  $\beta = 99.829(16)^\circ$ ,  $V = 5775.8(7) \text{ \AA}^3$ ,  $Z = 4$ ,  $T = 123 \text{ K}$ ,  $\mu(\text{CuK}\alpha) = 2.907 \text{ mm}^{-1}$ ,  $D_{\text{calc}} = 1.547 \text{ g/cm}^3$ , 21855 reflections measured ( $9.358^\circ \leq 2\theta \leq 130.09^\circ$ ), 4912 unique ( $R_{\text{int}} = 0.2836$ ,  $R_{\text{sigma}} = 0.6238$ ) which were used in all calculations. The final  $R_1$  was 0.1138 ( $I > 2\sigma(I)$ ) and  $wR_2$  was 0.3451 (all data).



## 5.0 Conclusions and Future Work

The conclusion of this research project resulted in the synthesis of four ligands, two of which were previously unknown (**L2** and **L3**). The ligands were designed to incorporate greater flexibility, a greater number of binding sites, and produce complexes with higher nuclearities. Through complexation and crystallisation, nine new *3d* ion complexes were produced and characterised, with four distinct topologies: mononuclear, dinuclear, trinuclear triangles, and tetranuclear defective dicubanes.

Three new mononuclear complexes (**C1-C3**) were synthesised during the project. **C1**, is an octahedral Cu(II) complex, which utilises the ligand, **L1**, and has weakly coordinated BF<sub>4</sub><sup>-</sup> anions completing the octahedral coordination geometry. The complex, **C2**, is square planar Ni(II), and utilises the same ligand as **C1**. Magnetic measurements on **C1** ( $\chi_M T$ , 0.349 cm<sup>3</sup> K mol<sup>-1</sup> and  $\mu_{eff}$ , 1.67  $\mu_B$ ) and **C2** ( $\chi_M T$ , -0.0586 cm<sup>3</sup> K mol<sup>-1</sup> and  $\mu_{eff}$ , 0.242  $\mu_B$ ) were as expected for octahedral Cu(II) and square planar Ni(II) ions. The complex **C3**, has an octahedral Mn(III) ion, coordinated by two **L4a** molecules, and axial NO<sub>3</sub><sup>-</sup> anions. The synthesis of **C3** was unexpected, as the ligand **L4** underwent a hydrolytic reaction to produce the precursor ligand, **L4a**. The cause for this was suggested to be free Mn(II) ions in solution. The magnetic moment measurement of **C3** was found to be  $\chi_M T$ , 3.95 cm<sup>3</sup> K mol<sup>-1</sup> and  $\mu_{eff}$ , 5.59  $\mu_B$ .

**C4**, a dinuclear Cu(II) complex provided a new unique route for ligand design. The ligand, **L3'**, a derivative of **L3**, was formed by a *in situ* condensation reaction. The result of this reaction was the addition of a difluoromethoxy borane functionality to the oximic oxygen atom. Magnetic measurements on **C4** revealed that the two Cu(II) ions had extremely weak antiferromagnetic exchange between them, resulting in a  $\chi_M T$  value of 0.91 cm<sup>3</sup> K mol<sup>-1</sup>.

Complexes, **C5** and **C6** are trinuclear Fe(III) and Mn(III) structures respectively, with triangular topologies. The triangular structures utilise the ligand **L4**, with the octahedral metal ion geometries completed by  $\mu_2$ -OAc anions. Key structural differences between the two complexes, are the coordination geometry of the  $\mu_2$ -OAc anions; for **C5**, all of the OAc<sup>-</sup> anions have a *fac* coordination geometry, whereas for **C6**, they coordinate in a *mer-mer-fac* fashion. **C6** is the first known H<sub>2</sub>Sao based Mn(III) triangle with  $\mu_2$ -OAc anions coordinated

in such a fashion. Magnetic measurements revealed both **C5** and **C6** have antiferromagnetically coupled exchange pathways present between the metal centres.

The fourth type of complex synthesised, was tetranuclear Ni(II) complexes with defective dicubane topologies (**C8** and **C9**). The metallic core of both complexes resemble each other in terms of coordination, however, small differences in the angle of the bridging groups between Ni(II) ions result from subtle differences in the secondary amine of the H<sub>2</sub>Sao based ligand (**L2** and **L3**, respectively for **C8** and **C9**). Magnetic measurements of both complexes were performed and it was found that the subtle differences (ether versus ester functional groups) resulted in a change from ferromagnetic (**C8**) to antiferromagnetic (**C9**) coupling between the metal centres.

With the results obtained from this research, the next steps would be to look into how modifications on the existing complexes, and/or the ligands utilised, could provide a platform for 4*f* ion coordination. The Ni(II) defective dicubanes are appealing starting points for exploring how structural modifications, whether small or large modifications, can affect and alter the magnetic properties of a complex, or a series of complexes.

## References

1. Housecroft, C. E; Sharpe, A. G., *Inorganic Chemistry*. 4th Ed.; Pearson: Harlow, England; 2012; 1215 pgs.
2. Vulfson, S. G., *Molecular Magnetochemistry*. Gordon and Breach Science Publishers: Amsterdam, Netherlands; 1998; 220 pgs.
3. Feltham, H. L. C.; Brooker, S., Review of purely 4*f* and mixed-metal *nd-4f* single-molecule magnets containing only one lanthanide ion. *Coord. Chem. Rev.* **2014**, *276*, 1-33.
4. Shriver, D. F; Atkins, P. W., *Inorganic Chemistry*. 3rd Ed.; Oxford University Press: Oxford, England; 1999; 763 pgs.
5. Weihe, H.; Gudel, H. U., Quantitative interpretation of the Goodenough-Kanamori rules: A critical analysis. *Inorg. Chem.* **1997**, *36*, 3632-3639.
6. Kanamori, J., Superexchange interaction and symmetry properties of electron orbitals. *J. Phys. Chem. Solids* **1959**, *10*(2), 87-98.
7. (a) Das, C.; Upadhyay, A.; Shanmugam, M., Influence of radicals on magnetization relaxation dynamics of pseudo-octahedral lanthanide iminopyridyl complexes. *Inorg. Chem.* **2018**, *57*(15), 9002-9011; (b) Ding, Y.-S.; Chilton, N. F.; Winpenny, R. E.; Zheng, Y-Z., On approaching the limit of molecular magnetic anisotropy: A near-perfect pentagonal bipyramidal dysprosium(III) single-molecule magnet. *Angew. Chem. Int. Ed.* **2016**, *55*, 16071-16074; (c) Goodwin, C. A. P.; Ortu, F.; Reta, D.; Chilton, N. F.; Mills, D. P., Molecular magnetic hysteresis at 60 kelvin in dysprosocenium. *Nature* **2017**, *548*(7668), 439-442; (d) Guo, F. S. Day, B. M.; Chen, Y. C.; Tong, M. L.; Mansikkamaki, A.; Layfield, R. A., Magnetic hysteresis up to 80 kelvin in a dysprosium metallocene single-molecule magnet. *Science* **2018**, *362*, 1400-1403; (e) Karotsis, G.; Teat, S. J.; Wernsdorfer, W.; Piligkos, S.; Dalgarno, S. J.; Brechin, E. K., Calix[4]arene-based single-molecule magnets. *Angew. Chem. Int. Ed. Engl.* **2009**, *48*(44), 8285-8288; (f) Ruiz-Molina, D. Christou, G.; Hendrickson, D. N., Single-molecule magnets. *Mol. Cryst. Liq. Cryst. Sci. Technol., Sect. A* **2000**, *343*, 17-27; (g) Han, T.; Shi, W.; Niu, Z.; Na, B.; Cheng, P., Magnetic blocking from exchange interactions: Slow relaxation of the magnetization and hysteresis loop observed in a dysprosium-nitronyl nitroxide chain compound with an antiferromagnetic ground state. *Chem.* **2013**, *19*(3), 994-1001; (h) Milios, C. J.; Piligkos, S.; Brechin, E. K., Ground state spin-switching via targeted structural distortion: Twisted single-molecule magnets from derivatised salicylaldoximes. *Dalton Trans.* **2008**, (14), 1809-1817.
8. (a) Bogani, L.; Wernsdorfer, W., Molecular spintronics using single-molecule magnets. *Nat. Mat.* **2008**, *7*, 179-186; (b) Cirera, B.; Matarrubia, J.; Kaposi, T.; Gimenez-Agullo, N.; Paszkiewicz, M.; Klappenberger, F.; Otero, R.; Gallego, J. M.;

- Ballester, P.; Barth, J. V.; Miranda, R.; Galan-Mascaros, J. R.; Auwarter, W.; Ecija, D., Preservation of electronic properties of double-decker complexes on metallic supports. *Phys. Chem. Chem. Phys.* **2017**, *19*(12), 8282-8287; (c) Holynska, M.; Premuzic, D.; Jeon, L-R.; Wernsdorfer, W.; Clerac, R.; Dehnen, S., [Mn<sup>III</sup><sub>6</sub>O<sub>3</sub>Ln<sub>2</sub>] single-molecule magnets: Increasing the energy barrier above 100 K. *Chem.* **2011**, *17*(35), 9605-9610; (d) Kim, J.; Han, S.; Lim, J. M.; Choi, K-Y.; Nojiri, H.; Suh, B. J., Single-molecule magnet: Heterodinuclear cyano-bridged cubic cluster [(Tp)<sub>8</sub>Fe<sub>4</sub>Ni<sub>4</sub>(CN)<sub>12</sub>] (Tp=hydrotris(1-pyrazolyl)borate). *Inorg. Chim. Acta* **2007**, *360*(8), 2647-2652; (e) Leuenberger, M. N.; Loss, D., Quantum computing in molecular magnets. *Nature* **2001**, *410*, 789-793; (f) Vignesh, K. R.; Langley, S. K.; Murray, K. S.; Rajaraman, G., Exploring the influence of diamagnetic ions on the mechanism of magnetization relaxation in {Co(III)<sub>2</sub>Ln(III)<sub>2</sub>} (Ln = Dy, Tb, Ho) "butterfly" complexes. *Inorg. Chem.* **2017**, *56*(5), 2518-2532; (g) Tsukerblat, B.; Pali, A.; Clemente-Juan, J. M.; Coronado, E., Jahn-Teller effect in molecular electronics: Quantum cellular automata. *J. Phys.: Conference Series* **2017**, *833*.
9. (a) Benelli, C.; Gatteschi, D., *Introduction to molecular magnetism: From transition metals to lanthanides*. Wiley-VCH: Weinheim, Germany; 2015; 450 pgs; (b) Christou, G., Single-molecule magnets: A molecular approach to nanoscale magnetic materials. *Polyhedron* **2005**, *24*, 2065-2075; (c) Gatteschi, D.; Sessoli, R., Quantum tunneling of magnetization and related phenomena in molecular materials. *Angew. Chem. Int. Ed.* **2003**, *42*, 268-297; (d) Vignesh, K. R.; Langley, S. K.; Moubaraki, B.; Murray, K. S.; Rajaraman, G., Understanding the mechanism of magnetic relaxation in pentanuclear {Mn(IV)Mn(III)<sub>2</sub>Ln(III)<sub>2</sub>} single-molecule magnets. *Inorg. Chem.* **2018**, *57*(3), 1158-1170; (e) Atkins, P.; Overton, T.; Rourke, J.; Weller, M.; Armstrong, F., *Shriver and Atkins' Inorg. Chem.* 4th Ed.; Oxford University Press: Oxford, England; 2006; 822 pgs.
10. (a) Lopez-Ruiz, R.; Almeida, P. T.; Vaz, M. G. F.; Novak, M. A.; Beron, F.; Pirota, K. R., A stochastic model for magnetic dynamics in single-molecule magnets. *J. Magn. Magn. Mater.* **2016**, *403*, 188-192; (b) Piquer, L. R.; Sanudo, E. C., Heterometallic 3d-4f single-molecule magnets. *Dalton Trans.* **2015**, *44*(19), 8771-8780; (c) Atanasov, M.; Aravena, D.; Suturina, E.; Bill, E.; Maganas, D.; Neese, F., First principles approach to the electronic structure, magnetic anisotropy and spin relaxation in mononuclear 3d-transition metal single molecule magnets. *Coord. Chem. Rev.* **2015**, *289-290*, 177-214.
11. (a) Bao, D-X.; Xiang, S.; Wang, J.; Li, Y-C.; Zhao, X-Q., Review: Single-molecule magnets based on pyridine alcohol ligands. *J. Coord. Chem.* **2016**, *69*(21), 3131-3147; (b) Escuer, A.; Mayans, J.; Font-Bardia, M.; Di Bari, L.; Górecki, M., Trinuclear complexes derived from R/S schiff bases - chiral single-molecule magnets. *Eur. J. Inorg. Chem.* **2017**, (6), 991-998; (c) Fang, X.; McCallum, K.; Pratt, H. D., III; Anderson, T. M.; Dennis, K.; Luban, M., A co-crystal of polyoxometalates exhibiting single-molecule magnet behavior: The structural origin of a large magnetic

- anisotropy. *Dalton Trans.* **2012**, 41(33), 9867-9870; (d) Vignesh, K. R.; Langley, S. K.; Gartshore, C. J.; Moubaraki, B.; Murray, K. S.; Rajaraman, G., What controls the magnetic exchange and anisotropy in a family of tetranuclear {Mn<sub>2</sub>(II)Mn<sub>2</sub>(III)} single-molecule magnets? *Inorg. Chem.* **2017**, 56(4), 1932-1949; (e) Halcrow, M. A., Jahn-Teller distortions in transition metal compounds, and their importance in functional molecular and inorganic materials. *Chem. Soc. Rev.* **2013**, 42(4), 1784-1795.
12. (a) Als-Nielsen, J.; McMorrow, D., *Elements of modern X-ray physics*. Wiley: Chichester, England; 2001; 336 pgs; (b) Cullity, B. D., *Elements of X-ray diffraction*. 2nd Ed.; Addison-Wesley Publishing Company Inc: Canada; 1978; 528 pgs; (c) Clegg, W., *Crystal structure determination*. Oxford University Press Inc., New York: United States; 1998; 84 pgs.
  13. (a) Gallop, J.; Hao, L., Nanoscale superconducting quantum interference devices add another dimension. *ACS Nano* **2016**, 10(9), 8128-8132; (b) Carlin, R. L., *Magnetochemistry*. 1st Ed.; Springer-Verlag: New York; 1986; 328 pgs.
  14. (a) Levenson-Falk, E. M.; Antler, N.; Siddiqi, I., Dispersive nanoSQUID magnetometry. *Supercond. Sci. Technol.* **2016**, 29(11), 11 pgs; (b) Sawicki, M.; Stefanowicz, W., Sensitive SQUID magnetometry for studying nano-magnetism. *Semicond. Sci. Technol.* **2011**, 26(6), 16 pgs; (c) Wernsdorfer, W., From micro- to nano-SQUIDs: applications to nanomagnetism. *Supercond. Sci. Technol.* **2009**, 22(6), 13 pgs.
  15. (a) Mibu, K.; Tanaka, M.; Hamaya, K., Mössbauer analysis. In *heusler alloys*, Springer International Publishing: Switzerland, 2016; p341-351; (b) Nakashima, S., Chemical information revealed by Mössbauer spectroscopy and DFT calculations. *Hyperfine Interactions.* **2017**, 238(1), 10 pgs; (c) Dyar, M. D.; Agresti, D. G.; Schaefer, M. W.; Grant, C. A.; Sklute, E. C., Mössbauer spectroscopy of earth and planetary materials. *Annu. Rev. Earth Planet. Sci.* **2006**, 34, 83-125.
  16. Walker, L. R.; Wertheim, G. K.; Jaccarino, V., Interpretation of the <sup>57</sup>Fe isomer shift. *Phys. Rev. Lett.* **1961**, 6(3), 98-101.
  17. Fultz, B., Mössbauer spectroscopy. In *characterization of materials*, Kaufmann, E., Editor. John Wiley: New York; 2011; 22 pgs.
  18. (a) Cox, E. G.; Pinkard, F. W.; Wardlaw, W.; Webster, K. C., The planar configuration for quadricovalent nickel, palladium, and platinum. *J. Chem. Soc.* **1935**, 459; (b) Ephraim, F., Über ein neues Reagens zur qualitativen and quantitativen Bestimmung des Kupfers. *Chem. Ber.* **1930**, 63, 1928-1930; (c) Jarski, M. A.; Lingafelter, E. C., The crystal structure of bis(salicylaldoximato)copper(II). *Acta. Cryst.* **1964**, 17, 1109-1112.
  19. (a) Bates, G. W.; Davidson, J. E.; Forgan, R. S.; Gale, P. A.; Henderson, D. K.; King, M. G.; Light, M. E.; Moore, S. J.; Tasker, P. A.; Tong, C. C., A dual host approach to NiSO<sub>4</sub> extraction. *Supramol. Chem.* **2012**, 24(2), 117-126; (b) Forgan, R. S.; Davidson, J. E.; Fabbiani, F. P.; Galbraith, S. G.; Henderson, D. K.; Moggach, S. A.; Parsons, S.; Tasker, P. A.; White, F. J., Cation and anion selectivity of zwitterionic salicylaldoxime metal

- salt extractants. *Dalton Trans.* **2010**, 39(7), 1763-1770; (c) Kolhe, N. H.; Jadhav, S. S.; Shaikh, S. H.; Takate, S. J.; Aware, D. V., Nanocrystalline mixed ligand complexes of Cu(II), Ni(II), Co(II) with N, O donor ligands: Synthesis, characterization, and antimicrobial activity. *Orient. J. Chem.* **2016**, 32(6), 2999-3013; (d) Zhu, Z-X.; Cai, L-Z.; Deng, X-W.; Zhou, Y-L.; Yao, M-X., Synthesis, structures and magnetism of heterotrimetallic Ni-Cu-Ln complexes based on a dicompartmental imine-oxime ligand. *New J. Chem.* **2017**, 41(19), 11097-11103; (e) Buhl, M.; Ashbrook, S. E.; Dawson, D. M.; Doyle, R. A.; Hrobarik, P.; Kaupp, M.; Smellie, I. A., Paramagnetic NMR of phenolic oxime copper complexes: A joint experimental and density functional study. *Chemistry* **2016**, 22(43), 15328-15339.
20. Forgan, R. S.; Davidson, J. E.; Galbraith, S. G.; Henderson, D. K.; Parsons, S.; Tasker, P. A.; White, F. J., Transport of metal salts by zwitterionic ligands; simple but highly efficient salicylaldoxime extractants. *Chem. Commun. (Camb)* **2008**, (34), 4049-4051.
  21. Coxall, R. A.; Lindloy, L. F.; Miller, H. A.; Parkin, A.; Parsons, S.; Tasker, P. A.; White, D. J., Solvent extraction of metal sulfates by zwitterionic forms of ditopic ligands. *Dalton Trans.* **2003**, 55-64.
  22. Liu, K.; Shi, W.; Cheng, P., Toward heterometallic single-molecule magnets: Synthetic strategy, structures and properties of 3d-4f discrete complexes. *Coord. Chem. Rev.* **2015**, 289-290, 74-122.
  23. (a) Mason, K.; Chang, J.; Garlatti, E.; Prescimone, A.; Yoshii, S.; Nojiri, H.; Schnack, J.; Tasker, P. A.; Carretta, S.; Brechin, E. K., Linking [Fe(III)<sub>3</sub>] triangles with "double-headed" phenolic oximes. *Chem. Commun. (Camb)* **2011**, 47 (21), 6018-6020; (b) Mason, K.; Chang, J.; Prescimone, A.; Garlatti, E.; Carretta, S.; Tasker, P. A.; Brechin, E. K., Linking [M(III)<sub>3</sub>] triangles with "double-headed" phenolic oximes. *Dalton Trans.* **2012**, 41(29), 8777-8785; (c) Wenzel, M.; Forgan, R. S.; Faure, A.; Mason, K.; Tasker, P. A.; Piligkos, S.; Brechin, E. K.; Plieger, P. G., A new polynuclear coordination type for (salicylaldoxime)copper(II) complexes: Structure and magnetic properties of an (oxime)Cu<sub>6</sub> cluster. *Eur. J. Inorg. Chem.* **2009**, (31), 4613-4617.
  24. Milios, C. J.; Vinslava, A.; Wernsdorfer, W.; Moggach, S.; Parsons, S.; Perlepes, S. P.; Christou, G.; Brechin, E. K., A record anisotropy barrier for a single-molecule magnet. *J. Am. Chem. Soc.* **2007**, 129, 2754-2755.
  25. Yang, C-I.; Cheng, K-H.; Hung, S-P.; Nakano, M.; Tsai, H-L., Crystal packing effects within [Mn<sup>III</sup><sub>3</sub>O]<sup>7+</sup> single-molecule magnets: Controlling intermolecular antiferromagnetic interactions. *Polyhedron* **2011**, 30(18), 3272-3278.
  26. Richers, C. P.; Bertke, J. A.; Gray, D. L.; Rauchfuss, T. B., Crystal structure of tetrakis-(acetylacetonato)-dichloridodi-μ<sub>3</sub>-methanolatotetra-μ<sub>2</sub>-methanolatotetrairon(III). *Acta Crystallogr. E Crystallogr. Commun.* **2015**, 71(Pt 8), 976-979.
  27. (a) Langley, S. K.; Chilton, N. F.; Massi, M.; Moubaraki, B.; Berry, K. J.; Murray, K. S., Synthesis and characterization of homo- and heterovalent tetra- hexa- hepta- and decanuclear manganese clusters using pyridyl functionalized beta-diketone,

- carboxylate and triethanolamine ligands. *Dalton Trans.* **2010**, 39(31), 7236-7249;
- (b) Peng, G.; Kostakis, G. E.; Lan, Y.; Powell, A. K., Body-wing swapping in butterfly {Fe(III)<sub>2</sub>Ln(III)<sub>2</sub>} coordination clusters with triethylene glycol as ligand. *Dalton Trans.* **2013**, 42(1), 46-49; (c) Peng, Y.; Mereacre, V.; Anson, C. E.; Powell, A. K., The role of coordinated solvent on Co(II) ions in tuning the single molecule magnet properties in a {CoDy} system. *Dalton Trans.* **2017**, 46(16), 5337-5343.
28. (a) Griffiths, K.; Tsipis, A. C.; Kumar, P.; Townrow, O. P. E.; Abdul-Sada, A.; Akien, G. R.; Baldansuren, A.; Spivey, A. C.; Kostakis, G. E., 3d/4f Coordination clusters as cooperative catalysts for highly diastereoselective michael addition reactions. *Inorg. Chem.* **2017**, 56(16), 9563-9573; (b) Jiang, L.; Zhang, D. Y.; Suo, J. J.; Gu, W.; Tian, J. L.; Liu, X.; Yan, S. P., Synthesis, magnetism and spectral studies of six defective dicubane tetranuclear {M<sub>4</sub>O<sub>6</sub>} (M = Ni(II), Co(II), Zn(II)) and three trinuclear Cd(II) complexes with polydentate Schiff base ligands. *Dalton Trans.* **2016**, 45(25), 10233-10248; (c) Liu, F.; Yang, F.; Chen, H.; Chen, Q.; Yan, P.; Li, G., Salen type homomultinuclear Yb<sub>3</sub> and Yb<sub>4</sub> complexes and their NIR luminescence. *J. Inorg. Organomet. Polym. Mater.* **2014**, 24(2), 259-266.
29. (a) Akhtar, M. N.; Mereacre, V.; Novitchi, G.; Tuchagues, J. P.; Anson, C. E.; Powell, A. K., Probing lanthanide anisotropy in Fe-Ln aggregates by using magnetic susceptibility measurements and <sup>57</sup>Fe Mössbauer spectroscopy. *Chem.* **2009**, 15(30), 7278-7282; (b) Glaser, T.; Lugger, T., A new tetranuclear iron complex with a [Fe<sub>4</sub>O<sub>6</sub>]<sub>6</sub> core: synthesis, structure, spectroscopic and magnetic properties. *Inorg. Chim. Acta* **2002**, (337), 103-112; (c) Rinck, J.; Lan, Y.; Anson, C. E.; Powell, A. K., Coordination cluster nuclearity decreases with decreasing rare earth ionic radius in 1:1 Cr/Ln *N*-butyldiethanolamine compounds: a journey across the lanthanide series from Cr<sub>4</sub>(III)Ln<sub>4</sub>-Cr<sub>4</sub>(III)Ln<sub>4</sub> via Cr<sub>3</sub>(III)Ln<sub>3</sub> and Cr<sub>3</sub>(III)Ln<sub>3</sub> to Cr<sub>2</sub>(III)Ln<sub>2</sub>. *Inorg. Chem.* **2015**, 54(7), 3107-3117.
30. (a) Das, D.; Mahata, G.; Adhikary, A.; Konar, S.; Biradha, K., Structural adaptation of Ni<sub>4</sub>O<sub>4</sub> units to form cubane, open dicubane, dimeric cubane, and one-dimensional polymeric cubanes: Magnetostructural correlation of Ni<sub>4</sub> clusters. *Cryst. Growth Des.* **2015**, 15(8), 4132-4141; (b) Mautner, F. A.; Scherzer, M.; Berger, C.; Fischer, R. C.; Vicente, R.; Massoud, S. S., Synthesis and characterization of three new 1-D polymeric [M<sub>2</sub>(4-azidopyridine)<sub>4</sub>(μ<sub>1,1</sub>-N<sub>3</sub>)<sub>2</sub>(μ<sub>1,3</sub>-N<sub>3</sub>)<sub>2</sub>]<sub>n</sub> (M=Ni, Co, Cd) complexes. *Polyhedron* **2015**, 85, 329-336; (c) Zeng, Y. F.; Hu, X.; Liu, F. C.; Bu, X. H., Azido-mediated systems showing different magnetic behaviors. *Chem. Soc. Rev.* **2009**, 38(2), 469-480.
31. (a) Bila, J. L.; Marmier, M.; Zhurov, K. O.; Scopelliti, R.; Živković, I.; Rønnow, H. M.; Shaik, N. E.; Sienkiewicz, A.; Fink, C.; Severin, K., Homo- and heterodinuclear iron clathrochelate complexes with functional groups in the ligand periphery. *Eur. J. Inorg. Chem.* **2018**, 2018(26), 3118-3125; (b) Cecot, G.; Marmier, M.; Geremia, S.; De Zorzi, R.; Vologzhanina, A. V.; Pattison, P.; Solari, E.; Fadaei Tirani, F.; Scopelliti, R.; Severin, K., The intricate structural chemistry of M(II)<sub>2n</sub>Ln-type assemblies. *J. Am.*

- Chem. Soc.* **2017**, *139*(24), 8371-8381; (c) Ge, C.; Zhang, J.; Qin, Z.; Zhang, P.; Zhang, R.; Zhao, H.; Wang, Y.; Zhang, X., Boron-capped binuclear Mn(II) clathrochelate complexes: Synthetic, structural, and electrochemical studies. *Inorg. Chim. Acta* **2017**, *463*, 134-141; (d) Marmier, M.; Cecot, G.; Curchod, B. F.; Pattison, P.; Solari, E.; Scopelliti, R.; Severin, K., Surface functionalization of dinuclear clathrochelates via Pd-catalyzed cross-coupling reactions: facile synthesis of polypyridyl metalloligands. *Dalton Trans.* **2016**, *45*(20), 8422-8427; (e) Marmier, M.; Cecot, G.; Vologzhanina, A. V.; Bila, J. L.; Zivkovic, I.; Ronnow, H. M.; Nafradi, B.; Solari, E.; Pattison, P.; Scopelliti, R.; Severin, K., Dinuclear clathrochelate complexes with pendent cyano groups as metalloligands. *Dalton Trans.* **2016**, *45*(39), 15507-15516; (f) Marmier, M.; Wise, M. D.; Holstein, J. J.; Pattison, P.; Schenk, K.; Solari, E.; Scopelliti, R.; Severin, K., Carboxylic acid functionalized clathrochelate complexes: Large, robust, and easy-to-access metalloligands. *Inorg. Chem.* **2016**, *55*(8), 4006-4015; (g) Pascu, M.; Marmier, M.; Schouwey, C.; Scopelliti, R.; Holstein, J. J.; Bricogne, G.; Severin, K., Anionic bipyridyl ligands for applications in metallasupramolecular chemistry. *Chemistry* **2014**, *20*(19), 5592-5600; (h) Qin, Z.; Han, F.; Ge, C.; Zhang, R.; Zhang, Y.; Zhang, X., Template synthesis of boron-capped cage metal complexes and assembly of supramolecular networks. *Inorg. Chim. Acta* **2018**, *479*, 36-41; (i) Zhang, J.; Ma, Z.; Zhao, H.; Ge, C.; Wang, Y.; Zhang, X., Bis-boron-capped tris(dioxime) cage complexes with terminal carbonyl groups. *Inorg. Chem. Commun.* **2016**, *65*, 63-67.
32. (a) Khanra, S.; Weyhernuller, T.; Bill, E.; Chaudhuri, P., Deliberate synthesis for magnetostructural study of linear tetranuclear complexes  $B^{III}Mn^{II}Mn^{II}B^{III}$ ,  $Mn^{III}Mn^{II}Mn^{II}Mn^{III}$ ,  $Mn^{IV}Mn^{II}Mn^{II}Mn^{IV}$ ,  $Fe^{III}Mn^{II}Mn^{II}Fe^{III}$ , and  $Cr^{III}Mn^{II}Mn^{II}Cr^{III}$ . Influence of terminal ions on the exchange coupling. *Inorg. Chem.* **2006**, *45*(15), 5911-5923; (b) Tandon, S. S.; Bunge, S. D.; Toth, S. A.; Sanchiz, J.; Thompson, L. K.; Shelley, J. T., Antiferromagnetically coupled dimeric dodecacopper supramolecular architectures of macrocyclic ligands with a symmetrical  $\mu_6\text{-BO}_3^{3-}$  central moiety. *Inorg. Chem.* **2015**, *54*(14), 6873-6884.
33. Martínez, L.; Bazzicalupi, C.; Bianchi, A.; Lloret, F.; González, R.; Kremer, C.; Chiozzzone, R., Structural and magnetic properties of polynuclear oximate copper complexes with different topologies. *Polyhedron* **2017**, *138*, 125-132.
34. (a) Parks, J. E.; Wagner, B. E.; Holm, R. H., Three-dimensional macrocyclic encapsulation reactions. II.<sup>1</sup> Synthesis and properties of nonoctahedral clathrochelates derived from tris(2-aldoximo-6-pyridyl)phosphine and boron trifluoride or tetrafluoroborate. *Inorg. Chem.* **1971**, *10*(11), 2472-2478; (b) Prushan, M. J.; Addison, A. W.; Butcher, R. J., Pentadentate thioether-oxime macrocyclic and quasi-macrocyclic complexes of copper(II) and nickel(II). *Inorg. Chim. Acta* **2000**, *300*, 992-1003.
35. (a) Pannu, A. P.; Stevens, J. R.; Plieger, P. G., Aryl-linked salicylaldoxime-based copper(II) helicates and "boxes": synthesis, X-ray analysis, and anion influence on



- complex structure. *Inorg. Chem.* **2013**, *52*(16), 9327-9337; (b) Wenzel, M.; Bruere, S. R.; Knapp, Q. W.; Tasker, P. A.; Plieger, P. G., Zwitterionic dicopper helicates: anion encapsulation and binding studies. *Dalton Trans.* **2010**, *39*(11), 2936-2941; (c) Wenzel, M.; Jameson, G. B.; Ferguson, L. A.; Knapp, Q. W.; Forgan, R. S.; White, F. J.; Parsons, S.; Tasker, P. A.; Plieger, P. G., Anion-induced contraction of helical receptors. *Chem. Commun.* **2009**, (24), 3606-3608; (d) Wenzel, M.; Knapp, Q. W.; Plieger, P. G., A bis-salicylaldoximato-copper(II) receptor for selective sulfate uptake. *Chem. Commun.* **2011**, *47*(1), 499-501; (e) De Silva, D. N. T.; Jameson, G. B.; Pannu, A. P. S.; Pouhet, R.; Wenzel, M.; Plieger, P. G., Piperazine linked salicylaldoxime and salicylaldimine-based dicopper(II) receptors for anions. *Dalton Trans.* **2015**, *44*(36), 15949-15959.
36. De Silva, D. N. T. Magneto-structural correlations of Iron-salicylaldoxime clusters. PhD thesis; Massey University, New Zealand; 2015; 294 pgs.
37. (a) Andruh, M., The exceptionally rich coordination chemistry generated by schiff-base ligands derived from *o*-vanillin. *Dalton Trans.* **2015**, *44*(38), 16633-16653; (b) Mukherjee, S.; Lu, J.; Velmurugan, G.; Singh, S.; Rajaraman, G.; Tang, J.; Ghosh, S. K., Influence of tuned linker functionality on modulation of magnetic properties and relaxation dynamics in a family of six isotypic Ln<sub>2</sub> (Ln = Dy and Gd) complexes. *Inorg. Chem.* **2016**, *55*(21), 11283-11298; (c) Zhang, K.; Wang, Y.-Y., A dinuclear dysprosium single-molecule magnet constructed by *o*-vanillin schiff base ligand: Magnetic properties and solution behaviour. *Inorg. Chem. Commun.* **2017**, *76*, 103-107; (d) Müller, J.; Kehr, G.; Fröhlich, R.; Erker, G., Structural features of titanium complexes of salicylaldiminato derivatives of amino acids. *Eur. J. Inorg. Chem.* **2005**, (14), 2836-2841; (e) Primik, M. F.; Goschl, S.; Meier, S. M.; Eberherr, N.; Jakupec, M. A.; Enyedy, E.; Novitchi, G.; Arion, V. B., Dicopper(II) and dizinc(II) complexes with nonsymmetric dinucleating ligands based on indolo[3,2-*c*]quinolines: synthesis, structure, cytotoxicity, and intracellular distribution. *Inorg. Chem.* **2013**, *52*(17), 10137-10146; (f) Zaltariov, M. F.; Hammerstad, M.; Arabshahi, H. J.; Jovanovic, K.; Richter, K. W.; Cazacu, M.; Shova, S.; Balan, M.; Andersen, N. H.; Radulovic, S.; Reynisson, J.; Andersson, K. K.; Arion, V. B., New iminodiacetate-thiosemicarbazone hybrids and their copper(II) complexes are potential ribonucleotide reductase R2 inhibitors with high antiproliferative activity. *Inorg. Chem.* **2017**, *56*(6), 3532-3549.
38. Aldred, R.; Johnston, R.; Levin, D.; Neilan, J., Magnesium-mediated ortho-specific formylation and formaldoximation of phenols. *J. Chem. Soc., Perkin Trans. 1* **1994**, (13), 1823-1831.
39. Meier, P.; Broghammer, F.; Latendorf, K.; Rauhut, G.; Peters, R., Cooperative Al(salen)-pyridinium catalysts for the asymmetric synthesis of *trans*-configured beta-lactones by [2+2]-cyclocondensation of acylbromides and aldehydes: investigation of pyridinium substituent effects. *Mol.* **2012**, *17*(6), 7121-7150.
40. Cruz-Huerta, J. Carillo-Morales, M.; Santacruz-Juarez, E.; Hernandez-Ahuactzi, I. F.; Escalante-Garcia, J.; Godoy-Alcantar, C.; Guerrero-Alvarez, J. A.; Hopfl, H.; Morales-

- Rojas, H.; Sanchez, M., Macrocyclic diorganotin complexes of  $\gamma$ -amino acid dithiocarbamates as hosts for ion-pair recognition. *Inorg. Chem.* **2008**, *47*, 9874-9885.
41. Stevens, J. R.; Plieger, P. G., Anion-driven conformation control and enhanced sulfate binding utilising aryl linked salicylaldoxime dicopper helicates. *Dalton Trans.* **2011**, *40*(45), 12235-12241.
42. (a) Akkus, N.; Campbell, J. C.; Davidson, J.; Henderson, D. K.; Miller, H. A.; Parkin, A.; Parsons, S.; Plieger, P. G.; Swart, R. M.; Tasker, P. A.; West, L. C., Exploiting supramolecular chemistry in metal recovery: novel zwitterionic extractants for nickel(II) salts. *Dalton Trans.* **2003**, 1932-1940; (b) Di Mauro, E. F.; Kozlowski, M. C., Salen-derived catalysts containing secondary basic groups in the addition of diethylzinc to aldehydes. *Org. Lett.* **2001**, *3*(19), 3053-3056; (c) Fennie, M. W.; Di Mauro, E. F.; O'Brien, E. M.; Annamalai, V.; Kozlowski, M. C., Mechanism and scope of salen bifunctional catalysts in asymmetric aldehyde and  $\alpha$ -ketoester alkylation. *Tetrahedron* **2005**, *61*(26), 6249-6265; (d) Jarrahpour, A.; Shirvani, P.; Sharghi, H.; Aberi, M.; Sinou, V.; Latour, C.; Brunel, J. M., Synthesis of novel mono- and bis-schiff bases of morpholine derivatives and the investigation of their antimalarial and antiproliferative activities. *Med. Chem. Res.* **2015**, *24*(12), 4105-4112; (e) Plieger, P. G. T., P. A.; Galbraith, S. G., Zwitterionic macrocyclic metal sulfate extractants containing 3-dialkylaminomethylsalicylalimine units. *Dalton Trans.* **2004**, 313-318.
43. (a) Galbraith, S. G.; Wang, Q.; Li, L.; Blake, A. J.; Wilson, C.; Collinson, S. R.; Lindoy, L. F.; Plieger, P. G.; Schroder, M.; Tasker, P. A., Anion selectivity in zwitterionic amide-functionalised metal salt extractants. *Chemistry* **2007**, *13*(21), 6091-6107; (b) Wen, Y. Q.; Ren, W. M.; Lu, X. B., Unsymmetric salen ligands bearing a Lewis base: intramolecularly cooperative catalysis for cyanosilylation of aldehydes. *Org. Biomol. Chem.* **2011**, *9*(18), 6323-6330.
44. Rao, H. S. P.; Rafi, S.; Kumar, P. R.; Guravaiah, C.; Muthanna, N., On the stereochemistry of the olefinic double bond in 13-membered heterocyclic rings accessible by ring-closing metathesis reaction. *Tetrahedron Lett.* **2012**, *53*(51), 6877-6880.
45. (a) Lee, D. H.; Lee, J. Y.; Jeong, J.; Kim, M.; Lee, K. W.; Jang, E.; Ahn, S.; Lee, C. H.; Hwang, J. Y., Synthesis and molecular modeling studies of *N'*-hydroxyindazolecarboximidamides as novel indoleamine 2,3-dioxygenase 1 (IDO1) inhibitors. *Mol.* **2017**, *22*(11); (b) Vijayendar, V.; Kaki, S. S.; Krishna, E. V.; Misra, S.; Prasad, R. B. N.; Jala, R. C. R., Synthesis and cytotoxic evaluation of undecenoic acid-based oxime esters. *Indian J. Chem.* **2018**, *57B*, 1015-1022.
46. Chen, H.; Ma, C-B.; Sun, L.; Chen, C-N., A family of  $\text{Fe}^{\text{III}}_4 \text{Ln}^{\text{III}}_4$  clusters containing derivatised salicylaldoximate ligand: Syntheses, structures and magnetic properties. *Polyhedron* **2017**, *132*, 90-94.

47. (a) Dolomanov, O. V.; Bourhis, L. J.; Gildea, R. J.; Howard, J. A. K.; Puschmann, H., OLEX2: A complete structure solution, refinement and analysis program. *J. Appl. Cryst.* **2009**, *42*, 339-341; (b) Spek, A., PLATON SQUEEZE: A tool for the calculation of the disordered solvent contribution to the calculated structure factors. *Acta Crystallogr., Sect. C.* **2015**, *71*(1), 9-18.
48. Steiner, T., The hydrogen bond in the solid state. *Angew. Chem. Int. Ed.* **2002**, *41*, 48-76.
49. (a) Bain, G. A.; Berry, J. F., Diamagnetic corrections and pascal's constants. *J. Chem. Ed.* **2008**, *85*(4), 532-536; (b) Marr, G.; Rockett, B. W., *Practical Inorganic Chemistry*. Reinhold: London; 1972; 444 pgs.
50. Joshi, S. R.; Habib, S. I., Synthesis, spectral study of Ni(II) and Cu(II) metal ions with heterocyclic ligands. *Int. J. Drug Dev. and Res.* **2014**, *6*(3), 32-38.
51. (a) Dolai, M.; Mondal, A.; Liu, J-L.; Ali, M., Three novel mononuclear Mn(III)-based magnetic materials with square pyramidal versus octahedral geometries. *New J. Chem.* **2017**, *41*(19), 10890-10898; (b) Grigoropoulos, A.; Pissas, M.; Papatolis, P.; Psycharis, V.; Kyritsis, P.; Sanakis, Y., Spin-relaxation properties of a high-spin mononuclear Mn(III)O<sub>6</sub>-containing complex. *Inorg. Chem.* **2013**, *52*(22), 12869-12871; (c) Realista, S.; Fitzpatrick, A. J.; Santos, G.; Ferreira, L. P.; Barroso, S.; Pereira, L. C.; Bandeira, N. A.; Neugebauer, P.; Hruby, J.; Morgan, G. G.; van Slageren, J.; Calhorda, M. J.; Martinho, P. N., A Mn(III) single ion magnet with tridentate schiff-base ligands. *Dalton Trans.* **2016**, *45*(31), 12301-12307.
52. Li, G-Z.; Zhang, S-H.; Liu, Z.; Jin, L-X., Aquabis(2,4-dichloro-6-formylphenolato-κ<sup>2</sup>O,O')(N,N'-dimethylformamide-κO)manganese(II). *Acta Cryst. Sect. E. Struct. Reports Online* **2007**, *63*(8), 2107.
53. Hindo, S. S.; Shakya, R.; Rannulu, N. S.; Allard, M. M.; Heeg, M. J.; Rodgers, M. T.; da Rocha, S. R. P.; Verani, C. N., Synthesis, redox, and amphiphilic properties of responsive salicylaldehyde-copper(II) soft materials. *Inorg. Chem.* **2008**, *47*, 3119-3127.
54. (a) Crawford, V. H.; Richardson, H. W.; Wasson, J.R.; Hodgson, D. J.; Hatfield, W.E., Relationship between the singlet-triplet splitting and the Cu-O-Cu bridge angle in hydroxo-bridged copper dimers. *Inorg. Chem.* **1976**, *15*(9), 2107-2110; (b) Merz, L.; Haase, W., Exchange interaction in tetrameric oxygen-bridged copper(II) clusters of the cubane type. *J. Chem. Soc., Dalton Trans.* **1980**, (6), 875-879.
55. Schrauzer, G. N., Chemistry of metal coordination compounds. I. Reaction of bis(dimethylglyoxime)-nickel with boron compounds. *Chem. Ber.* **1962**, *95*, 1438-1445.
56. Madhu, N. T.; Tang, J-K.; Hewitt, I. J.; Clérac, R.; Wernsdorfer, W.; Slageren, J. V.; Anson, C. E.; Powell, A. K., What makes a single molecule magnet? *Polyhedron* **2005**, *24*, 2864-2869.
57. (a) Chandra, S.; Sangeetika; Sharma, S. D., Mössbauer and electronic spectral studies of iron(III) complexes of oximes. *Spectrochim. Acta Part A: Mol. Biomol. Spectrosc.*

- 2003**, 59(4), 755-760; (b) Raptopoulou, C. P.; Sanakis, Y.; Boudalis, A. K.; Psycharis, V., Salicylaldoxime (H<sub>2</sub>salox) in iron(III) carboxylate chemistry: Synthesis, X-ray crystal structure, spectroscopic characterization and magnetic behavior of trinuclear oxo-centered complexes. *Polyhedron* **2005**, 24(5), 711-721; (c) Abbas, G.; Lan, Y.; Mereacre, V.; Wernsdorfer, W.; Clerac, R.; Buth, G.; Sougrati, M. T.; Grandjean, F.; Long, G. J.; Anson, C. E.; Powell, A. K., Magnetic and <sup>57</sup>Fe Mössbauer study of the single-molecule magnet behavior of a Dy<sub>3</sub>Fe<sub>7</sub> coordination cluster. *Inorg. Chem.* **2009**, 48(19), 9345-9355.
58. (a) Gass, I. A.; Milios, C. J.; Collins, A.; White, F. J.; Budd, L.; Parsons, S.; Murrie, M.; Perlepes, S. P.; Brechin, E. K., Polymetallic clusters of iron(III) with derivatised salicylaldoximes. *Dalton Trans.* **2008**, (15), 2043-2053; (b) Inglis, R.; Taylor, S. M.; Jones, L. F.; Papaefstathiou, G. S.; Perlepes, S. P.; Datta, S.; Hill, S.; Wernsdorfer, W.; Brechin, E. K., Twisting, bending, stretching: Strategies for making ferromagnetic [Mn(III)<sub>3</sub>] triangles. *Dalton Trans.* **2009**, (42), 9157-9168.
59. (a) Stamatatos, T. C.; Foguet-Albiol, D.; Stoumpos, C. C.; Raptopoulou, C. P.; Terzis, A.; Wernsdorfer, W.; Perlepes, S. P.; Christou, G., Initial example of a triangular single-molecule magnet from ligand-induced structural distortion of a [Mn(III)<sub>3</sub>O]<sup>7+</sup> complex. *J. Am. Chem. Soc.* **2005**, 127(44), 15380-15381; (b) Stamatatos, T. C.; Foguet-Albiol, D.; Lee, S.-C.; Stoumpos, C. C.; Raptopoulou, C. P.; Terzis, A.; Wernsdorfer, W.; Hill, S. O.; Perlepes, S. P.; Christou, G., "Switching on" the properties of single-molecule magnetism in triangular manganese(III) complexes. *J. Am. Chem. Soc.* **2007**, 129, 9484-9499.
60. (a) Stelzig, L.; Steiner, A.; Chansou, B.; Tuchagues, J.-P., Versatile pentadentate 1,5-bis(salicylideneamino)pentan-3-ol type ligands yield novel tri- and tetramanganese(II) complexes: Structure and properties. *Chem. Commun.* **1998**, (7), 771-772; (b) Milios, C. J.; Raptopoulou, C. P.; Terzis, A.; Lloret, F.; Vicente, R.; Perlepes, S. P.; Escuer, A., Hexanuclear manganese(III) single-molecule magnets. *Angew. Chem. Int. Ed. Engl.* **2004**, 43(2), 210-212; (c) Sreerama, S. G.; Pal, S., A novel carboxylate-free ferromagnetic trinuclear μ<sub>3</sub>-oxo-manganese(III) complex with distorted pentagonal-bipyramidal metal centers. *Inorg. Chem.* **2002**, 41, 4843-4845.
61. (a) Kozoni, C.; Manolopoulou, E.; Siczek, M.; Lis, T.; Brechin, E. K.; Milios, C. J., Polynuclear manganese amino acid complexes. *Dalton Trans.* **2010**, 39(34), 7943-7950; (b) Stoumpos, C. C.; Inglis, R.; Karotsis, G.; Jones, L. F.; Collins, A.; Parsons, S.; Milios, C. J.; Papaefstathiou, G. S.; Brechin, E. K., Supramolecular entanglement from interlocked molecular nanomagnets. *Cryst. Growth Des.* **2009**, 9(1), 24-27; (c) Yang, C.-I.; Feng, P.-Y.; Chen, Y.-T.; Tsai, Y.-J.; Lee, G.-H.; Tsai, H.-L., Molecular architecture based on manganese triangles: Monomer, dimer, and one-dimensional polymer. *Polyhedron* **2011**, 30(18), 3265-3271.
62. Chilton, N. F.; Anderson, R. P.; Turner, L. D.; Soncini, A.; Murray, K. S., PHI: A powerful new program for the analysis of anisotropic monomeric and exchange-coupled polynuclear *d*- and *f*-block complexes. *J. Comput. Chem.* **2013**, 34(13), 1164-1175.

63. (a) Das, A.; Klinke, F. J.; Demeshko, S.; Meyer, S.; Dechert, S.; Meyer, F., Reversible solvatomagnetic effect in novel tetranuclear cubane-type Ni<sub>4</sub> complexes and magnetostructural correlations for the [Ni<sub>4</sub>(μ<sub>3</sub>-O)<sub>4</sub>] core. *Inorg. Chem.* **2012**, *51*(15), 8141-8149; (b) Palacios, M. A.; Mota, A. J.; Perea-Buceta, J. E.; White, F. J.; Brechin, E. K.; Colacio, E., Antiferromagnetic versus ferromagnetic exchange interactions in bis(μ-o(oximate))dinickel(II) units for a series of closely related cube shaped carboxamideoximate-bridged Ni<sub>4</sub> complexes. A combined experimental and theoretical magneto-structural study. *Inorg. Chem.* **2010**, *49*(21), 10156-10165; (c) Perlepe, P. S.; Athanasopoulou, A. A.; Alexopoulou, K. I.; Raptopoulou, C. P.; Psycharis, V.; Escuer, A.; Perlepes, S. P.; Stamatatos, T. C., Structural and magnetic variations in tetranuclear Ni(II) clusters: the effect of the reaction solvent and ligand substitution on product identity. *Dalton Trans.* **2014**, *43*(44), 16605-16609; (d) Perlepe, P. S.; Cunha-Silva, L.; Bekiari, V.; Gagnon, K. J.; Teat, S. J.; Escuer, A.; Stamatatos, T. C., Structural diversity in Ni(II) cluster chemistry: Ni<sub>5</sub>, Ni<sub>6</sub>, and {NiNa<sub>2</sub>}<sub>n</sub> complexes bearing the schiff-base ligand *N*-naphthalidene-2-amino-5-chlorobenzoic acid. *Dalton Trans.* **2016**, *45*(25), 10256-10270; (e) Slater-Parry, M. E.; Durrant, J. P.; Howells, J. M.; Pitak, M. B.; Horton, P. N.; Klooster, W. T.; Coles, S. J.; O'Connor, H. M.; Brechin, E. K.; Barra, A. L.; Jones, L. F., Crowding out: Ligand modifications and their structure directing effects on brucite-like {M<sub>x</sub>(μ<sub>3</sub>-OH)<sub>y</sub>} (M = Co(II), Ni(II)) core growth within polymetallic cages. *Dalton Trans.* **2019**, *48*(4), 1477-1488; (f) Zhao, L.; Wu, J.; Ke, H.; Tang, J., Family of defect-dicubane Ni<sub>4</sub>Ln<sub>2</sub> (Ln = Gd, Tb, Dy, Ho) and Ni<sub>4</sub>Y<sub>2</sub> complexes: Rare Tb(III) and Ho(III) examples showing SMM behavior. *Inorg. Chem.* **2014**, *53*(7), 3519-3525.
64. Rigaku, O. D. *CrysAlis PRO*, Rigaku Oxford Diffraction Ltd.: Yarnton, England, 2017.
65. (a) Sheldrick, G. M., Crystal structure refinement with SHELXL. *Acta Crystallogr. C. Struct. Chem.* **2015**, *71*(Pt 1), 3-8; (b) Sheldrick, G. M., SHELXT - Integrated space-group and crystal-structure determination. *Acta Crystallogr. A* **2015**, *71*, 3-8.
66. (a) *PROCESS-AUTO*, Rigaku Corporation: Tokyo, 1998; (b) *Crystal Clear*, v. 1.4.0; Rigaku Americas Corporation: The Woodlands, Texas, 2005; (c) Chapuis, L. P. G., Superflip - a computer program for the solution of crystal structures by charge flipping in arbitrary dimensions. *J. Appl. Cryst.* **40**, 786-790; (d) Palatinus, L.; Van der Lee, A., Symmetry determination following structure solution in P1. *J. Appl. Cryst.* **2008**, *41*(6), 975-984; (e) Palatinus, L.; Chapuis, G., *J. Appl. Cryst.* **2007**, *40*, 786-790; (f) Palatinus, L.; Prathapa, S. J.; Van Smaalen, S., *J. Appl. Cryst.* **2012**, *45*, 575-580.

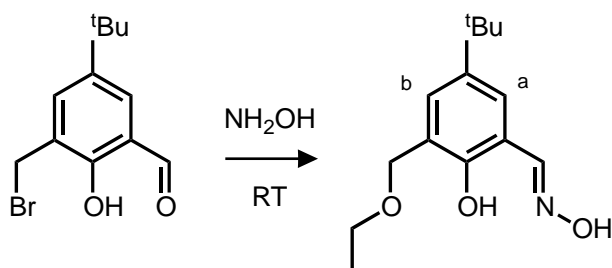
# Appendices

<b>A1.0 Synthesis and Characterisation of 5-tert-Butyl-3-(ethoxymethyl)-2-hydroxybenzaldehyde oxime .....</b>	<b>115</b>
A1.1 Synthesis of 5-tert-Butyl-3-(ethoxymethyl)-2-hydroxybenzaldehyde oxime .....	115
<b>A2.0 Characterisation of New Aldehyde Precursors (L2a &amp; L3a).....</b>	<b>117</b>
A2.1 <sup>1</sup> H NMR of L2a .....	117
A2.2 <sup>13</sup> C NMR of L2a .....	118
A2.3 <sup>1</sup> H NMR of L3a .....	119
A2.4 <sup>13</sup> C NMR of L3a .....	120
<b>A3.0 Characterisation of New Ligands (L2 &amp; L3).....</b>	<b>121</b>
A3.1 <sup>1</sup> H NMR of L2 .....	121
A3.2 <sup>13</sup> C NMR of L2 .....	122
A3.3 <sup>1</sup> H NMR of L3 .....	123
A3.4 <sup>13</sup> C NMR of L3 .....	124

## A1.0 Synthesis and Characterisation of 5-*tert*-Butyl-3-(ethoxymethyl)-2-hydroxybenzaldehyde oxime

### A1.1 Synthesis of 5-*tert*-Butyl-3-(ethoxymethyl)-2-hydroxybenzaldehyde oxime

Before the coupling procedure of Stevens and Plieger was chosen to synthesis **L1a-L4a**, several other methods were attempted. One attempt involved the oximation of the compound **2** following the method utilised for **L1-L4**. Instead of the formation of 5-*tert*-Butyl-3-bromomethyl-2-hydroxybenzaldehyde oxime, it was found that the compound 5-*tert*-Butyl-3-(ethoxymethyl)-2-hydroxybenzaldehyde oxime was produced instead.



The compound 5-*tert*-Butyl-3-(ethoxymethyl)-2-hydroxybenzaldehyde oxime was prepared from an adapted version of De Silva *et al.*<sup>35e</sup> The compound **2** (1.03 g, 3.80 mmol, 1.0 eq.) was dissolved in EtOH (50 mL) and refluxed for one hour, then cooled to RT. A solution of  $\text{NH}_2\text{OH}\cdot\text{HCl}$  (0.513 g, 7.38 mmol, 2.0 eq.) in EtOH (30 mL) was neutralised with a solution of KOH (0.414 g, 7.38 mmol, 2.0 eq.) in EtOH (30 mL). The filtered solution was added slowly dropwise into the cooled reaction mixture. The resulting solution was stirred for 24 hours at RT. The light-yellow solution was concentrated *in vacuo* affording an oil, which was redissolved in  $\text{CHCl}_3$  (30 mL). This solution was washed with deionised  $\text{H}_2\text{O}$  (3 x 30 mL) and the combined organic layers dried over anhydrous  $\text{MgSO}_4$ , filtered and concentrated *in vacuo* affording 5-*tert*-Butyl-3-(ethoxymethyl)-2-hydroxybenzaldehyde oxime as a yellow solid (0.844 g, 3.36 mmol, 89%) The crude material was recrystallised from hot pentane, to give colourless platelet shaped crystals.  $^1\text{H}$  NMR (500 MHz,  $\text{CDCl}_3$ ):  $\delta$  8.23 (1H, s,  $\text{CH}=\text{N}$ ), 7.41 (1H, d,  $J = 2.2$  Hz, *b*), 7.11 (1H, d,  $J = 2.2$  Hz, *a*), 4.61 (2H, s,  $\text{Ar-CH}_2\text{-N}$ ), 3.62 (2H, q,  $J = 7.2$  Hz,  $\text{CH}_3\text{-CH}_2\text{-O}$ ), 1.30 (9H, s, *t*Bu) 1.28 (3H, t,  $J = 7.2$  Hz,  $\text{CH}_3\text{-CH}_2\text{-O}$ ); IR:  $\bar{\nu} = 3400$  (O-H), 2961 (C-H), 1625 (C=N), 1480 (C-H), 1392 (*t*Bu),

1362 (O-H), 1219 (C-O), 1085 (C-N)  $\text{cm}^{-1}$ ; MS:  $m/z$  (ESI) 252  $[\text{M}+\text{H}]^+$ . **Crystal Data** for  $\text{C}_{14}\text{H}_{21}\text{NO}_3$  ( $M=251.32$  g/mol): monoclinic, space group  $P2_1/c$  (no. 14),  $a = 10.6302(19)$  Å,  $b = 8.2397(18)$  Å,  $c = 16.265(3)$  Å,  $\beta = 103.023(8)^\circ$ ,  $V = 1388.0(5)$  Å<sup>3</sup>,  $Z = 4$ ,  $T = 123$  K,  $\mu(\text{CuK}\alpha) = 0.679$   $\text{mm}^{-1}$ ,  $D_{\text{calc}} = 1.203$   $\text{g}/\text{cm}^3$ , 9592 reflections measured ( $11.168^\circ \leq 2\theta \leq 130.166^\circ$ ), 2335 unique ( $R_{\text{int}} = 0.1121$ ,  $R_{\text{sigma}} = 0.1984$ ) which were used in all calculations. The final  $R_1$  was 0.0836 ( $I > 2\sigma(I)$ ) and  $wR_2$  was 0.2515 (all data).

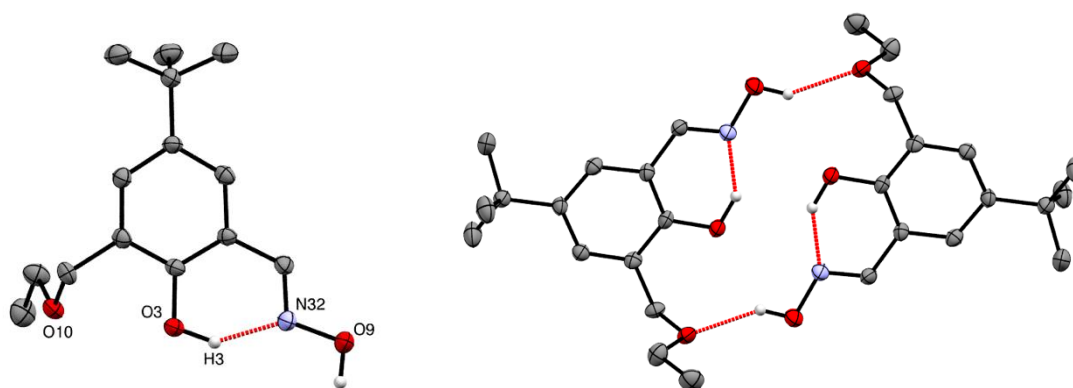


**Figure 41:** Crystal Structure of 5-*tert*-Butyl-3-(ethoxymethyl)-2-hydroxybenzaldehyde oxime (left). Hydrogen bonded dimers found within the cell (right). H atoms, apart from attached to heteroatoms, have been omitted for clarity; N = blue, O = red, C = grey, H = white. Hydrogen bonding represented as red dotted lines. ORTEP view at 30% probability level.

As mentioned earlier, the structure of 5-*tert*-Butyl-3-(ethoxymethyl)-2-hydroxybenzaldehyde oxime was obtained when the hot recrystallisation from pentane resulted in colourless, platelet-shaped crystals. This ligand structure is monoclinic and crystallises in the  $P2_1/c$  space group, with the entire ligand found within the asymmetric unit. Hydrogen bonding is present within the structure between the phenolic oxygen atom and oximic nitrogen atom ( $\text{O3}\cdots\text{N32}$ ,  $1.73(5)$  Å). Two structures are found within close contact of each other, hydrogen bonding to one and another in a *trans* conformation. Additional hydrogen bonds are found between the oximic OH and ether oxygen ( $\text{O9}\cdots\text{O10}$ ,  $2.85(4)$  Å).



## A2.0 Characterisation of New Aldehyde Precursors (L2a & L3a)

### A2.1 $^1\text{H}$ NMR of L2a

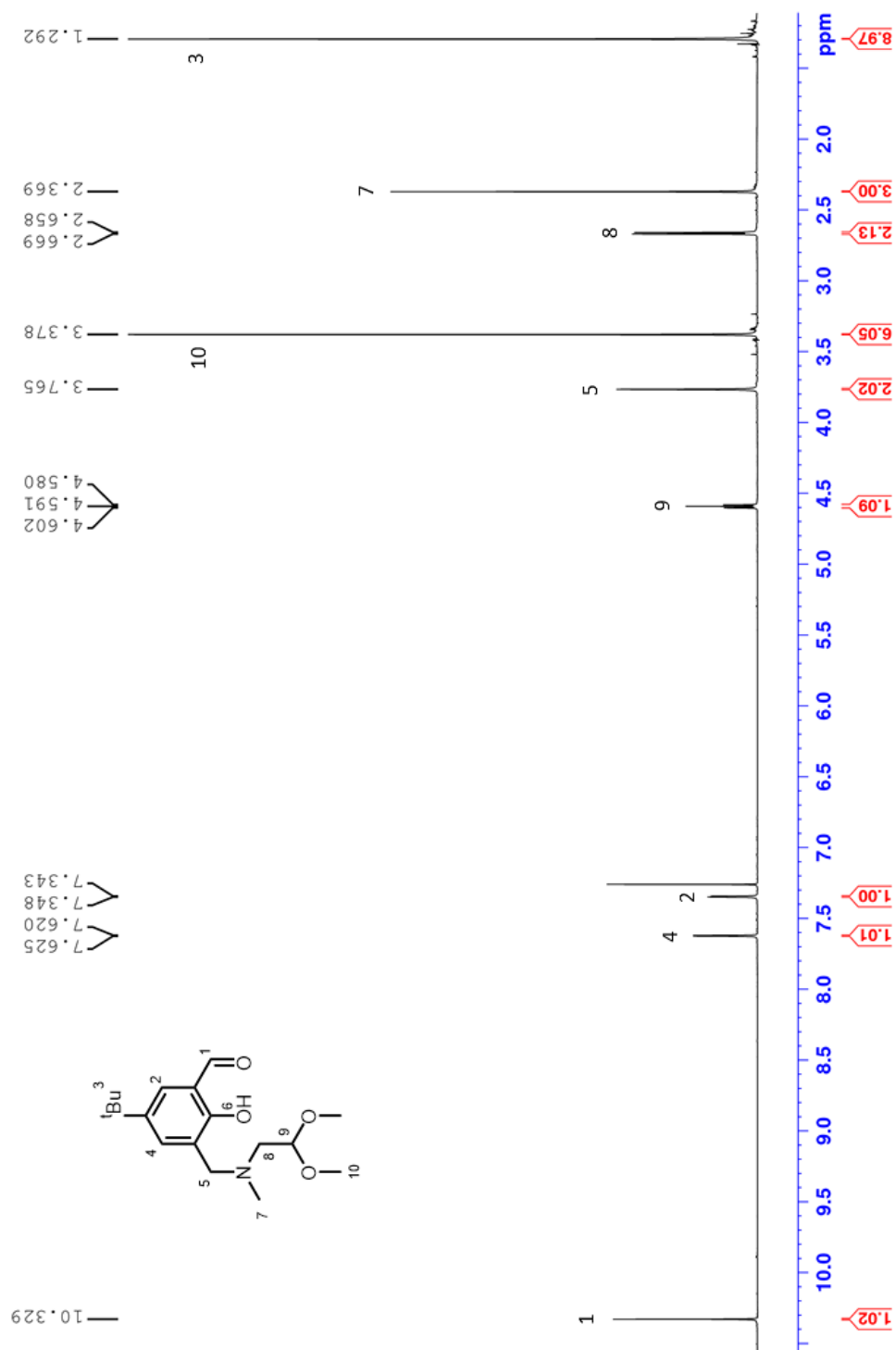


**Figure 42:**  $^1\text{H}$  NMR of L2a. Reference solvent peak ( $\text{CDCl}_3$ ) at 7.26 ppm.

## A2.2 $^{13}\text{C}$ NMR of L2a

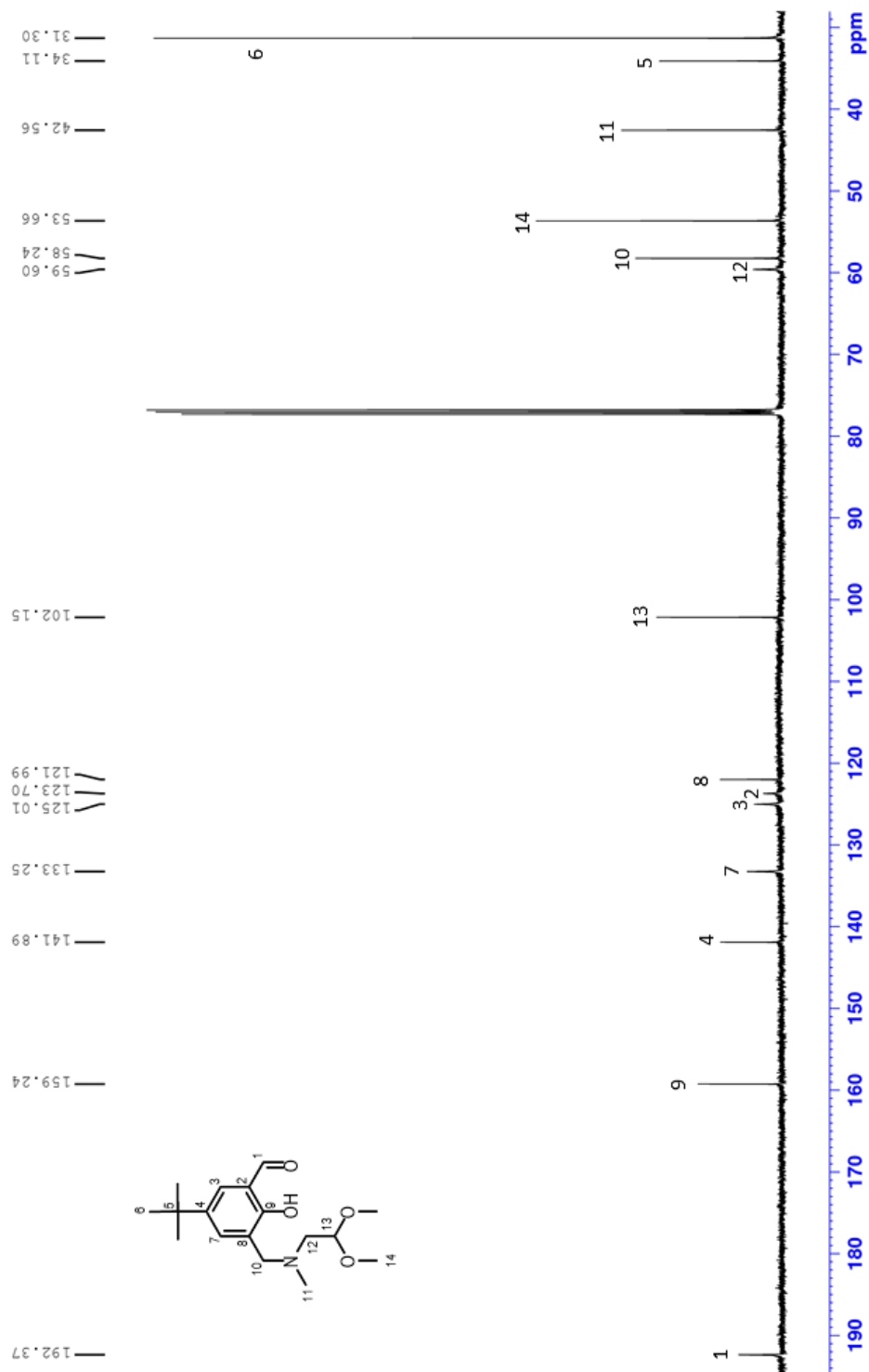


**Figure 43:**  $^{13}\text{C}$  NMR of L2a. Reference solvent peak (CDCl<sub>3</sub>) at 77 ppm.

A2.3  $^1\text{H}$  NMR of L3a

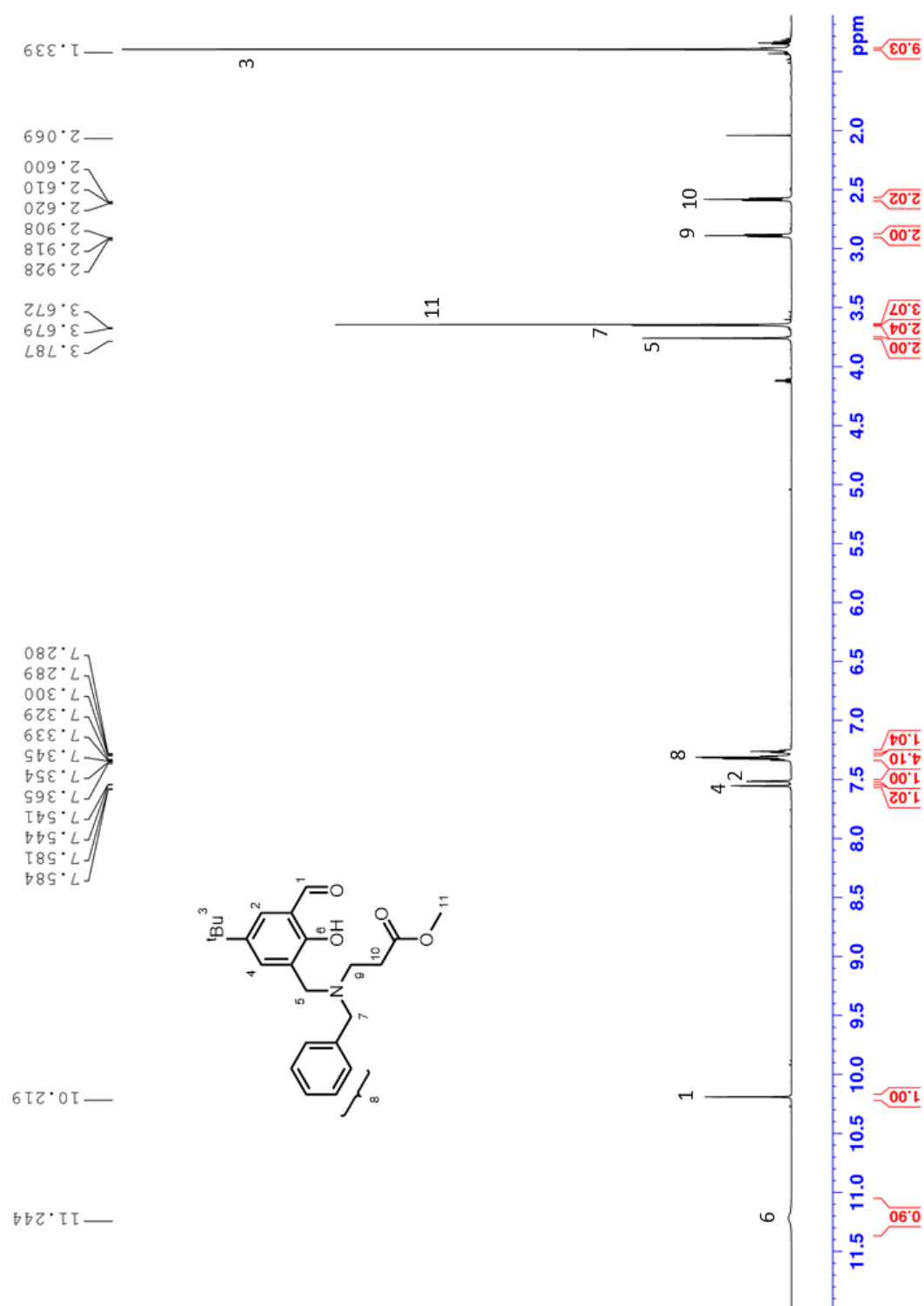


Figure 44:  $^1\text{H}$  NMR of L3a. Reference solvent peak ( $\text{CDCl}_3$ ) at 7.26 ppm.

A2.4  $^{13}\text{C}$  NMR of L3a

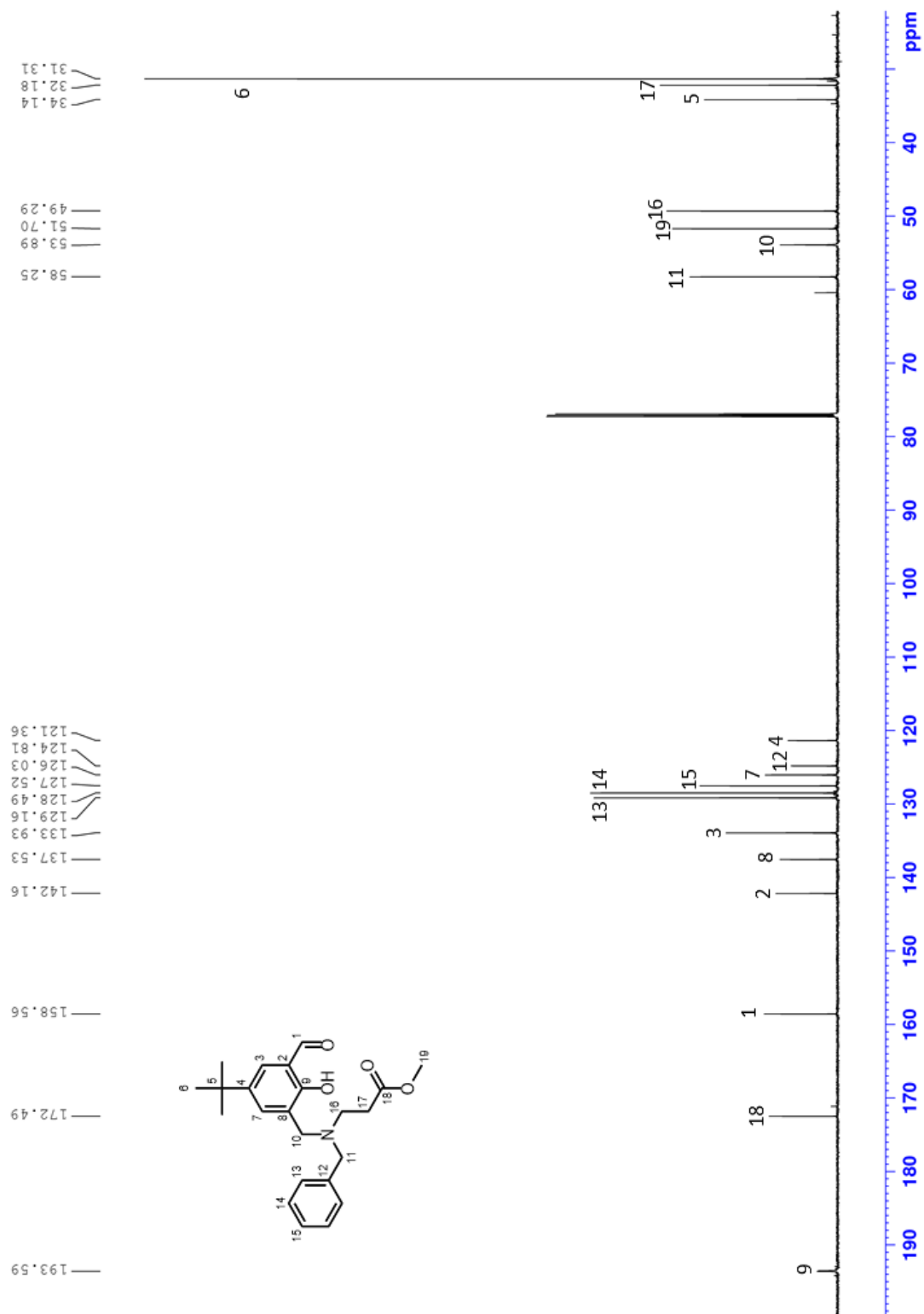
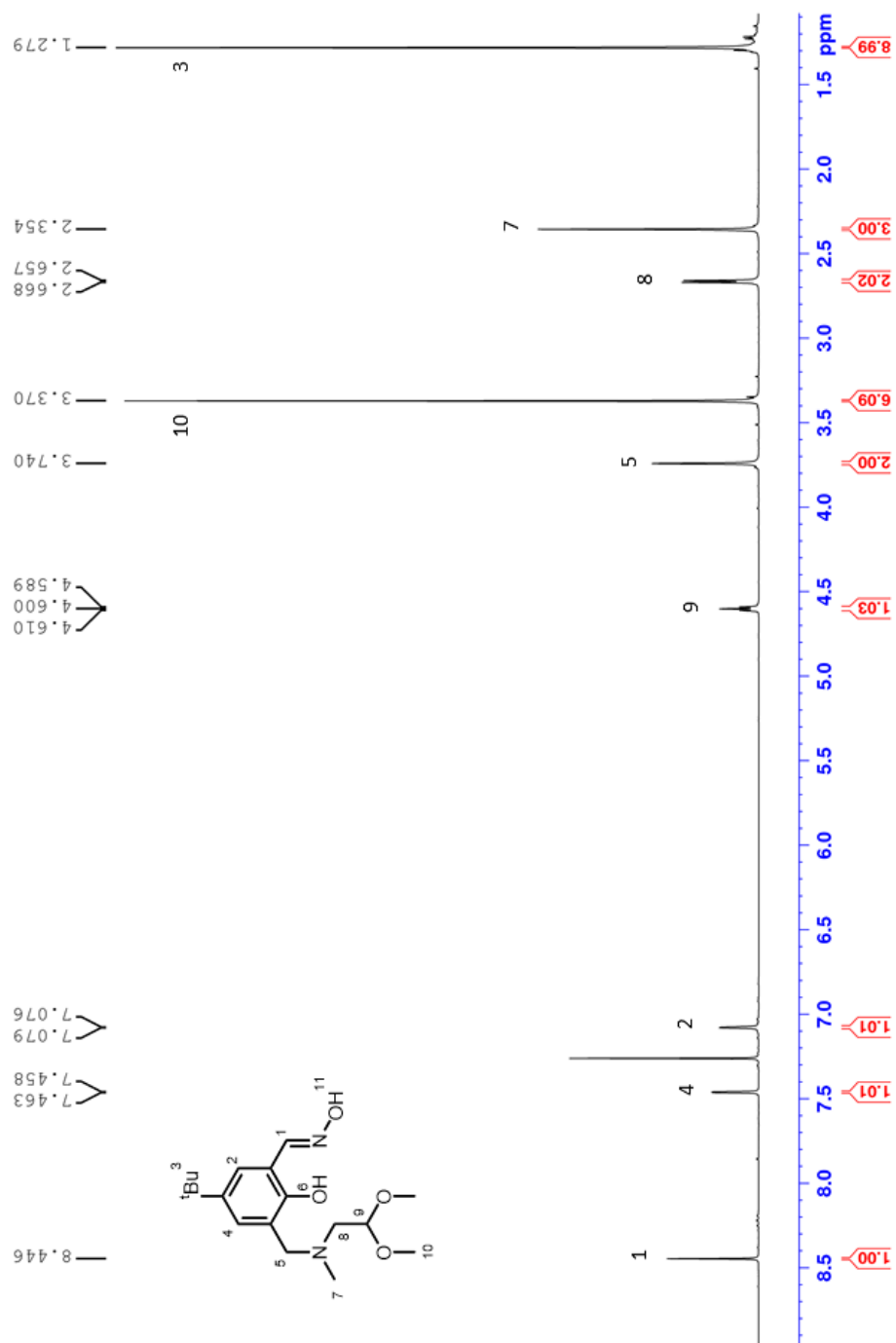


Figure 45:  $^{13}\text{C}$  NMR of L3a. Reference solvent peak ( $\text{CDCl}_3$ ) at 77 ppm.

## A3.0 Characterisation of New Ligands (L2 & L3)

### A3.1 $^1\text{H}$ NMR of L2



**Figure 46:**  $^1\text{H}$  NMR of L2. Reference solvent peak ( $\text{CDCl}_3$ ) at 7.26 ppm.

### A3.2 $^{13}\text{C}$ NMR of L2

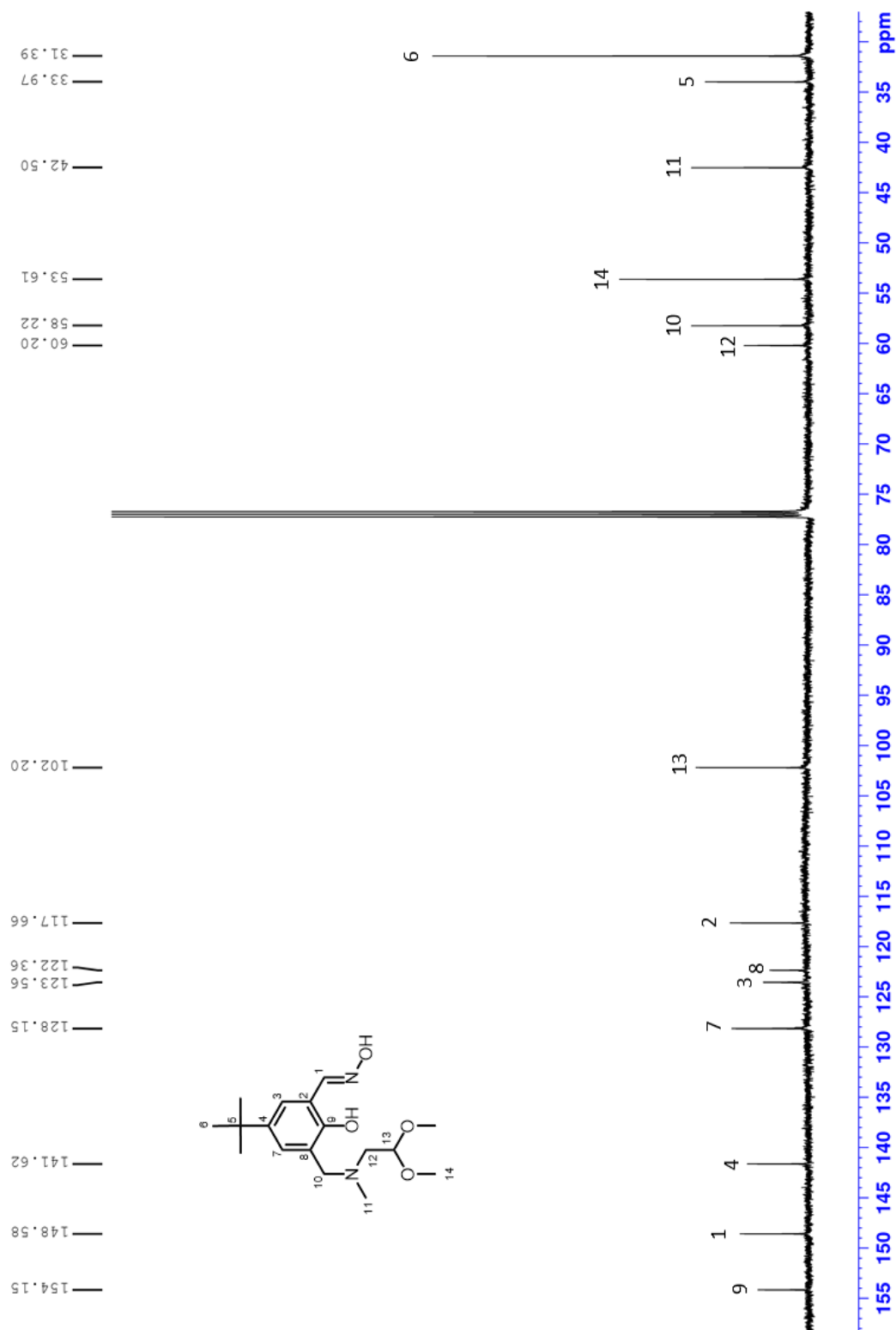


**Figure 47:**  $^{13}\text{C}$  NMR of L2. Reference solvent peak ( $\text{CDCl}_3$ ) at 77 ppm.

### A3.3 $^1\text{H}$ NMR of L3

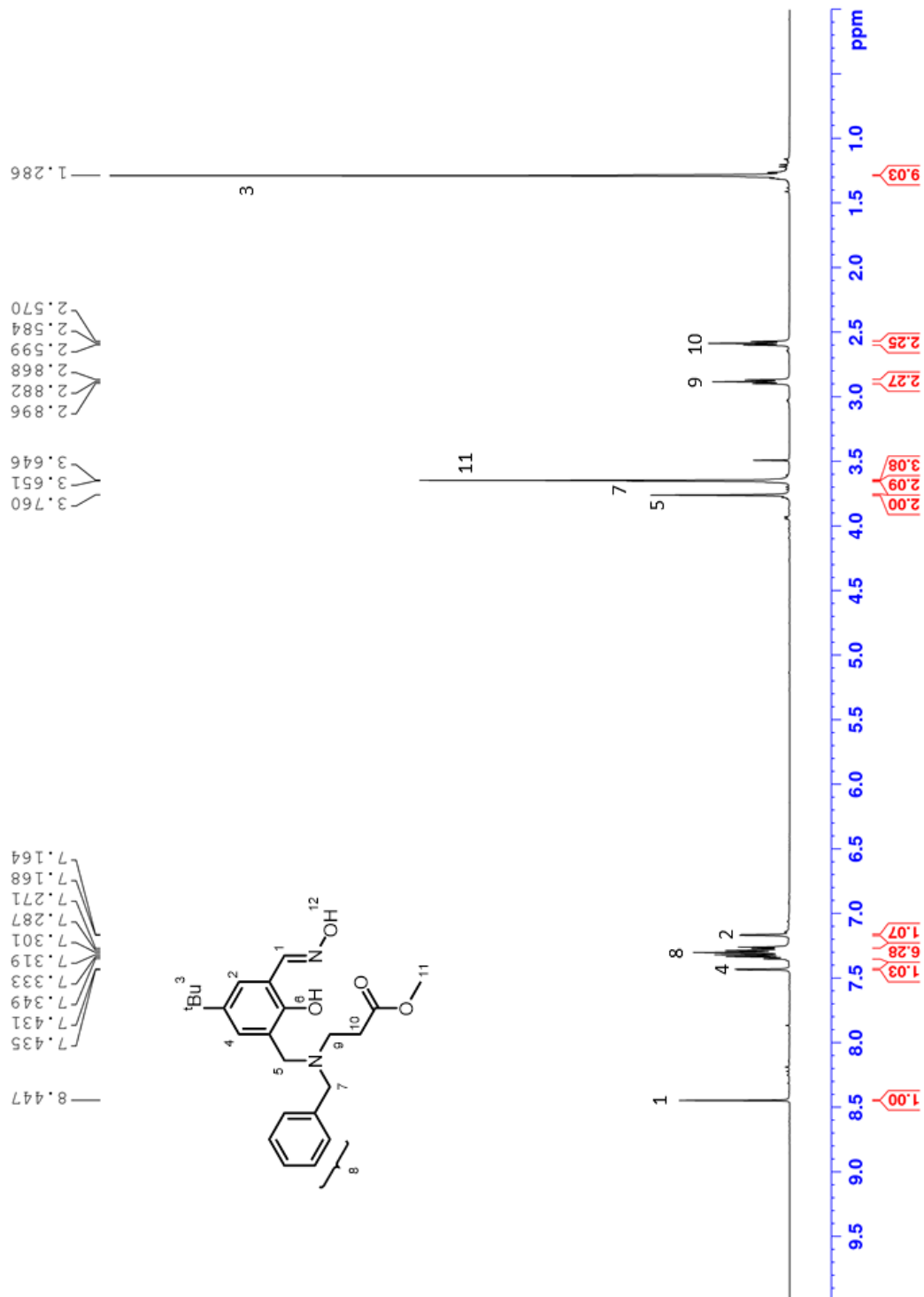
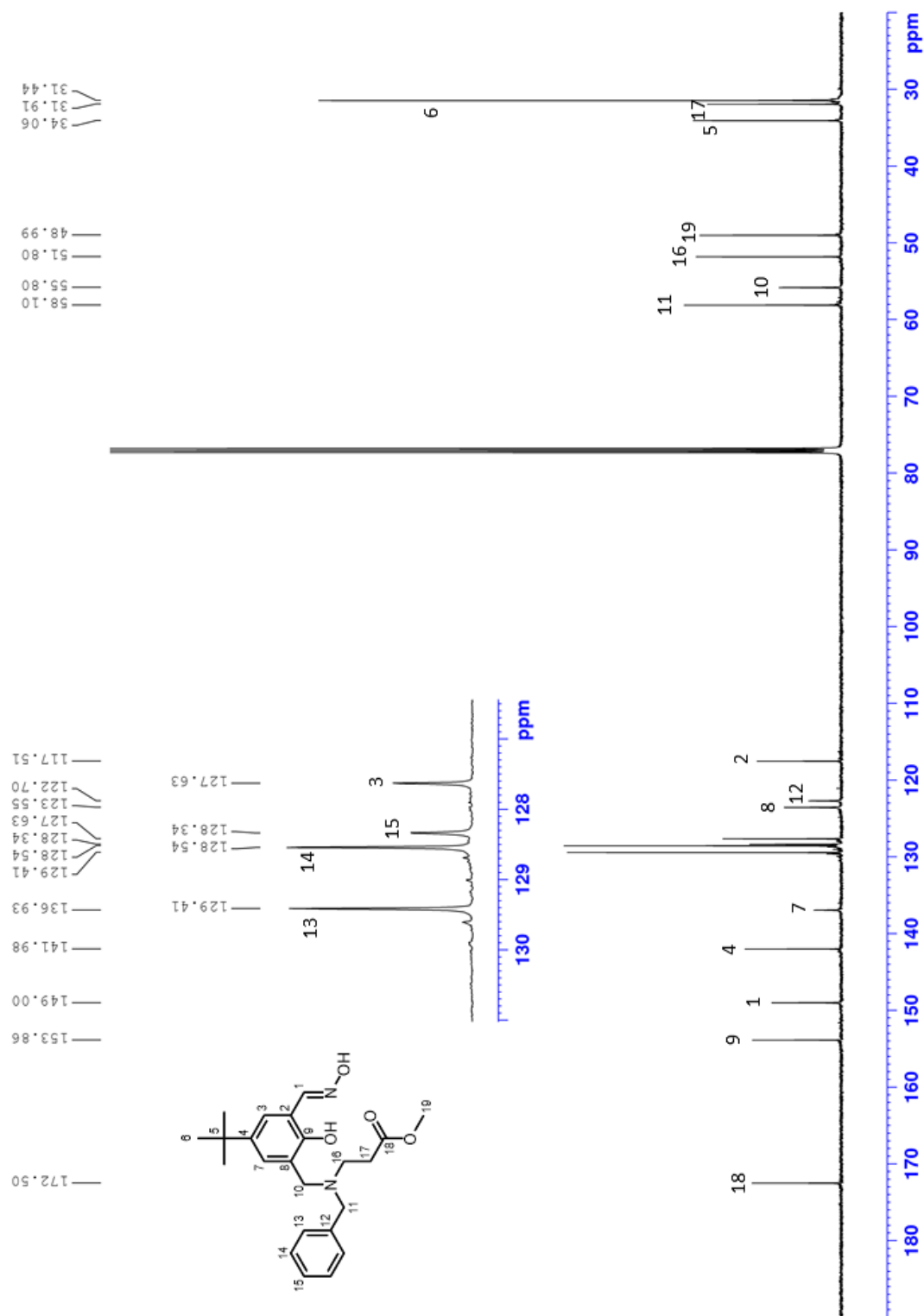


Figure 48:  $^1\text{H}$  NMR of L3. Reference solvent peak ( $\text{CDCl}_3$ ) at 7.26 ppm.

### A3.4 $^{13}\text{C}$ NMR of L3



**Figure 49:**  $^{13}\text{C}$  NMR of L3. Reference solvent peak ( $\text{CDCl}_3$ ) at 77 ppm.